2000

Plasma source ion implantation of high voltage electrodes

Thomas Joseph Venhaus
College of William & Mary - Arts & Sciences

INFORMATION TO USERS

This manuscript has been reproduced from the microfilm master. UMI films the text directly from the original or copy submitted. Thus, some thesis and dissertation copies are in typewriter face, while others may be from any type of computer printer.

The quality of this reproduction is dependent upon the quality of the copy submitted. Broken or indistinct print, colored or poor quality illustrations and photographs, print bleedthrough, substandard margins, and improper alignment can adversely affect reproduction.

In the unlikely event that the author did not send UMI a complete manuscript and there are missing pages, these will be noted. Also, if unauthorized copyright material had to be removed, a note will indicate the deletion.

Oversize materials (e.g., maps, drawings, charts) are reproduced by sectioning the original, beginning at the upper left-hand corner and continuing from left to right in equal sections with small overlaps.

Photographs included in the original manuscript have been reproduced xerographically in this copy. Higher quality 6" x 9" black and white photographic prints are available for any photographs or illustrations appearing in this copy for an additional charge. Contact UMI directly to order.

Bell & Howell Information and Learning
300 North Zeeb Road, Ann Arbor, MI 48106-1346 USA
800-521-0600

UMI®

PLASMA SOURCE ION IMPLANTATION OF HIGH VOLTAGE ELECTRODES

A Dissertation

Presented to The Faculty of the Department of Applied Science

The College of William and Mary

In Partial Fulfillment

Of the Requirements for the Degree of

Doctor of Philosophy

By

Thomas J. Venhaus

December 1999

APPROVAL SHEET

This dissertation is submitted in partial fulfillment
of the requirements for the degree of

Doctor of Philosophy.

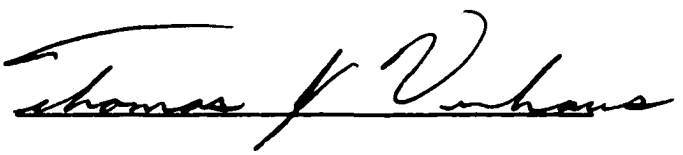

Thomas J. Venhaus

Approved, December 1999

Dennis M. Manos

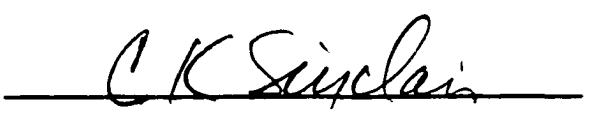

Charles K. Sinclair

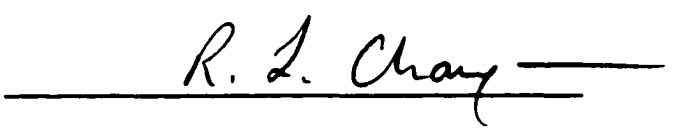

Roy L. Champion

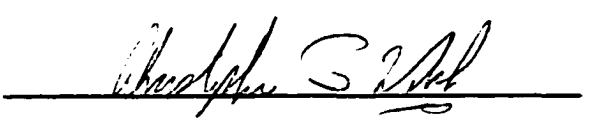

Christopher S. Welch

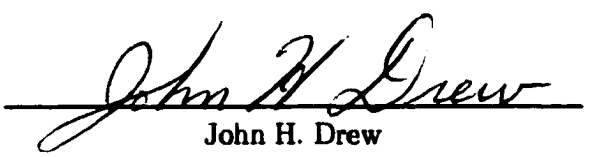

John H. Drew
Department of Mathematics

Dedicated to

Mom,

for putting me in college,

Dawn,

for keeping me there,

and Greyson,

for getting me out.

Contents

List of Tables

List of Figures

Abstract

Field emission and breakdown characteristics of high voltage, large area electrodes determine the performance of many vacuum-based electron sources. A corraborative plan with the Thomas Jefferson National Accelerator Facility involves studying the behavior of such electrodes after nitrogen ion implantation. A Plasma Source Ion Implantation (PSII) facility is designed and contructed at William and Mary, and used to treat stainless steel electrodes. PSII is a novel implantation technique developed at the University of Wisconsin - Madison. A workpiece is submerged in a quiescent plasma of the species to be implanted. A series of high, negative voltages (30 - 100 kV) is applied to the workpiece to accelerate the ions in the plasma, implanting them to depths of several hundred Angstroms. To characterize the response of the modified electrodes to high field gradients, fields as high as 20 MV/m are applied between parallel electrodes in a VG ESCALab MKII surface analysis system. XPS, AES, and SEM are used to characterize the surface of the cathodes. The pre-breakdown current from implanted electrodes is compared to that of thin film coated, polished, electron beam treated, and untreated electrodes. Current models to explain anomalous field emission are reviewed and considered as explanation of observed effects.

PLASMA SOURCE ION IMPLANTATION OF HIGH VOLTAGE ELECTRODES

Chapter 1

Introduction

1.1 Field Emission and High Voltage Breakdown

The investigation of anomalous electron emission and ultimate breakdown voltage between extended-area, vacuum insulated, metal electrode systems has been the subject of investigations for many years [1–4]. The performance of high field particle accelerators, electron sources, and pulse-power systems is limited by the emission and acceleration of unwanted electrons from the metallic surface into the vacuum. Initial investigations [4] revealed that low levels of current flowing between the electrodes preceded breakdown. The current increased with applied voltage, until an arc formed between the electrodes. Field emitted currents and subsequent breakdown between extended area electrodes was, and still is, believed to be the result of a reduction in the local work function of the metal surface, or in the enhancement of the local field strength. Field emitted currents can be sufficient to cause a localized heating of the cathode surface and gas desorption [5]. Electron bombardment of the anode may also release particles [6,7] and desorb gases into the vacuum gap [8]. The local charge carrier density (electrons and ions) in the vacuum gap increases, and arc formation occurs through an avalanche of secondary ions and electrons in the vacuum. The ability to maintain a stable high electric field is a limiting factor in many accelerator and electron injector applications. The exact mechanisms for the enhancement are not fully understood, but a physical picture of the localized emission sites on extended-area electrodes is becoming

clear [1,9].

At the Thomas Jefferson National Accelerator Facility, high voltage photo-electron guns are used for electron beam production. Figure 1.1 shows the schematic of the Free-Electron Laser electron gun. A wafer of GaAs is mounted on a molybdenum base. This base is mounted to a stainless steel or titanium cathode support structure. The cathode is biased to a high potential, typically 100 - 500 kV. A pulsed laser is used to emit the electrons from the wafer via the photoelectric effect. The electrons are then accelerated by the high electric field, usually ~2-10 MV/m, and exit the anode aperature.

Two parameters that are of interest in the design of an electron gun are the bunch charge and the emittance. For an pair of parallel electrode placed a distance d apart with a voltage $-V$ applied to the cathode, the magnitude of the surface charge per unit area on the surface of the cathode is $\sigma = \epsilon_o V/d = \epsilon_o E$, where ϵ_o is the permittivity of free space (8.85×10^{-14} F/cm), and E is the electric field. For an electric field on the order of a MV/m, the total amount of surface charge available is then 8.85×10^{-10} C/cm^2. The GaAs wafers used in the photoelectron guns are typically a few square centimeters, so this gives a total surface charge available of about 1000 pC. However, for pulse beam production, the complete removal of all the surface charge is not desired. Electrons near the back of a charge bunch experience a greatly reduced field, due to the shielding of the charges near the front. These electrons feel less electrostatic force than the ones near the front of the bunch, causing the momentum distrubution of the charge bunch to spread. The remedy is not to extract the entire surface charge, only a small fraction. This is accomplished by illuminating only a portion of the wafer with each laser pulse. The charge per bunch requirement for the FEL gun is 135 pC/bunch.

The high voltage is required to meet the design criterion for low electron beam emittance. The emittance of given beam is directly related to the spot size of the emitting area and the solid angle subtended by the beam. Due to space charge (the electrons' Coulomb repulsion from one another), an electron beam will try to expand as it travels

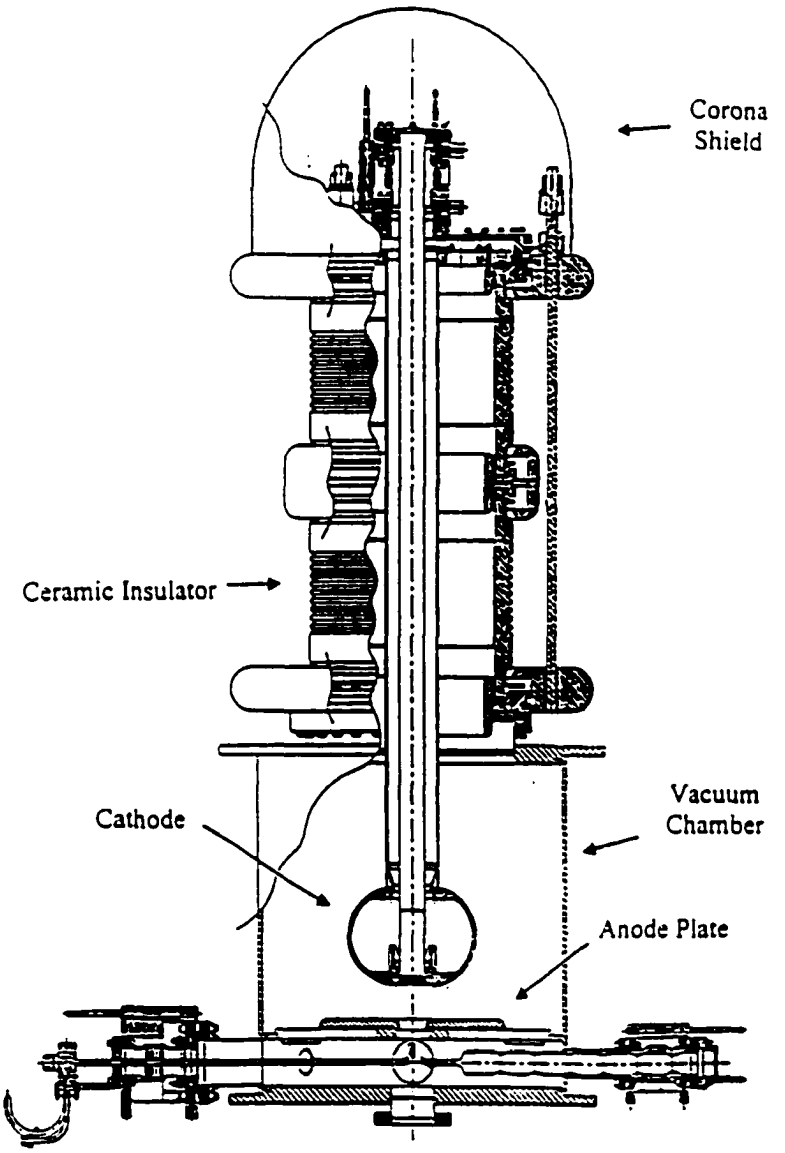

Figure 1.1: Diagram of the Free-Electron Laser Injector gun at Jefferson Labs.

from the cathode. A high voltage beam will travel more quickly toward its final target, and the time allowed for beam expansion is shorter than a low voltage beam. Thus, the high voltage electron beam will have less time to expand, and will arrive at the target with a lower emittance.

The high voltage and high field environment in these electron guns leads to anomalous field emission from the metal electrode support structures, limiting their maximum operating field through breakdown. The current solution is extensive hand polishing of all metal surfaces exposed to high potential gradients. Polishing has been shown [3] to decrease the prebreakdown current and to increase the ultimate breakdown field, and is a standard procedure in high voltage vacuum insulation. Although polishing reduces prebreakdown emission current, it is difficult, time consuming, and the results are unpredictable. The ultimate breakdown voltage of the guns is still, in the end, compromised by breakdown.

The electron guns are required to deliver high electron currents from the GaAs wafer, but only a few centimeters away, emission from the metal electrodes can lead to arc formation between the metal electrode support structures. These arcs can lead to surface damage that will further enhance the field emission. This can trigger more arcs, and ultimately lower the final operating field strength of the device. Arcs are accompanied by a sudden burst of gas pressure in the gap [5], which fuels the arcing activity. Figure 1.2 shows a secondary electron micrograph of a series of arc craters that occurred on a polished electrode surface. Note the sharp geometric protrusions that are caused by each arc, especially around the outer edge of the craters. The arcs that caused this damage occurred within a few seconds of one another. Sudden current surges from the arcs can destroy electronic devices or cause the high voltage power supply to deactivate due to an over-current fault condition.

Figure 1.2: SEM micrograph of arc craters formed on a stainless steel cathode surface. Note sharp protrusions at edge of crater.

1.2 Physical Basis of Field Emission

Field emission is a quantum mechanical phenomenon defined as the emission of electrons from the solid surface as the result of a high electric field [10]. In photoemission and thermionic emission, electrons are given enough energy to surmount the potential barrier at the surface. A high electric field, however, alters the shape of the surface potential barrier and allows conduction electrons to *tunnel* through the barrier. The field emission process can be discussed in terms of the energy bands in a metal. Consider the one dimensional potential energy band diagram in Fig. 1.3. The Fermi energy, μ, defines the highest filled energy level in the metal. The Fermi level lies a few electron volts above the bottom of the conduction band in most metals. This corresponds to an electron temperature of tens of thousand of Kelvins, making the Fermi level virtually independent of the lattice temperature. Thus, the Fermi energy determines a maximum energy of field emitted electrons [10]. The difference between the top of the Fermi level and the vacuum level is defined as the work function, ϕ.

The work function consists of two parts. The first is the contribution from the Fermi level. At absolute zero, the Fermi level refers to the energy of the most energetic electrons in the metal. This can be considered as the free energy of the electron "solution". The second part is a contribution arising from the redistribution of electrons at the surface of the metal. The latter effect is smaller, but not negligible. The electron wave function at the surface of a metal does not terminate abruptly (which would require an infinite amount of energy). Rather, the wave function extends into the vacuum as shown in Fig. 1.4. This negative charge cloud extends about 1 Angstrom above the surface into the "vacuum". This slightly depletes the negative charge just inside the metal, leaving a small positively charged zone. The resultant charge distribution results in an additional electric field barrier that the electron must surmount in order to be pulled from the metal. Electrons with kinetic energy E_x will face a barrier of height $\phi - E_x$.

Consider the one dimensional potential energy diagram in Fig. 1.5. An applied

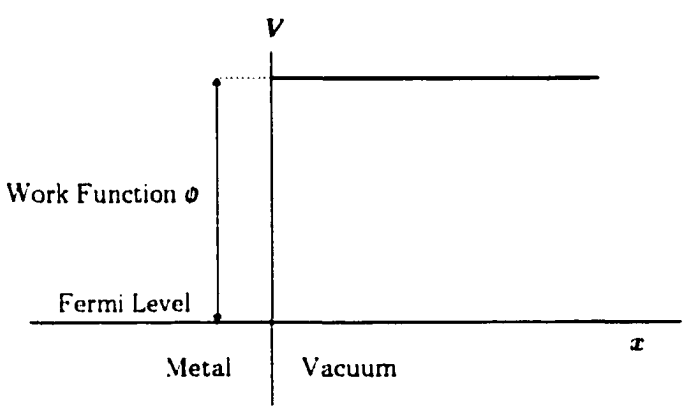

Figure 1.3: Field-free potential energy diagram for the metal-vacuum interface.

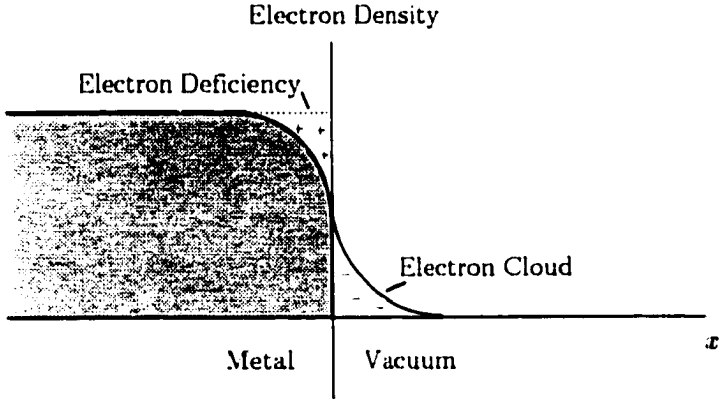

Figure 1.4: Surface dipole layer from an atomically smooth surface.

electric field, $E = V/d$, is placed at the metal-vacuum barrier. Electrons in the metal will now a face a barrier of thickness $(\phi - E_x)/eE$ and height $\phi - E_x$, where e is the charge of the electron. Also shown in Fig. 1.5 is the effect of the image charge on the barrier. The image charge is due to the induced charge an escaping electron creates on the metal surface. The image charge is opposite in sign, so electrons are pulled back into the metal by this induced charge. The magnitude of the image force is inversely proportional to the square of the electron's distance from the metal. It is effective for only a fraction of an Angstrom from the surface.

The Heisenberg uncertainty principle can be used to estimate the penetration of electrons through the barrier. An uncertainty in the electron's position Δx implies an uncertainty in momentum, Δp, by the relation

$$\Delta p \times \Delta x \approx \frac{h}{2\pi} \tag{1.1}$$

where h is Planck's constant. For electrons at the Fermi level, the maximum uncertainty in momentum can be derived from the height of the barrier, ϕ, as $\Delta p \sim \sqrt{2m\phi}$. If the barrier thickness for electrons at the Fermi level, ϕ/eE, is equivalent to the uncertainty in position

$$\Delta x \approx \frac{h}{2\pi\sqrt{2m\phi}}, \tag{1.2}$$

then one can obtain

$$\frac{\phi}{eE} \approx \frac{h}{2\pi\sqrt{2m\phi}}, \tag{1.3}$$

or,

$$E \approx \frac{2\pi}{e}\sqrt{\frac{2m}{h^2}}\phi^{3/2}. \tag{1.4}$$

A Typical value for the work function is 4 eV. This requires the field to be on the order of 7×10^{10} V/m for low level emission. Although this simple view of field emission overestimates the field required for emission levels for clean, needle-like electrode systems by an order of magnitude, it does give a physical picture of the nature of field emission.

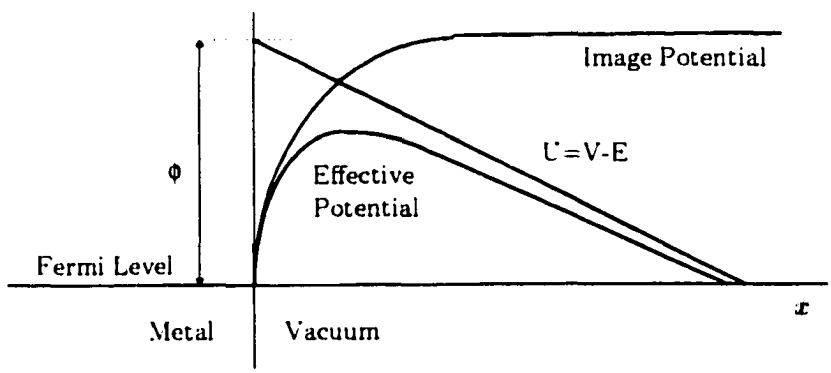

Figure 1.5: Metal-vacuum potential barrier distorted by the application of an electric field E.

The Fowler Nordheim Equation

The Fowler-Nordheim equation [11] gives an accurate description of the current density from a metal surface as a function of applied field. This equation will be derived in Appendix A. The general form is:

$$j = C_1 \frac{\beta^2 E^2}{\varphi} \exp\left(-C_2 \frac{\varphi^{3/2}}{\beta E}\right) \tag{1.5}$$

where j is the current density in A/cm^2, E is the electric field in V/cm, φ is the work function in eV, E is the electric field in V/cm, and C_1 and C_2 are constants. β is the so-called enhancement factor that accounts for local field enhancement due to the geometric "sharpness" of the emitter. The Fowler-Nordheim equation is usually written as

$$\frac{i}{E^2} = C_1 \frac{\beta^2 a}{\varphi} \exp\left(-C_2 \frac{\varphi^{3/2}}{\beta E}\right) \tag{1.6}$$

where a is a the effective emitting area. Taking the natural log of the above relation yields:

$$ln\left(\frac{i}{E^2}\right) = \ln\left(C_1 \frac{\beta^2 a}{\varphi}\right) - \left(\frac{C_2 \varphi^{3/2}}{\beta}\right) \frac{1}{E}. \tag{1.7}$$

Thus, Fowler-Nordheim emission will yield a straight line when plotted as $\ln(i/E^2)$ vs. $1/E$. From the intercept and the slope of the line, the effective emitting area a and geometric enhancement factor β can be deduced.

This theory is well supported for clean metallic structures such as needle-like cathodes of known tip radii [12]. However, field emission from extended area electrodes begins several orders of magnitude below the predicted threshold [13, 14]. Much evidence on broad area electrodes has shown that initial field-induced emission originates from some or all of the following: sharp microprotrusions [3, 15], surface defects [16], and contaminants [1, 13, 17–19]. Field emission from broad-area electrodes is erratic and unpredictable, and there exists no methodology for predicting the eventual gap breakdown. However, techniques have evolved to increase the ultimate breakdown voltage in HV electrode configurations. Most involve high levels of mechanical or electro-polishing [20] followed by some cleaning procedure to reduce the pre-breakdown emission [3]. Efforts have also been

made to coat the electrode surface with an insulating thin film [21,22] or to treat the electrode surface with an intense electron beam [23]. These methods have improved in the ultimate breakdown voltage for metal electrode systems, although they can be expensive, very time consuming, and fail to give consistent results between systems. These methods produce breakdown voltages that are still, at best, an order of magnitude below the Fowler-Nordheim threshold.

When high levels of emission current are measured between extended area electrodes, a common practice is to assume a sharp microprotrusion on the surface has caused a localized field enhancement $E_{Enh} = \beta E$. The field at the tip of this structure is then assumed to be sufficient for Fowler-Nordheim emission. It is reasonable to believe that an electrode surface of several hundred square centimeters, although carefully polished to a mirror finish, could still support geometric structures capable of high field enhancements. A work function for the material is assumed, but values for ϕ can vary between crystalline surfaces [24] in a metal and be highly dependent on the amount and nature of gas coverage [25]. Current and field data are usually plotted according to the Fowler-Nordheim equation, and values are obtained for emitting area a and field enhancement factor β. However, dubious results have often been obtained with this procedure when applied to extended-area electrodes; calculated values for the emitting area a are often orders of magnitude larger than the electrodes themselves [17]. Also, many SEM imaging studies have failed in the past to locate sharp microprotrusions that are suggested for high β values [26]. Some researchers are revisiting the microprotrusion model [14], and claim that micropoints could form and be destroyed by microdischarge activity on time scales too short to be detected [8]. The operating conditions, e.g. the presence of oil diffusion pumps, has been shown [18] to dramatically increase the level of pre-breakdown current. Gases present in the vacuum environment also show an effect [25] on the stability of field emission and linearity of the data with the Fowler-Nordheim equation.

The Fowler-Nordheim equation, although adequate for describing emission from

clean, needle-like points of known geometry and work function, can not account for the field emission behavior of extended area electrodes. A complete literature review of experiments from extended area electrodes is given in Chapter 2 of this thesis.

A common technique for reducing the levels of field emission between electrodes is "conditioning". During conditioning, the energy available for arc formation (i.e. the stored energy in the high voltage power supply and associated cabling) is limited by the insertion of a current limiting resistor. The voltage is slowly increased to allow field emitted electrons and microdischarge activity to destroy, by localized heating, the microprotrusion or other sites responsible for the emission [8, 20, 25]. With each increment of voltage, field emission levels are allowed to subside before continuing to the next voltage plateau. The conditioning process is continued until the emission current has dropped to an acceptable level (no measureable pressure increase or current above the detectable limit) at a voltage somewhat above the operating voltage. Only then is the current limiting resistor removed for device operation. In practice, however, conditioning can improve the voltage hold-off capabilities of the system only so far. Some emitter sites are stable and will not be affected by conditioning. High levels of emission currents ($> 10^{-6}$ amperes) will begin to desorb gases from the electrode surfaces, contaminating the vacuum system. This is highly undesirable in system such as the photo-electron guns discussed earlier, as gas contamination of the GaAs wafer will poison the cathode and reduce its effective life-time. A more favorable solution is an *ex situ* process that would eliminate the need for conditioning, and provide more reliable and consistent operating conditions at high voltages and high field strengths.

1.3 Plasma Source Ion Implantation

Nitrogen ion implantation is a common procedure for hardening the surface of medical implants, automotive parts, and tool steels. Typical beam implantation involves rastering a high energy focused beam of ions across the workpiece surface. At energies above 10 kV, substantial implantation takes place to depths of several hundred Angstroms. Ni-

trogen ion implantation has been shown [27,28] to increase the hardness and wear rate of metals through the formation of nitrides. In order to process a non-planar surface, however, one must be able to move the work-piece in a very controlled manner in order to obtain a uniform implantation. This leads to the development of very complicated translational and rotational stages. Rastering of the ion beam is also necessary, as well as masking of the beam to prevent off-angle impact and sputtering.

An alternative to conventional beam implantation was developed at the University of Wisconsin in 1987 by Conrad et al [27]. The workpiece to be processed is submerged in an ambient plasma of the species to be implanted. The piece is then pulsed with a series of negative, high voltage pulses a few microseconds in length at a repetition rate of 10 Hz to several kilo-Hertz. Ions in the plasma are accelerated by the applied field and implanted into the workpiece. The shape of high voltage electrodes found in medical X-ray tubes [29] or electron sources is often very critical in tailoring the local field strength. Electrodes, therefore, have rounded, smooth shapes. The proposed surface treatment, Plasma Source Ion Implantation, or PSII, is appropriate for the processing of such high voltage electrodes. The benefits of plasma source ion implantation, or PSII are:

- Ions follow the electric field lines and are therefore implanted normal to the surface.
- No complicated rastering or sample manipulation is necessary
- Large pieces can be more easily processed.

The motivation for processing electrodes with ion implantation is based on the the general practices of workers in the field. The materials that have become "accepted" are stainless steel and titanium. Latham [1, pages 48, 49] points out the similarity between these electrodes in their oxide layers. Both materials have ambient oxide layers that are insulating and highly resistant to corrosion. Ion implantation has been shown [30] to increase the corrosion stability of stainless steel. Williams [31] *et al* have observed a reduction in electrochemical corrosion currents in titanium alloys by more than two orders of magnitude.

Hardness may also be a factor, as generally accepted electrode materials have a hardness number > 300 on the Vickers scale. Ion nitriding of steel has been shown [27,32] to increase the hardness of tool steels and surgical implants. The smoothness of the materials is also a factor [3], and ion bombardment during the PSII process may reduce the number of protruding emitter sites.

This thesis will present the design and operational considerations for The William and Mary PSII system, the effects of nitrogen implantation on the field emission characteristics from processed metal electrodes, and theoretical considerations for the field emission behavior from the modified surface layer.

1.4 Organization of this Thesis

The goal of the work will be to ascertain the effects of PSII on the pre-breakdown field emission characteristics of stainless steel electrodes. This will be accomplished by the following:

- Consider the design parameters for the William and Mary PSII system. Understand the pulse forming network, plasma parameters, and pumping requirements.
- Characterize the operation of a thermionic-emission driven plasma by direct *in-situ* measurement of ion densities and electron temperatures.
- Characterize the performance of the WM-PSII system. Compare implant depth profile predictions from calculations with Auger Electron Spectroscopy depth profiling.
- Perform *in situ* field emission experiments on small scale test electrodes in ESCA system. Detailed surface spectroscopy will help elucidate effects of modified surface layer on electrode performance.
- Design and construct a large-area electrode (6" diameter) test facility at Jefferson Laboratory. This system will be used for future investigations of surface modification

techniques for high voltage electrodes.

- Propose a physical basis for field emission behavior from implanted electrodes.

Chapter 2 of this work will present past experimental efforts to detect and analyze emission sites from broad area electrodes. Also, current models developed to explain field emission behavior from such systems will be reviewed.

The design considerations for the William and Mary Plasma Source Ion Implantation facility will be described in Chapter 3. The dynamics of the plasma during the high voltage pulse will be presented. Dose calculations, TRIM modeling, and Auger depth profiling of implanted samples will be compared.

Chapter 4 of this work will describe the modeling and design work for the small scale field emission test platform at William and Mary, and the large area test platform at Jefferson Laboratory.

In Chapter 5, the experimental procedures and data will be presented for the field emission experiments. Data from treated and untreated electrodes will be presented, as well as data from some alternative surface treatments.

Chapter 6 discusses the results and their possible bearing on future modification techniques for field emission suppression. Modifications are suggested for the W & M PSII system. Also, a discussion of future directions in field emission suppression is presented, including outlines of possible improvements in design based on this work.

Chapter 2

Theory

2.1 Enhanced Electron Emission

The Fowler-Nordheim equation for electron tunneling has been successful, to a degree, in describing the electron emission from small, needle-like electrodes [12]. However, electron emission from extended-area electrodes, where the source of the emission is not known exactly, begins at field strengths several orders of magnitude below the Fowler-Nordheim prediction. Early work [4] in pre-breakdown emission attributed this anomaly to sharp protrusions enhancing the local field. The data was fitted to the Fowler-Nordheim equation, and the shape of the protrusion deduced from the slope and intercept of the equation. The first section below reviews this method from an early investigation by Williams *et al* [3]. Recently, experimental systems have been constructed [1,3,17,19] to locate and identify the source of the anomalous emission. The following sections address past experimental evidence concerning emission behavior from extended-area electrodes. Physical models that attempt to explain anomalous emission are reviewed.

Surface Finish

Williams and Williams investigated the effect of the electrode surface finish on pre-breakdown current [3]. Pre-breakdown current was measured for hand-polished, lapped,

electropolished, and unpolished electrodes under similar vacuum conditions. The results showed that hand polishing was the most effective at reducing the level of emission current at a given field, then lapping, then electropolishing. Electrodes with no surface treatment gave the highest field emission levels. The data were fitted to the Fowler-Nordheim equation, and the two fit parameters, a, and β, were determined from the intercept and slope of the line, respectively. The fitted data are shown in Fig. 2.1. Results such as these encouraged workers to continue to fit emission data from extended area electrode to the Fowler-Nordheim law.

The work function ϕ is also a fit parameter in the Fowler-Nordheim equation, because the exact source of emission in plane-plane electrode systems is usually unknown. The emitter geometry deduced from these plots is of cones 2-3 μm in height, and $\sim$ 10 nm in base diameter. No Scanning Electron Microscope (SEM) analysis was performed on these samples to confirm the existence of the whisker-like protrusions. This method of deducing the geometry of a "sharp" microprotrusion based on the Fowler-Nordheim equation was typical of early work in electrode breakdown studies [19]. As will be seen in the following sections, this method cannot be used to explain most of the behavior of anomalous emission from extended area electrodes. In fact, the sharp protrusions are rarely found.

Imaging Techniques

N. S. Xu and R. V. Latham [9] used a transparent anode to visually monitor emission and breakdown activity between electrodes. Oxygen free, high conductivity (OFHC) copper samples were used as the cathode (15 mm diam.), and a tin-oxide coated window as the anode (30 mm diam) in an plane-plane electrode configuration. Figure 2.2 shows the experimental system. Electrons from emission sites were accelerated by the applied field in the gap, and generated a fluorescent spot on the tin oxide anode. This created a spatial "map" of the emitter sites. A 25 Hz frame rate video camera and image analyzer were used to record the emitter distribution and breakdown events in the plane-parallel electrode setup. With simultaneous electrical recordings of breakdown events, workers were able to

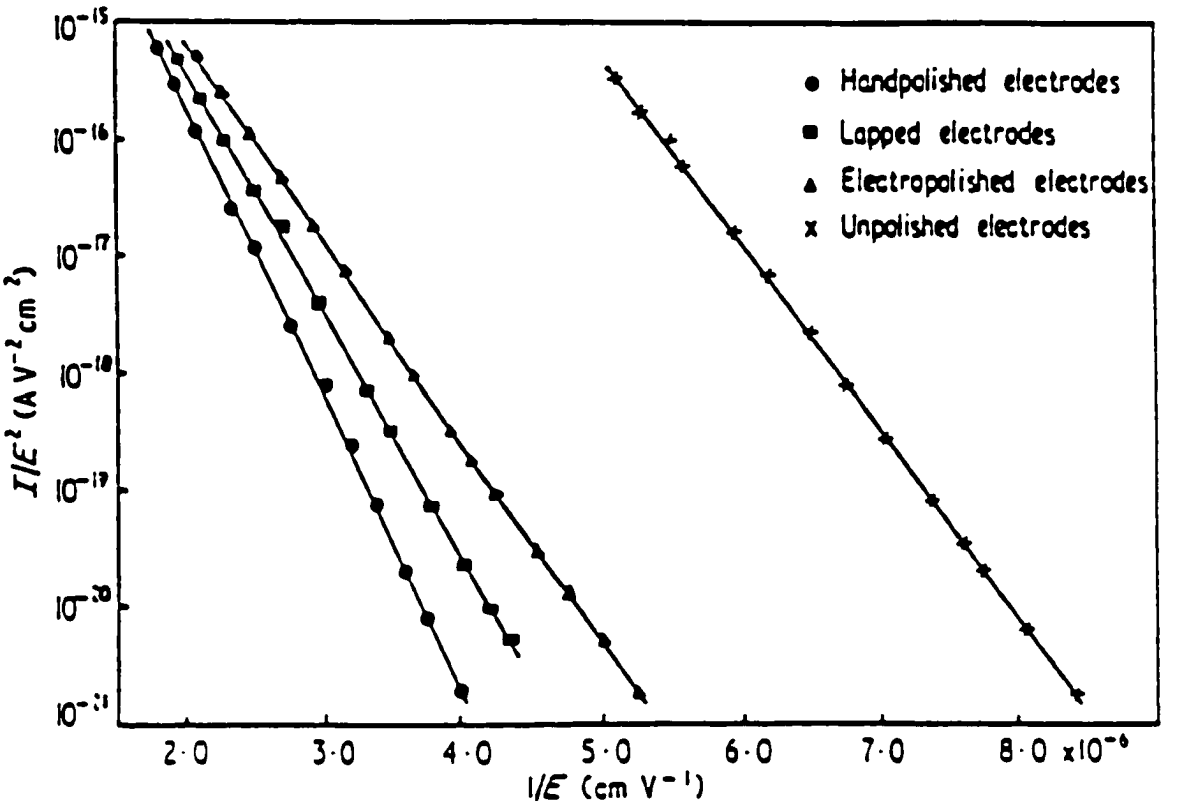

Figure 2.1: Data from hand-polished, lapped, electropolished, and unpolished electrodes plotted to the Folwer-Nordheim equation. From Williams and Williams [3]

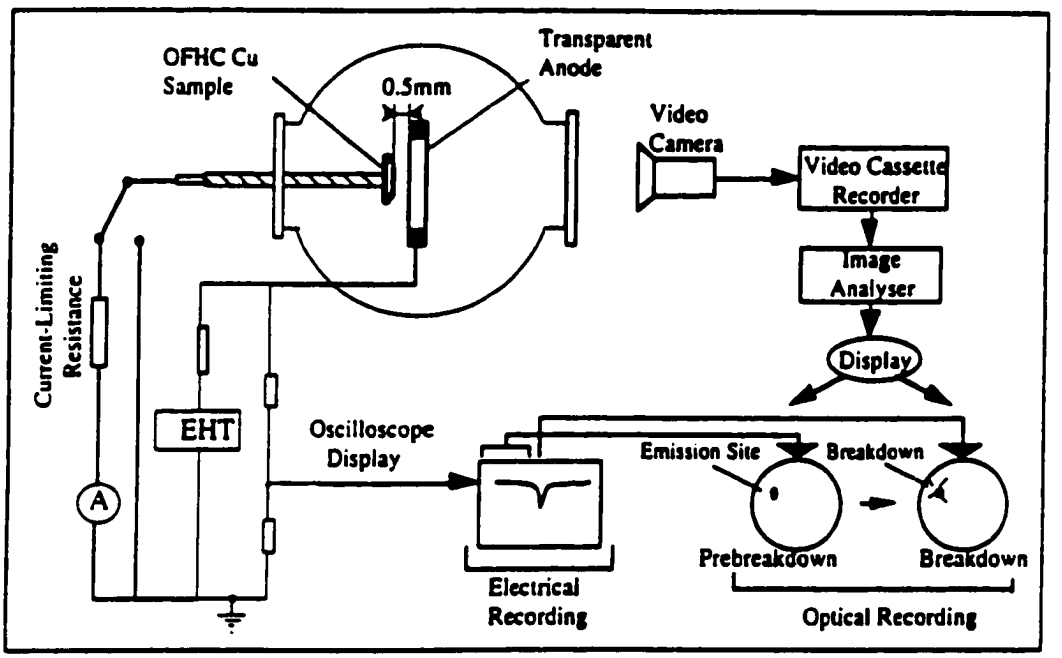

Figure 2.2: Transparent anode technique employed by Xu and Latham [9]. Anode is a tin-oxide coated window that will fluoresce when struck by electrons. Spatial distribution of emission sites and breakdown activity can be obtained.

make a direct correlation between the spatial and temporal characteristics of pre-breakdown emission sites and direct current breakdown events.

The voltage on the cathode was slowly increased until the initial "switch-on" field was reached (~10-20 MV/m), and emission sites were observed on the video screen. The images showed a few discrete sites. When the specimen exhibited stable, reversible, current-voltage characteristics, the voltage was removed and the cathode grounded. The voltage was increased to produce an arc. An oscilloscope was set to trigger on a negative-going pulse and the video camera recorded the optical emissions from the tin-oxide window. It was found that the breakdown field of the primary discharge is usually less than the switch-on field of the corresponding emission site. This observation suggests that emission current changes the state of the electrodes. Video recordings of the emission sites and breakdown events revealed: (i) the breakdown discharge location directly correlates with its particular emission site, with only one direct current breakdown site, and (ii) a primary discharge triggers a number of secondary events at random locations in the gap. For multiple discharges, it was observed that the average rate of discharges as recorded by the oscilloscope was higher than the sampling rate of the video camera, so they could not be optically resolved. However, it was observed that a second discharge occurs after the gap voltage is re-established after a "dwelling-time" of about 50 ms (i.e. there has been an irreversible change to the gap due to the arc). This study showed that 80% of all breakdown sites were spatially correlated with the site of the pre-breakdown emission.

Hurley *et al* investigated electroluminescence from d[illegible]e regions on the surface of high purity metal cathodes [16,33]. Electroluminescence is due to excitation of electrons in an insulator to the conduction band by electron impact ionization. The excited electrons gain energy in the electric field. If an electron drops back to the ground state, or some intermediate state, a photon is emitted. In these experiments, voltages of 130 kV DC, or 15μs 130 kV pulses, were applied across a 2-8mm gap. The electrode materials studied were commercial grade molybdenum, H15 duraluminium, stainless steel type EN58B, high purity

copper (Johnson and Matthey Puratronic grade 1), and high purity gold (Mat. Res., Marz grade). In the report, spots emitting light were referred to as "k-spots" to distinguish them from areas where arcing occurs. These workers claimed that impurities play a major role in breakdown initiation and electroluminescence. Electroluminescence is associated with high resistance spots in semiconducting impurities. These high resistance spot could be a result of the so-called "electroforming" process, in which minute filamentary conducting channels are formed through semiconducting or insulating layers on the surface.

Energy Spectra

Energy spectra of electrons from localized emission sites have been measured by several workers [1, 9, 13]. Modified electron microscopes and field emission scanning microscopes were fitted with electron energy spectrometers. Emission sites were located on the surface, and the energy spectrum measured. Figure 2.3 shows a spectrum from an emitting structure of a copper-chromium cathode in work by Allen *et al* [13]. The nature of the emitting site was not known exactly, but X-ray analysis showed iron and aluminum impurities. Curve A in figure 2.3 was obtained from a clean tungsten tip. Curve B is the spectrum from the emission site. Curve C was obtained after a 24 hr period. The sample was heat treated to ~700 °C, and the double-peak spectrum of curve B reappeared.

The authors state that the spectrum is similar to that of semiconductor emitters. Due to the localized nature of emission sites, Allen and coworkers discount the theory that the native oxide layer of the material is responsible, but rather assume the presence of small dielectric inclusions in the material. A three stage model is proposed to explain the emission, and a schematic of the electronic "element" is shown in Fig. 2.4. The emission mechanism is based on the tunneling of electrons into the conduction band of the semiconductor, subsequent heating of the electrons by the applied field, and emission of the electrons from non-equilibrium states on the surface. The appearance of the double peak was ascribed to possible effects of adsorbed gases on the emission site.

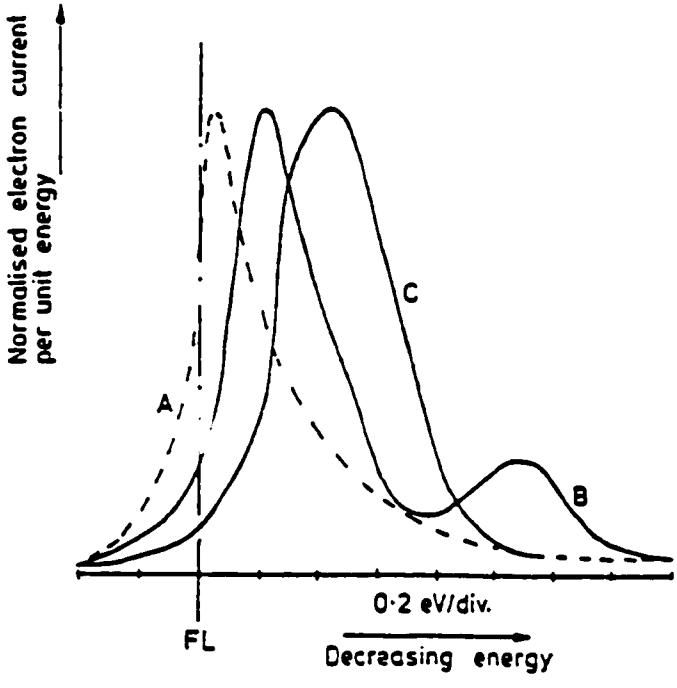

Figure 2.3: Electron energy spectrum from emitting site on broad-area copper-chromium electrode. Curve A is spectrum from a clean tungsten tip. Curve B is the double-peak spectrum from the site when the specimen was first installed. Curve C was taken after several a 24 hour period. The samples was heated to ~700 °C. A trace similar to B was then measured. From Al[illegible] *et al* [13].

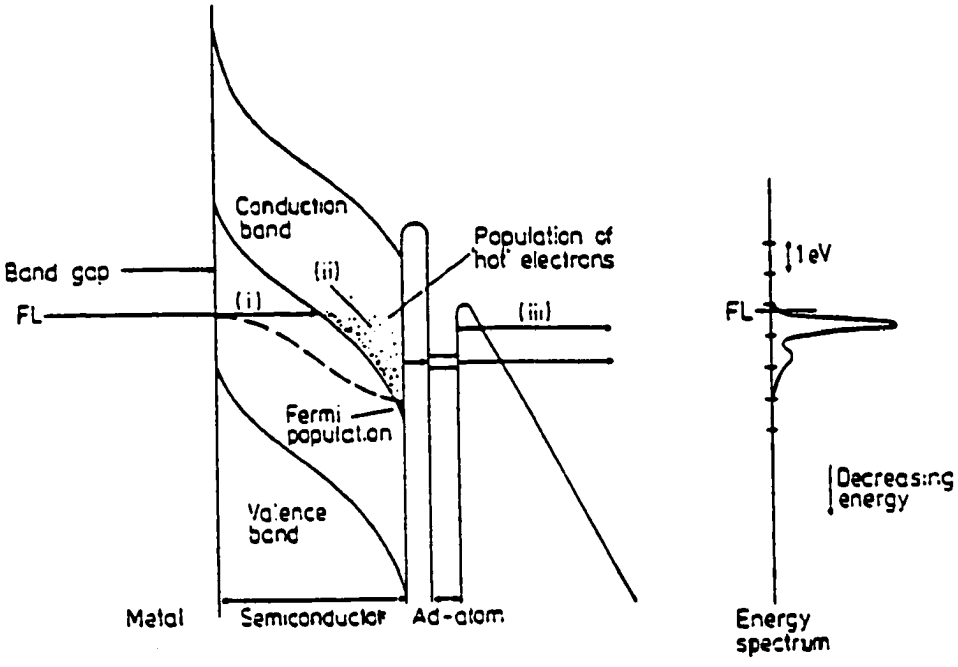

Figure 2.4: Band diagram for the model proposed by Allen and Latham. Initially, electrons tunnel from the metal substrate to the conduction band of the semiconductor. Then, the electrons are accelerated by the penetrating field. Finally, electrons tunnel from non-equilibrium states near the top of the surface potential barrier. From Allen *et al* [13].

Adsorbed Gases

The role of adsorbed gases on pre-breakdown emission was investigated by Kelsey in two different vacuum environments [18]. The first chamber was evacuated to 5×10^{-7} Torr with an oil diffusion pump. The electrodes were degassed by electron heating to 280° C. The second system was evacuated with zeolite sorption pumps and a 400 l/s ion pump. These pumps are oil-free. The base pressure of the system was less than 10^{-10} Torr. This system was baked to 400 °C. Electrodes for both systems were stainless steel. The anomalous emission currents in the oil-pumped system were up to 10^4 times greater at a given field strength than those in the oil-free system. The author states that, due to the unknown local gas pressure in the gap, it is difficult to account for the distinct performance of the two systems. However, this experiment indicates that the vacuum conditions may play a role in the behavior of the electrode system.

Probe Techniques

Pupeter *et al* have used probe techniques to isolate and identify surface features that produced unusually high levels of field emission from the cathode surface [17]. A biased anode probe was rastered across the surface of the cathode. The emitted current as a function of position was measured.

The field-emission scanning microscope (FESM) used in this work employed a small, flat tungsten anode. This was raster-scanned across the sample, and fields between 40 MV/m and 100 MV/m can be applied to the cathode surface. Higher fields, up to 200 MV/m were applied to larger areas (5 mm^2) to investigate weak emission sites. I-V characteristics were measured for each emission site and the two fit parameters, a and β, were calculated from Fowler-Nordheim plots. An average work function was assumed for the cathode material. SEM and AES determined the elemental composition and morphology of each emission site.

These experiments compared field-emission behavior from chemically and mechanically polished Nb, Cu, and Al cathodes. Data from the emission sites were compared to the Fowler-Nordheim theory. The values for a, the emitter area, had an unrealistic range of 1×10^{-17} to 6×10^{15} cm^2. The SEM revealed no sharp protrusions at the emission site. Instead, several different surface anomalies were observed: Inclusions in Al (with high concentrations of Si, Mg, Fe, and Mn), sulfur contamination on chemically etched Cu (sulfur content in OFHC copper ~5ppm), particles on Nb (carbon) and Cu (water rinse residue), surface defects on Nb, and craters created by discharge activity on all samples. The workers found no dependence of emission characteristics on cathode material within these five emission types.

Around 50% of the particles that showed enhanced emission were smaller than 0.5 μm. Mechanical polishing with final ultra-pure water rinsing of the copper was found to be very effective in the reduction of enhanced emission. Contaminant-free grain boundaries were not seen to cause enhanced field emission up to 200 MV/m. However, contamination was found at a majority of the emission sites for all the materials.

A similar technique was used by Cox *et al* [3.19]. A beam tracking technique and "probe-hole" SEM was used to investigate anomalous emission sites. In this apparatus, a biased movable anode with a small hole in it was rastered across the surface of a cathode. A small probe detected the electrons that passed through the hole. The SEM imaged any enhanced emission sites.

The cathode used was a polished stainless steel disk, roughened on a lathe (to create possible emission sites). The anode was a polished, 20 mm diameter plate with two probe holes of 500 mm and 5 mm diameters. Care was taken to keep the electrodes clean for UHV.

Emission sites typically delivered currents of 10 nA at 4.8 MV/m. The authors assumed that the emission was a result of field enhancement at the tip of a sharp microprotrusion. Fowler-Nordheim plots gave an enhancement factor β of 735, and an emitting

area of 0.5 fm^2. These parameters correspond to either a conical (29 μm high, 0.02 μm tip radius) or cylindrical (11 μm high, 0.015 μm tip) projection. The resolution of the SEM was about 0.1 μm, so at least the base of the conical projection could have been seen. However, SEM micrographs showed no such protrusions on the surface. Instead, a small insulating particle 5 μm in diameter was found. The field was increased to 12 MV/m, whereupon the current suddenly dropped to 10 picoamperes. Upon further SEM viewing, the particle had disappeared (evidence of the "conditioning Effect"). Three additional emission sites were detected on the roughened cathode surface. No particles were resolved at that time under SEM viewing, but the emission area was covered with machining marks from the lathe tool.

Jimenez *et al* have investigated emission from selectively contaminated cathode surfaces [15]. Similar to the FESM, a tungsten anode was scanned over the surface of the cathode to locate emission sites. SEM and Energy-Dispersive X-ray spectroscopy (EDX) were used to identify the emission site.

Emission sites from electropolished Nb and mechanically polished gold cathodes were examined. Some of the Nb samples had been anodized to grow thick oxide layers. The samples were contaminated with $\sim$ 20 μm particles of various composition: insulators (Al_2O_3, SiO_2), metals with conducting surfaces (Ag, Au, Fe), and metals with insulating oxides (Nb, Ti).

The insulating particles, Al_2O_3 and SiO_2, showed substantially lower emission currents than the metallic particles on any given substrate. The particles that gave the highest emission currents were those with naturally oxide free surfaces (e.g. Ag, Au), or those with thin conducting oxides (e.g. Fe). Particles with insulating oxide layers, Nb and Ti, showed low levels of emission under the range of fields. The presence of a thick oxide layer on the Nb cathodes showed little effect on the individual emission behavior of the particles. Strong emission was also seen from Au particle on Au substrates. In addition, particles with insulating oxide layers lost their capacity to charge under the SEM beam after they had emitted. The authors speculated that the emission currents may have rendered the

oxide layer conductive.

These experiments reveal that the particle-vacuum interface plays a larger role than the particle-substrate interface. The author tentatively ascribes the results to the metal microprotrusion model. The geometric enhancement to the electric field from the projections on the surface of the particles would increase the tunneling current. This model, however, still does not explain the magnitude of the emission currents. It is important to note that the background pressure in these experiments was in the range of 10^{-5} to 10^{-7} Torr. The authors did not report removing the adsorbed adventitious carbon and water layer, that forms from air exposure, from these samples by a heat cycle. If the samples were heated to remove this layer of gas, a monolayer of adsorbed gases from the chamber would nevertheless form in approximately 0.1 second at 10^{-5} Torr (1 sec at 10^{-6} Torr, etc.). In either case, the samples were likely to be coated with a thin layer of hydrocarbon and water in this pressure range. As will be discussed in a later section, adsorbed gas plays a major role in enhanced field emission.

Results from several investigations into the nature of field emission sites have revealed that, almost without exception, the emitter is closely associated with a foreign particulate. Shown in Table 2.1 are results from several studies. The cathode material, the presence of its oxide, the emitters found, and the presence of their oxide is given. A plethora of work has been done to locate and analyze (both structurally and chemically) emitter sites on extended area electrodes. The data in Table 2.1 reveals that, with exception, the presence of an insulating oxide layer may play a role in field emission suppression. Indeed, the most "popular" materials for high voltage electrode design are stainless steel and titanium, both of which have very hard, resilient oxide layers. Jimenez *et al* [35] observed the effects of exposing a damage site, created in vacuum by a diamond indentation, to air for oxidation. The damaged gold cathode (Au does not form a native oxide), showed stable and repeatable emission behavior before and after exposure to air. Emission from niobium, which does form a native oxide, showed variability after the air exposure, suggesting some effect by the native

Investigator	Cathode Material	Oxide	Emitters	Oxide
Niedermann *et al* [34]	Niobium	Yes	C	No
			S	No
			Mo	No
			Ti	Yes
			Ag	No
Pupeter *et al* [17]	OFHC Cu	No	S	No
	Al	Yes	Al, Mg	?
Allen *et al* [13]	Cu-Cr Alloy	?	Al, Fe	?
Noer *et al* [35]	Nb	No	C	No
			S	No
			MoS_2	No
Jimenez *et al* [15]	Nb	No	Ag, Au	No

Table 2.1: Results from several investigation on localized emitter composition.

oxide. It is true, though, that materials that form conducting or semiconducting oxides, such as high-purity vacuum-melted copper [19], do not show copious levels of emission, without the presence of contaminants. Further studies are needed to elucidate the effects of an insulating oxide layer in field emission suppression.

Another phenomenon associated with high voltage vacuum insulation, that of microparticle transport across a high voltage gap, is reviewed in the next section.

2.2 Microparticles

Microparticles have been regarded as a source of breakdown [6] between metal electrodes. Electric field of sufficient strength cause microparticle detachment and acceleration of the particles across the gap. Upon impact, the particle dissipates its energy as heat or mechanical shock. Electrode material may vaporize. If the amount of material expelled into the gap is above some critical value, an avalanche of charged particles will ensue, and an arc may form. Often seen in high voltage electrode experiments is a rapid "turn-on" effect. Turn-on is characterized by a rapid increase of current of several orders of magnitude. Microparticle impact creates crater damage on the surface [7] and may be a source of contamination, which may lead to the emission sites often seen in probe investigations.

The charge and velocity of microparticles from outgased, polished electrodes has been measured by Texier [7]. To estimate the charge on a microparticle, half-spheroid particle shapes were assumed with a major axis a and minor axis b. The particle then gets an amount or charge Q according to the relation:

$$Q = \pi \epsilon E b^2 \beta(\lambda). \tag{2.1}$$

The λ in the function $\beta(\lambda)$ is the ratio of half-major to half-minor axis of the half-spheroid particle. The mass of the particle is written as density times volume, and deduced from the experimental procedures.

The experiment consisted of a stainless steel grid (0.15 mm wires 1.5 mm spacing) serving as one electrode. The opposite electrode, copper or tin, was spaced 5 mm from the grid. After a particle had passed through the grid, it moved through the electrostatic detector, which consisted of a series of cylinders: a trigger cylinder, the detecting cylinder, and two guard cylinders. A charged particle moving through the cylinders induces a charge Q by electrostatic influence. This signal was amplified and recorded. The particle finally impacted on a collector plate for later identification.

The size of the detected particles ranged from fractions of micrometers to 8 micrometer and sometimes more. The velocity ranged from a few m/s (large particles) to about 200 m/s. The threshold voltage for particle emission varied, ranging from a few kV up to 50 kV (10 MV/m). Microparticles were observed during times of constant voltage, but most were emitted during a voltage increase. The total number ranged from a few to about a hundred for freshly polished electrodes.

Microparticle identification was done through optical metallography. With a copper anode and stainless steel collector, yellow-red microparticles were observed on the surface of the collector, apparently Cu. For a tin anode with Ti collector, tin spots about 4 microns in diameter appeared on the collector. Larger Al spots and some iron were also detected. These were assumed to be impurities in the anode material. Particle were observed from both cathodes and anodes.

Microparticles may be responsible for the so-called Total Voltage effect [8]. This effect is based on experimental evidence that shows a relationship between the breakdown voltage and the gap spacing of a given electrode system. At low gap spacing ($d < 0.5mm$), a linear relationship exists between breakdown voltage and gap spacing:

$$V_b \propto d \tag{2.2}$$

For larger gap spacing, $d \geq 2.0mm$, a non-linear relationship takes over:

$$V_b \propto d^{\alpha} \tag{2.3}$$

Where $\alpha < 1$. This dependence on breakdown voltage has been empirically verified by several investigations [6, 36].

2.3 Field Emission Models

Most experimental evidence has shown that the location of emission sites on extended area electrodes is strongly correlated with surface anomalies. Several observations have been made concerning the local emission sites:

1. Unreasonable geometric enhancement factors, β, and emitting areas, a, are deduced from the Fowler-Nordheim equation.

2. Electron energy spectra from emitters on broad-area electrodes do not match those of known metallic emitters.

3. Electroluminescence, a non-metallic phenomenon, is often observed from emission sites.

4. Presence of foreign particles or inclusions in the material near the emission sites.

These observations have led Latham and co-workers in developing [1] the Metal- Insulator-Metal (MIM) model and the Metal-Insulator-Vacuum (MIV) model. These studies are based on results obtained from experiments that measure the spatial distribution of emission sites,

their chemical nature, and the energy distribution of the emitted electrons. These emission models contrast the traditional model of enhanced fields via sharp microprotrusions, the so-called Microprotrusion Model (MM). The physical basis leading to the development of these model will be reviewed in the following sections.

2.3.1 The Anomalous Emitter Structure

The past experimental evidence indicates anomalous emission sites on an extended-area cathode surface are not simple metallic structures. Several investigations have indicated emitters are contaminants resting on the surface of the electrode, or "built-in" dielectric inclusions. It is certainly possible that both these structures be present on a cathode surface. To begin to understand how a dielectric structure could be involved in emission of electrons due to an strong applied field, a generalized metal-insulator-vacuum structure is drawn in Fig. 2.5.

Insulators are usually thought of as having very few mobile charge carriers. In practice, however, the "band structure" of insulators, or the discrete levels of energy in the material, is slightly blurred due to structural imperfections and impurities. The insulating emitter sites and oxide layers found on broad-area electrodes are usually amorphous and impure. In this case, the insulators take on "semiconductor-like" properties [37]. Some insulators, including many oxides (SiO_2, Al_2O_3) may have a relatively high charge carrier density. The carriers, however, are trapped at these structural imperfections, and the insulating nature stems from the low mobility of the carriers. In the context of the anomalous emitter structure, a description of charge injection into and transport through a semiconductor will be reviewed in the following sections. First, attention is turned to the energy band diagrams of metals, insulator, and semiconductors.

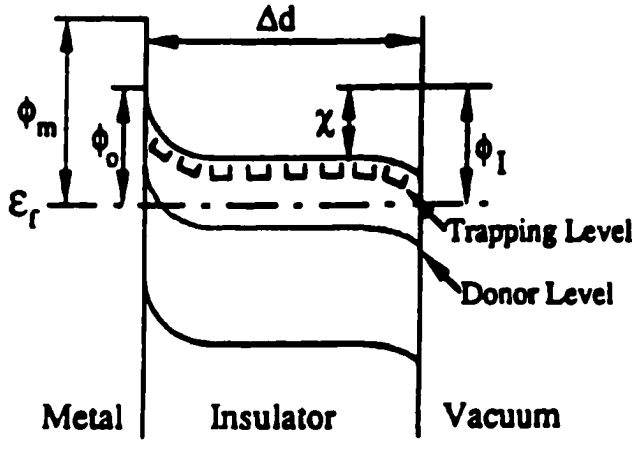

Figure 2.5: The general metal-insulator-vacuum structure used for discussion. The insulator can be an oxide layer or some dielectric inclusion in the surface.

2.3.2 Energy Band Diagrams

Metals, semiconductors, and insulators are characterized by the position of their valence and conduction band energy in the solid. Energy band diagrams are useful in describing the electronic properties of materials. Figure 2.6 represents the energy band positions for each material. In a metal, the conduction bands and valence bands overlap, so some electrons are free to move about the metal and contribute to the conduction of the material. Pure insulators are characterized by a large gap between the conduction and valence band ($\sim$ 5-10 eV). The conduction band is empty, so there is no substantial electron current flow at room temperatures. Semiconductors have a small gap, on the order of E_g = 1 eV. The conduction band is mostly empty, and the valence band is mostly full. The conductivity of a pure semiconductor is due solely to the electron movement in the conduction band, and the motion of positive "holes" in the valence band. Holes can be considered as positive charge sites created by the absence of an electron. This type of pure semiconductor is called *intrinsic*. Silicon and germanium are examples of intrinsic semiconductors.

An *extrinsic* semiconductor is created by introducing a chemical impurity in the lattice with one more or one less valence electron than the host atom. The addition of these impurities create new "states" within the energy band gap. For example, if phosphorous, with 5 valence electrons is added to silicon, with 4 valence electrons, an additional electron will be present for each impurity. This type of impurity is called a "donor". An electron state will be created just below the bottom of the conduction band. These electrons can be freed with a small amount of energy ($\sim$ 25 meV) and enter the conduction band. This type of semiconductor is termed *n-type*. If boron, with 3 valence electrons, is added to silicon, a hole will be created for each impurity site. This type of impurity is called an "acceptor". The hole states are created just above the top of the valence band. As with electrons, holes can be excited to conduct electricity with small amounts of energy. This type of material is termed *p-type*. The Fermi energy of an intrinsic semiconductor lies at the midpoint of the

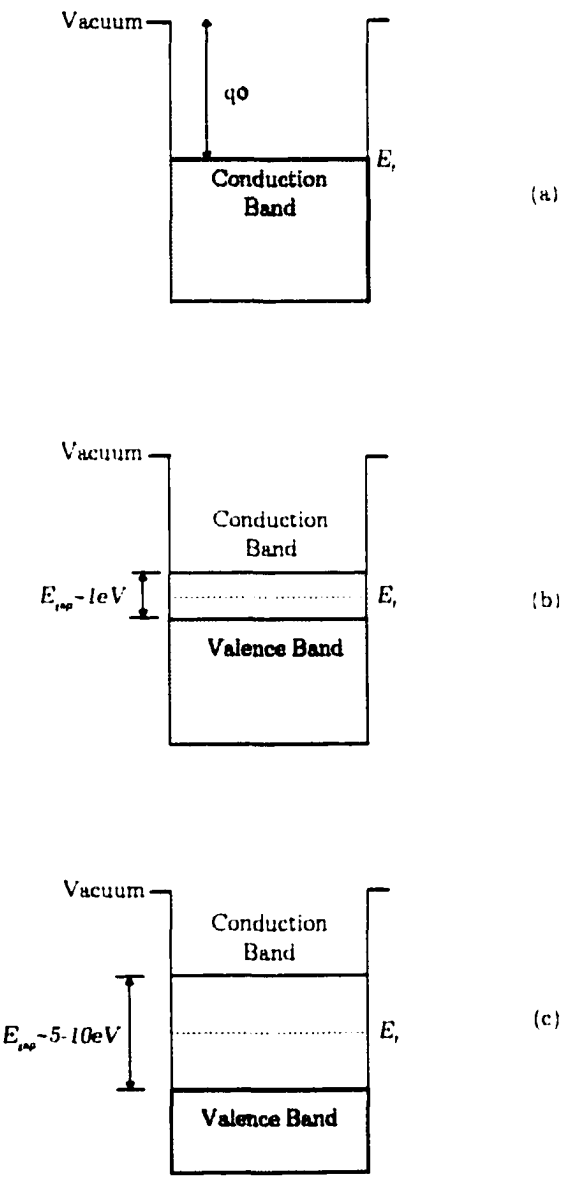

Figure 2.6: Energy bands for (a) a metal, (b) a semiconductor, and (c) an insulator.

gap ($E_f = (E_v + E_c)/2$). When the material is doped with acceptor atoms, E_f lies below the mid-gap energy. If the dopant is a donor atom, the Fermi level lies above the mid-gap energy. The band diagrams for n-type, p-type, and intrinsic semiconductors are shown in Fig. 2.7.

The energy band diagrams are useful in understanding the electron transport through metal-semiconductor barriers and electron emission in vacuum from semiconductor-vacuum surfaces. The current models for enhanced field emission consider the emitting structure as an n-type semiconductor (high density of "donor" atoms). Therefore, the following discussion of the metal-semiconductor interface is restricted to n-type materials.

2.3.3 The Metal-Semiconductor Interface

Figure 2.8a shows band diagrams for an isolated metal and an n-type semiconductor. ϕ_M and ϕ_s are the work functions of the metal and semiconductor, respectively. The semiconductor is also characterized by its electron affinity, χ. The electron affinity is the energy required to bring an electron from the top of the conduction band to the vacuum level. Figure 2.8b shows the band diagram when the metal and semiconductor are brought to contact. Before contact, $E_{F_s} > E_{F_M}$. Thermodynamic equilibrium requires that, after contact, the Fermi level be constant throughout the system. To equilibrate the Fermi level, electrons must be transferred into the metal to raise E_{F_M}. This depletes the semiconductor of electrons in a region near the interface. The semiconductor is "less n-type" in this region, and the conduction and valence bands bend upward as shown in Fig. 2.8b. An electron at the Fermi level of the metal must surmount the potential barrier $q(\phi_M - \chi)$ in order to reach the conduction band of the semiconductor. This type of transport mechanism is called Schottky emission.

If metal contacts are placed on either side of a semiconductor and a voltage applied, the electric field E causes the bands in the semiconductor to slope, as shown in Fig. 2.9b. If the field is sufficient, the barrier is thinned and electrons from the negative electrode will

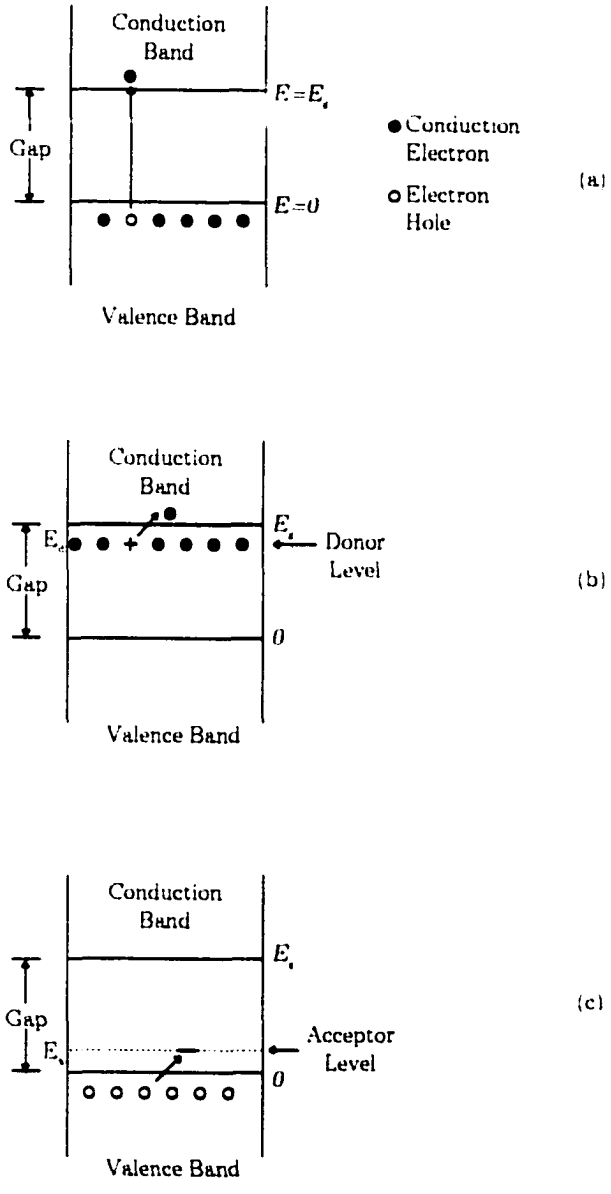

Figure 2.7: Energy bands for (a) intrinsic, (b) n-type, and (c) p-type semiconductors.

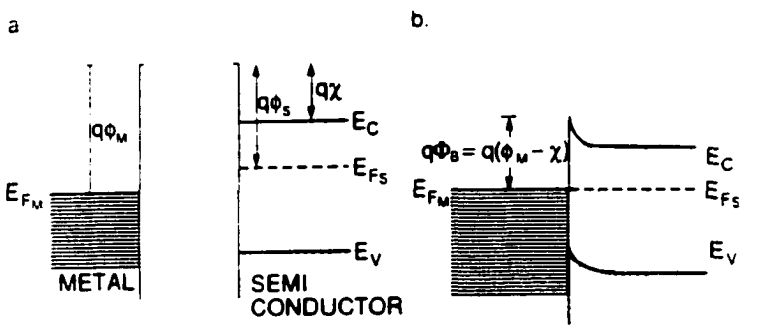

Figure 2.8: (a) Isolated metal band diagram (work function ϕ_M and Fermi level E_{F_M}) and semiconductor (work function ϕ_s and Fermi level E_{F_s}. (b) Schottky barrier formation at metal-semiconductor interface.

tunnel to the vacant conduction band states of the semiconductor, rather than surmount the barrier as in Schottky emission. This process is shown in Fig. 2.9b.

2.3.4 Electrical Transport Through Insulators

As stated, the difference between semiconductors and insulators is the energy gap between the conduction band and the valence band, E_g. The anomalous emitter structure often shows insulating properties, but the insulator is assumed to be amorphous and impure, and takes on semiconductor-like properties. There are several mechanisms by which electrons can move through an insulator after having been injected into the conduction band. These are:

- Space-Charge-Limited (SCL) Conduction. This type of conduction occurs when the rate at which charge carriers are being injected into the insulator exceeds the rate at which the carriers can move through the insulator. Further charge injection is discouraged by the formation of a charge cloud. SLC Conduction is shown in Fig. 2.10a.

- Ionic Conduction. This conduction mechanism is based on ionic rather than electronic motion. Ions have very low mobility, and require high (1-3 eV) energies to make diffusive jumps through the lattice. This mechanism is shown in Fig. 2.10b.

- Intrinsic Conduction. Negligible at room temperature for large band-gap insulators (several eV), this mechanism involves a direct electronic excitation from the valence band to the conduction band.

- Poole-Frenkel Emission. An internal emission process whereby bulk charges trapped by impurity levels in the band gap are transferred to the conduction band. Impurity states are created by structural imperfection in the lattice that lead to allowable states within the band gap. Electrons are "trapped" in the defect center, and the center in neutralized. With the application of a high field, the potential wells are distorted, as shown in Fig. 2.10c. The electrons can be thermally activated to escape the well and

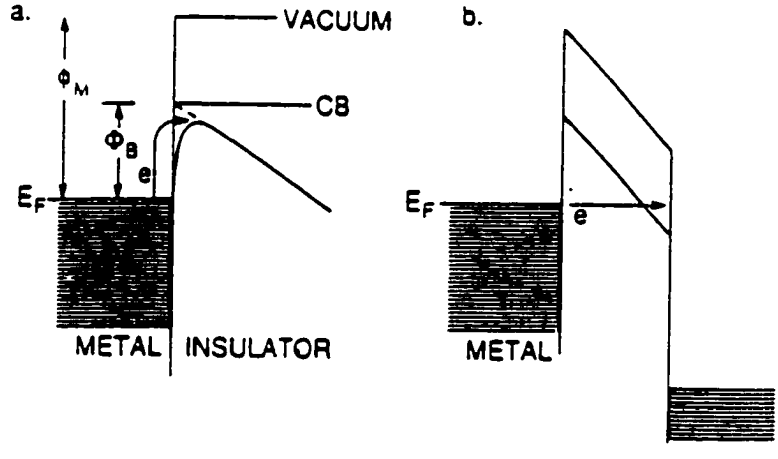

Figure 2.9: Barrier limited conduction mechanisms in a metal-semiconductor interface. (a) Schottky emission, (b) tunneling. From Ohring [37, page 166]

jump to the next trap. The equation for Poole-Frenkel emission is

$$J_{PF} = cE \exp\left(\frac{E_i}{kT}\right) \exp\left[\frac{1}{kT}\left(\frac{q^3 E}{\pi \epsilon_i}\right)^{1/2}\right] \tag{2.4}$$

where c is a constant, E_i is the depth of the trap, and ϵ_i is the insulator dielectric constant.

2.3.5 The Semiconductor-Vacuum Interface

Attention is now turned to the structure of the semiconductor surface . Gomer [10, pages 21-29] considers the potentials surface barrier presented to conduction electrons in a semiconductor, and the treatment is followed closely in this section.

At the surface of a semiconductor, the ions have dangling bonds because they are in the top layer of the material. Hence, the lattice is distorted at the surface, leading to an asymmetrical charge distribution [38]. In particular, the periodicity of the lattice is lost, and when Schrödinger's equation is solved one finds solutions that are confined to the surface. This gives rise to the surface "states". These waves exist only in the forbidden band of the solid. Surface imperfections and impurities also contribute to the density of surface states. Figure 2.11 is a band diagram for an n-type semiconductor, shown with surface acceptor states, E_s. Valence band electrons fill these trap states, resulting in a negatively charged, subsurface layer. Electrons in the conduction band of the semiconductor are repelled by the charged layer, and must do work to overcome it. This potential can be considered analogous to the work function of a metal. If there are no surface states, an applied electric field penetrates the semiconductor. The bands slope, and electrons tunnel through the Schottky barrier into the conduction band of the semiconductor. If the density of surface states is sufficient, the charge will concentrate there, and the field will not penetrate [10]. The tunneling of electrons through the Schottky barrier will be reduced. The surface band structure will become important as the development of the insulator-based field emission model.

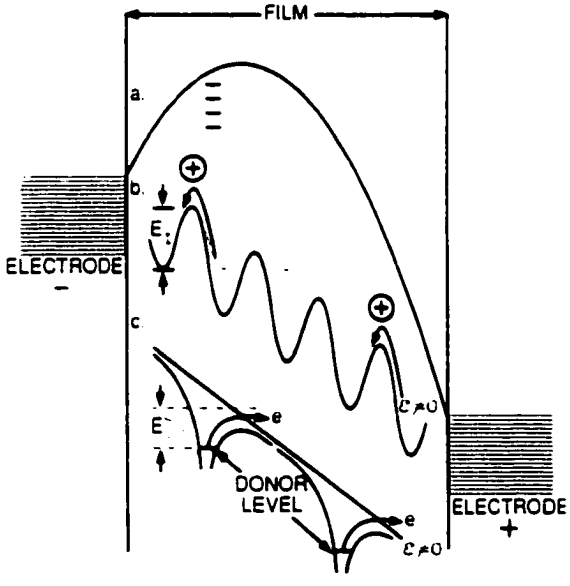

Figure 2.10: Bulk limited conduction mechanisms. (a) Space-charge-limited conduction. (b) Ionic conduction of cations, (c) Poole-Frenkel emission from trap states. E_i is the well depth. From Ohring [37, page 467].

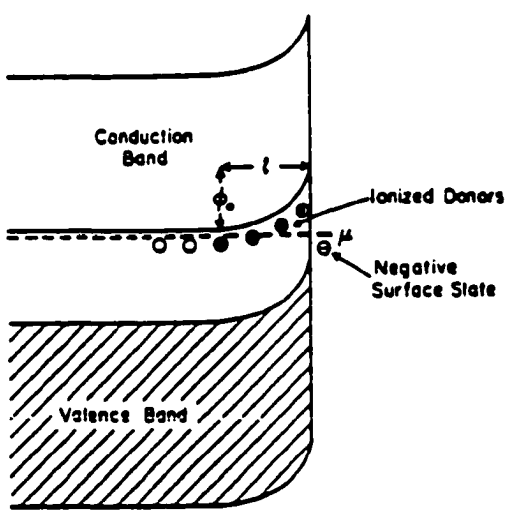

Figure 2.11: Band structure effects of the surface charge and depletion region in an n-type semiconductor. From Gomer [10, page 24].

2.3.6 Metal-Insulator-Vacuum Model

The findings of Latham and co-workers have led to non-metallic emission models. The Metal-Insulator-Vacuum (MIV) model is shown in Fig. 2.12. An insulating particle or inclusion is built into the surface of the metal. This could be a foreign inclusion or perhaps a portion of the native oxide layer. The model assumes the insulating emission site contains a high number of trap states and donor states (e.g. impurities, defects), on the order of $\sim 10^{24}/m^3$. A blocking contact (Schottky Barrier) will exist at the metal-insulator interface if $\phi_m > \phi_I$ where ϕ_m and ϕ_I are the work functions of the metal and insulator, respectively. The entire process proposed by Latham is shown in Fig. 2.13. With the application of an electric field, any mobile charge carriers in the insulator move toward the insulator-vacuum (IV) interface (Fig. 2.13b). At medium fields (Fig. 2.13c), electrons are injected into the conduction band of the insulator, and trap states on the surface are filled (to this point, no ejection of electrons into the vacuum has occurred). Due to the increased space charge in the insulator, the bands are flattened (Fig. 2.13d). The injection and movement of charge in the insulator stop.

As the field is increased, the bands are sloped further. The IV barrier is sufficiently thinned to allow tunneling through the Schottky barrier and into the conduction band of the insulator(Fig. 2.13e). Since bulk trap states are filled, electrons do not lose energy as they move through the conduction band (no Poole-Frenkel emission). The electrons are accelerated by the applied field (Latham assumes the concentration of surface states is low enough to allow field penetration), and a burst of "hot" electrons is emitted into the vacuum.

A steady state is quickly developed. Hot electrons ($E \gg k_B T$) generated near the surface (at the surface states) reduce the insulator-vacuum potential barrier. The external field will penetrate further into the surface of the insulator, increasing the tunneling probability. As the electrons near the surface state barrier are preferentially emitted, the surface field will be increased (better penetration by the field). Holes in the insulator (created near

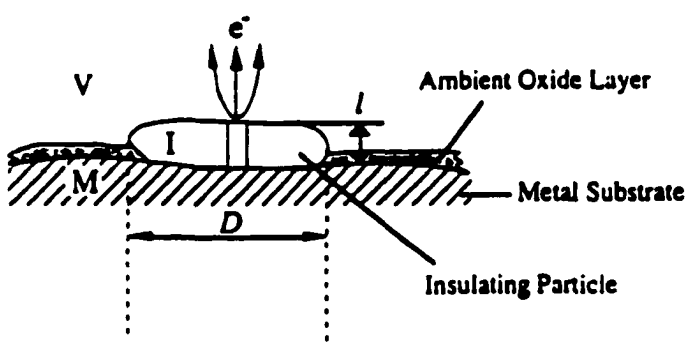

Figure 2.12: Illustration of the Metal-Insulator-Vacuum structures on extended area cathodes.

the IV interface) move back toward the MI interface, lowering the metal insulator barrier further. This process continues until the a highly conducting state is reached, and the emission has reached a "turn-on" state (Fig. 2.13f).

2.3.7 Metal-Insulator-Metal Model

The Metal-Insulator-Metal model [9] assumes a metallic flake-like particle on cathode surface, as shown in Fig. 2.12b. The flake will tend to orient itself with the electric field lines, hence acting as an "antenna" and enhancing the field strength in the insulating native oxide layer of the cathode surface. Electrons are then injected into the insulating layer by the same process as in the MIV model, gaining energy through the conduction band of the oxide layer from the enhanced electric field. A more detailed diagram of the conditions for MIM emission is shown in Fig. 2.14.

2.4 Summary

This section was intended to present the current state of understanding (and speculation) of enhanced emission from broad-area electrodes. The proposed models are based on experimental evidence that electron emission from extended area electrodes is not solely metallic in nature. Direct SEM imaging, Auger analysis of enhanced emission sites, and energy distribution measurements of the emitted electrons, indicate that the anomalous field emission from extended area electrodes is driven by non-metallic surface abnormalities. The pure Microprotrusion Model has been largely dismissed due to these findings. However, one cannot ignore the empirical observation that lower levels of emission are usually obtained from a smoother electrode surface [3]. If the mechanism of pure field emission from a sharp protrusion is to be assumed, it must be modified somehow to account for the unrealistic geometries deduced from the Fowler-Nordheim equation.

The oxide layers and foreign insulating inclusions that are found are assumed to contain lattice imperfections and impurities. The lattice imperfections in the insulating

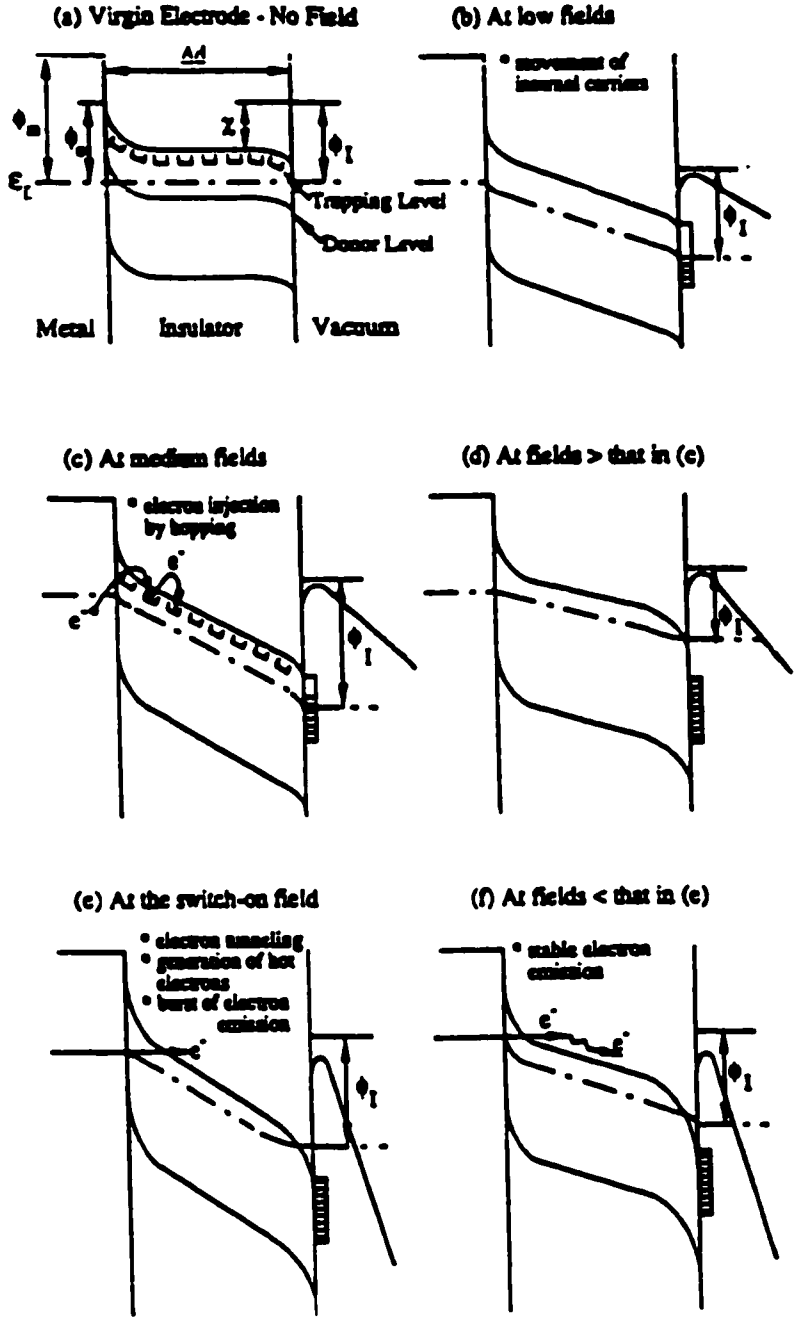

Figure 2.13: Energy band diagram for Latham's Metal-Insulator-Vacuum model [1].

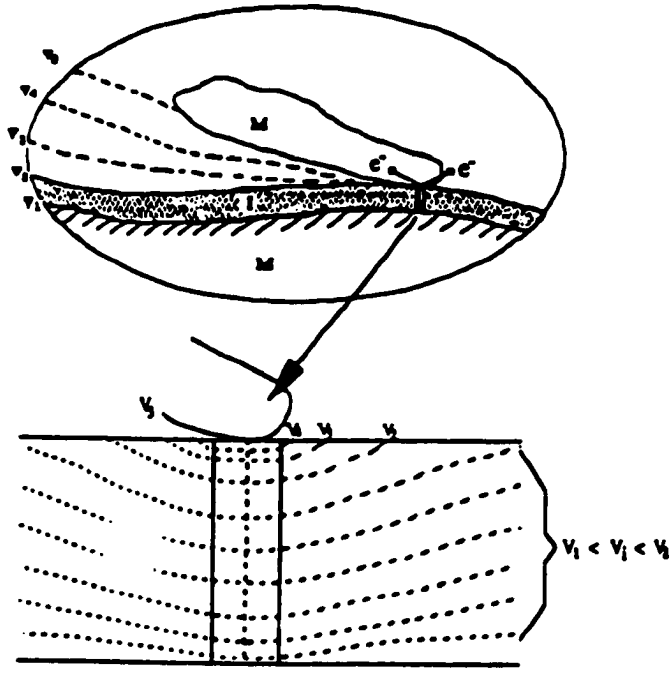

Figure 2.14: (a) An illustration describing how electrons can be scattered into the vacuum from the "antenna" effect of a metal flake on the electrode surface. (b) A diagram of the equipotential lines within the insulating layer, showing the field enhancement from the metal particulate. From Latham [1].

materials act as traps for electrical charge [39]. The insulating "particle" in Latham's insulator-based models assumes trapping levels on the order of $10^{24}/m^3$. It also assumes donor atom densities of $\sim 10^{24}/m^3$. Alteration of these factors by ion implantation, either in the oxide layer or individual localized chemical impurities in the surface, is the goal of this thesis work.

Chapter 3

Plasma Source Ion Implantation

3.1 System Description

In the course of this thesis, a 100 kV PSII system was designed and developed at William and Mary for processing large area work pieces. A schematic of the W&M PSII is shown in Fig. 3.1. The implanter has three critical components: the vacuum system, the pulse forming network (PFN) and the plasma generation system.

The vacuum system has a base pressure of 10^{-9} Torr. Operation of the plasma during the implantation requires a stable operational pressure of 0.5 mTorr. Mass flow controllers are used to introduce source gases. A 150 l/s turbo molecular pump is used for pumping the implant species from the chamber.

The PFN delivers a high voltage (up to 10 kV) pulse train at a maximum repetition rate of 40 Hz. Maximum current at 10 kV is 300 Amps. The pulse is delivered through a 10:1 step up transformer to achieve a peak voltage of 100 kV and a peak current of 30 A (for convenience, the combination of the pulse forming network and the transformer will be referred to as the PFN). The square pulse is 10 μs long with $< 1\mu$s rise time, $<10\%$ ripple, and fall times on the order of a few μs. For repairs and maintenance, the energy stored in the PFN capacitors is automatically shunted to ground in a fail-safe mode. All high voltage components are shielded from contact.

Plasma generation is accomplished by a *sustained diode* scheme. A hot tungsten

filament is used to emit electrons thermionically into the chamber. The filament (the cathode) is biased negatively to $-50V$. A small plate (the anode) placed adjacent to the filament is biased positively 50 V to collect the electrons. The gas is partially ionized and a *plasma* is ignited. The plasma generation circuit is shown in Fig. 3.1.

Once the discharge is initiated and stable, high voltage pulses are applied to the workpiece by the PFN. The dynamics of the plasma during the application of the high voltage pulse train will be addressed in the next section.

3.2 Plasma Dynamics

A plasma is an assembly of charged particles whose collective motion is dominated by electromagnetic forces. Neutral gas atoms may also be present, and may contribute to the behavior of the plasma. Plasmas that are used in material processing are about 1 - 5% ionized. The plasma electrons, ions, and neutrals, are described by their temperatures, $T_e \gg T_i \approx T_g$. The subscripts e, i, and g refer to the electrons, ions, and neutrals, respectively.

The plasma *sheath* is a positively charged thin layer adjacent to all surfaces in contact with the plasma. The sheath develops due to the differences in the relative thermal velocities of electrons ($V_{th_e} = \sqrt{T_e/m_e}$), and the ions ($V_{th_i} = \sqrt{T_i/m_i}$). The temperatures T_e and T_i are given in units of electrons volts (eV), and obey a Maxwellian distribution. In a *quasi-neutral* plasma, where the potential, Φ, and the electric field, E, are zero, electrons would be quickly lost to the walls due to their relatively higher temperature and lower mass. Indeed, the electrons have velocities that are on the order of 100 times greater than that of the ions. As a result, a situation shown in Fig. 3.2 occurs. Electrons near the walls (normally ground) are quickly lost due to their higher velocity. What remains is a thin, positively charged region of ions ($n_e \ll n_i$). The potential profile that develops is shown in Fig. 3.3. The electric field across the sheath is directed outward toward the walls. This field forces electrons into the plasma and ions out of the plasma. The plasma potential comes to equilibrium such that the net charge gain (creation of charged species) from the power

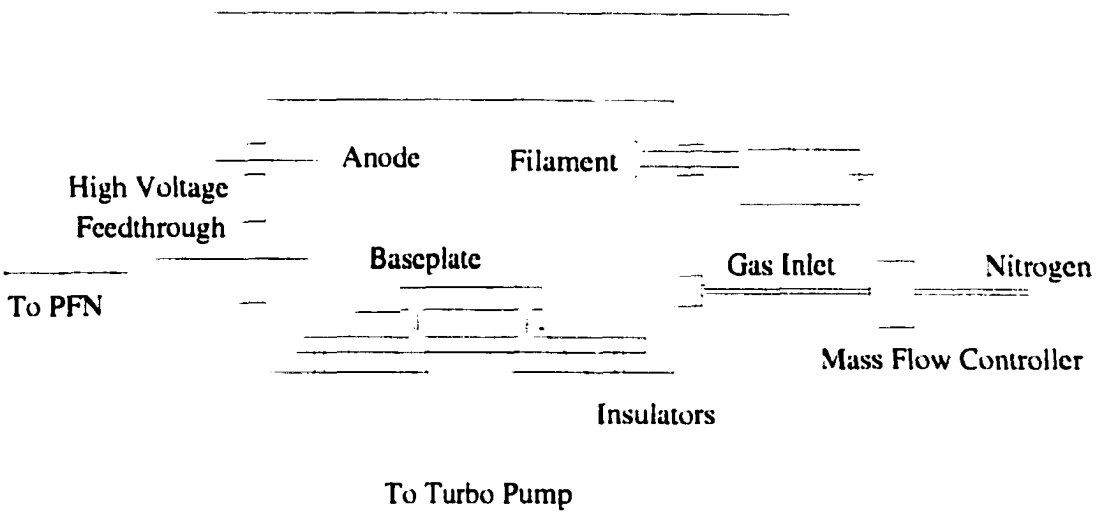

Figure 3.1: William and Mary Plasma Source Ion Implantation apparatus

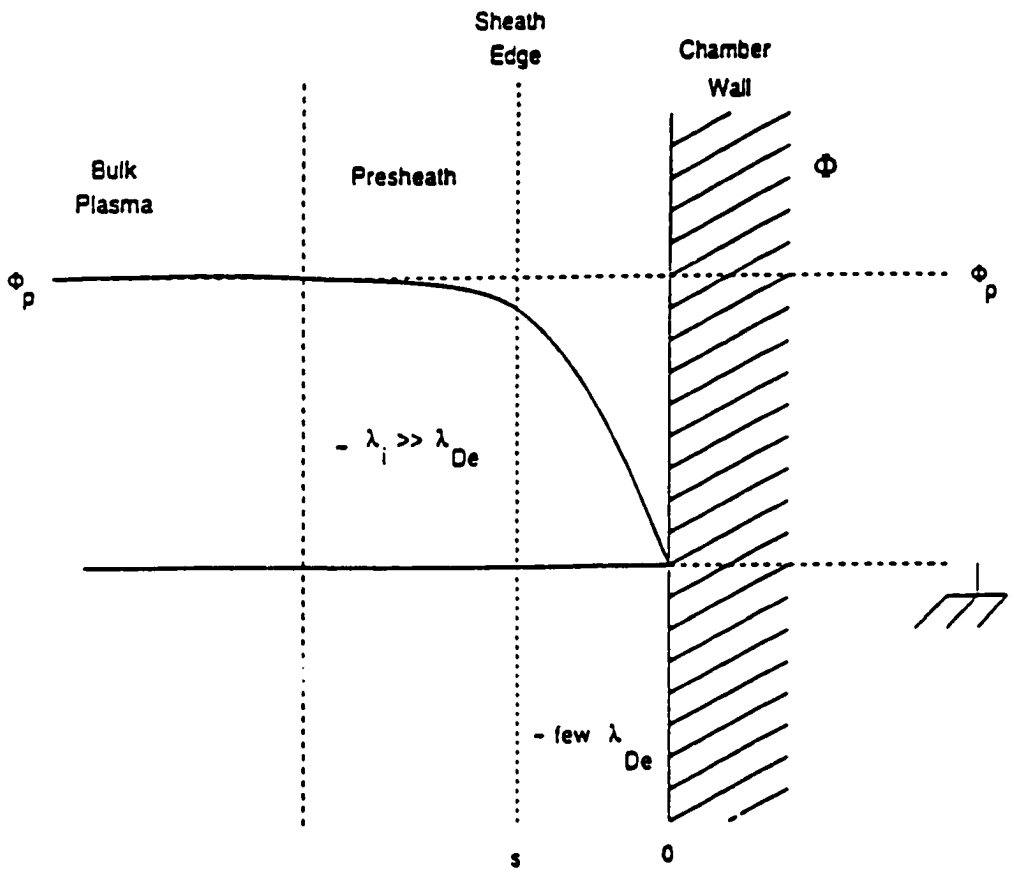

Figure 3.2: Generalized sheath formation. A positively charged layer forms near the surface of the chamber walls. A potential barrier is formed that prevents further electron loss to the wall. Ions traverse the sheath with kinetic energy $\sim eV_p$.

input is balanced with the net charge loss. The electric field does not terminate abruptly at the sheath boundary, but rather extends slightly into the plasma. This region outside the sheath is called the *pre-sheath*, and ions traversing the pre-sheath gain energy through a potential drop of $\approx T_e/2$. The ions are accelerated to a speed of $u_B = \sqrt{eT_e/M}$ (the Bohm sound speed) [40]. The electron density near the sheath edge follows a Maxwell-Boltzmann distribution $n_e(x) = n_{es}e^{\Phi(x)/T_e}$, where n_{es} is the density of electrons at the sheath edge. For convenience, $\Phi(x)$ is taken to be zero at the sheath edge.

When a metal boundary in a plasma is suddenly subjected to a high negative potential ($\Phi \ll T_e$), the electrons near the boundary are expelled ($n_e \rightarrow 0$). What remains is an ion-rich region, the so-called *ion matrix sheath*. If the assumption is made that the ion density is uniform, the thickness of the ion matrix sheath of density n_s can be found by applying Poisson's equation:

$$\begin{aligned} \frac{dE}{dx} &= \frac{en_s}{\epsilon_o} \\ E &= \frac{en_s}{\epsilon_o}x \end{aligned} \tag{3.1}$$

$$\begin{aligned} \frac{d\Phi}{dx} &= -E \\ \Phi &= \frac{-en_s}{\epsilon_o}\frac{x^2}{2} \end{aligned} \tag{3.2}$$

With $\Phi = -V_o$, the thickness of the matrix sheath can be obtained:

$$s = \sqrt{\frac{2\epsilon_o V_o}{en_s}}. \tag{3.3}$$

Defining the *Debye length* as $\lambda_D = \sqrt{\epsilon_o T_e/en_s}$, the matrix sheath thickness s can be written as

$$s = \lambda_D\sqrt{\frac{2V_o}{T_e}}. \tag{3.4}$$

The Debye length is a characteristic parameter used to describe the shielding effects of the sheath. For the quasi-neutrality condition to hold true, the number of charged particles in a sphere of radius λ_D is required to be much greater than one. Or, the Debye length must

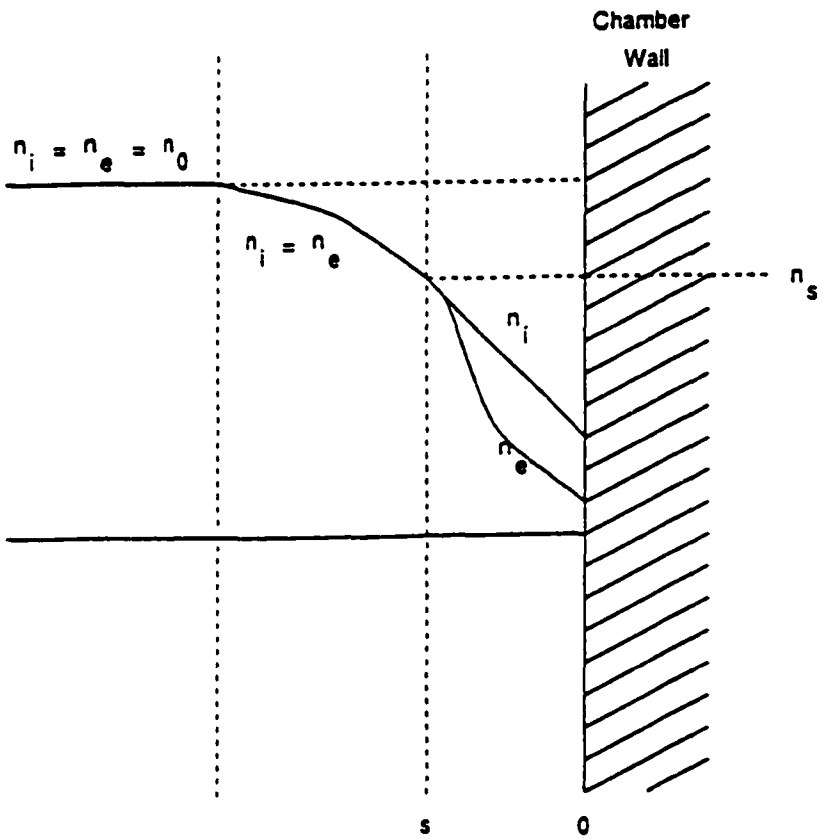

Figure 3.3: Generalized sheath density profile. In the bulk, the plasma is still quasi-neutral. At λ_i (the ion mean free path) from the wall, the plasma density begins to fall from the bulk value (presheath), but the quasi-neutrality condition still holds. In the sheath, the ion density becomes greater than the electron density.

be much less than the chamber dimensions, L. The Debye length for laboratory plasmas is on the order of microns to millimeters.

With the application of an instantaneous negative voltage to a metal boundary in a plasma, the sheath begins to expand from the steady state Child-Langmuir sheath. Lieberman [41] considers the evolution of the plasma after the application of a high, negative voltage V_c at $t = 0$. In Fig. 3.1, n_o is the plasma density, s_o is the ion matrix sheath thickness, and $\omega_{pi} = \sqrt{e^2 n_o/\epsilon M}$ is the ion plasma frequency. Lieberman derives a time-dependent expression for the sheath expansion, and this derivation is presented below.

First, A few assumptions can be made:

- The ions, due to their relatively larger mass, are stationary for all time t.
- Electrons are inertia-less.
- The charge voltage V_o is much greater than T_e, so λ_D is much less than s_o.
- A quasi-static sheath forms before and after the voltage pulse.
- The electric field remains unchanged during the ion motion across the sheath, i.e. the sheath expansion is small.

The Child-Langmuir law for current density J_c for a voltage V_o crossing a sheath s is [42]

$$J_c = \frac{4}{9}\epsilon_o \sqrt{\frac{2e}{M}} \frac{V_o^{3/2}}{s^2} \tag{3.5}$$

where ϵ_o is the permittivity of free space, e is the electron charge, and M is the mass of the ion. As the ions in the matrix sheath begin to accelerate toward the workpiece, the ion density in the sheath begins to decrease. The ability of the positive sheath to shield the workpiece from the plasma is compromised. The sheath must expand in order for the plasma to maintain the quasi-neutrality condition. The net charge crossing the expanding sheath boundary is

$$J_c = en_o \left(\frac{ds}{dt} + u_B \right). \tag{3.6}$$

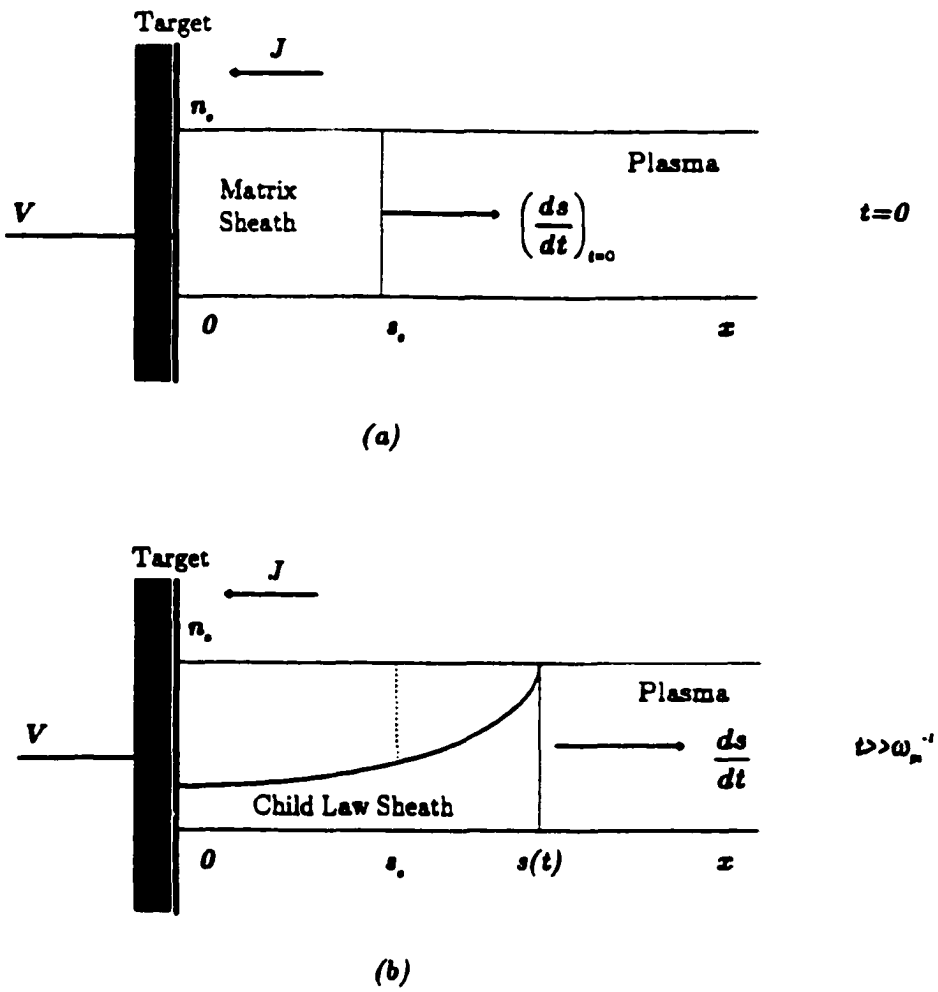

Figure 3.4: Expansion of the ion-matrix sheath. At $t = 0$, electrons are expelled away from the workpiece to a distance s_o, revealing the ions.

The first term in the equation accounts for the moving sheath uncovering more ions. The second term accounts for the acceleration of the ions to the sheath edge. Setting Eq. 3.5 equal to Eq. 3.6, one can solve for the sheath velocity ds/dt:

$$\frac{ds}{dt} = \frac{2}{9}\frac{s_o^2 u_o}{s^2} - u_B \tag{3.7}$$

where $s_o = \sqrt{2\epsilon_o V_o/en_o}$ is the initial matrix sheath thickness, and $u_o = \sqrt{2eV_o/M}$ is the characteristic ion velocity. Integrating this equation yields

$$\tanh^{-1}\left(\frac{s}{s_{CL}}\right) - \frac{s}{s_{CL}} = \frac{u_B t}{s_{CL}} + \tanh^{-1}\left(\frac{s_o}{s_{CL}}\right) - \frac{s_o}{s_{CL}}. \tag{3.8}$$

Where s_{CL} is the thickness of the Child-Langmuir sheath, s_o is the initial ion matrix sheath thickness, and s is the time-dependent position of the ion matrix sheath. This equation can be used to calculate the distance the expanding ion matrix sheath travels during the time the pulse is on. The final sheath thickness is critical. If the sheath expands too far, an arc may form between the workpiece and the chamber walls. Also, the pressure must be low enough to ensure the mean free path of the ions is greater than the final sheath thickness. Otherwise, ions will lose energy through collisions with the background gas. In the limit of small sheath expansion, that is, when the pulse ends long before the steady state Child-law sheath, s_{CL}, has formed, $s \ll s_{CL}$. Assuming $s_o \gg s_{CL}$, the position of the sheath edge as a function of time can be found by expanding eqn. 3.8 and obtaining

$$s = s_o[(2/3)\omega_{pi}t + 1]^{1/3}. \tag{3.9}$$

For pulse widths on the order of $10\mu s$, and plasma densities on the order of $10^10/cm^3$, one obtains the plot of sheath position as a function of time shown in Fig. 3.5. The sheath expands from the initial ion matrix sheath thickness to approximately 8 cm from the workpiece. The steady state Child-law sheath for a 30 kV pulse would be approximately 20 cm. The pulse is shut off long before the steady state Child-law sheath forms. The mean free path can be estimated by the crude approximation

$$\lambda_{mfp} = 5 \times 10^{-3}/P \tag{3.10}$$

with λ_{mfp} given in units of centimeters, and P in Torr. At P = 5×10^{-4} Torr, λ_{mfp} = 10 centimeters. The ion matrix sheath, during the 10 μs pulse, can be considered collisionless. Some fraction of the implanted ions come from inside the ion matrix sheath, and the remainder cross the sheath boundary and gain the full implant energy, if no collisional energy loss takes place. Assuming that the charge density in the ion matrix sheath is initially uniform, the electric field varies as

$$E = \frac{en_o}{\epsilon_o}(x - s) \tag{3.11}$$

or, since $\omega_{pi} = \sqrt{e^2 n_o/\epsilon M}$,

$$E = \frac{M}{e}\omega_{pi}^2(x - s). \tag{3.12}$$

The ion motion in the electric field is $F/m = E/(Me) = d^2x/dt^2 = \omega_{pi}^2(x - s)$. The distance the ion matrix sheath edge propagates can be approximated by $s = s_o + (ds/dt)_o t$. From eqn. 3.7, one can now write

$$\frac{d^2x}{dt^2} = \omega_{pi}^2(x - s_o) - \frac{2}{9}u_o\omega_{pi}^2 t. \tag{3.13}$$

The above equation can be integrated to obtain

$$x - s_o = (x_o - s_o)\cosh(\omega_{pi}t) - \frac{2}{9}s_o\sinh(\omega_{pi}t) + \frac{2}{9}u_o t \tag{3.14}$$

with $x = x_o$ and $dx/dt = 0$, at $t = 0$. The ion flight time across the sheath can be computed by setting $x = 0$ in the above equation and obtaining

$$s_o = (x_o - s_o)\cosh(\omega_{pi}t) - \frac{2}{9}s_o\sinh(\omega_{pi}t) + \frac{2}{9}u_o t. \tag{3.15}$$

Ions that traverse the entire sheath travel a distance x_o, therefore

$$s_o|_{x=x_o} = \frac{2}{9}\sinh(\omega_{pi}t) - \frac{2}{9}u_o t. \tag{3.16}$$

The above equation can be solved for a normalized time $\hat{t} \cong \omega_{pi}t \cong 2.7$. After t, all matrix sheath ions have implanted. The ions from the matrix sheath arrive at the surface with

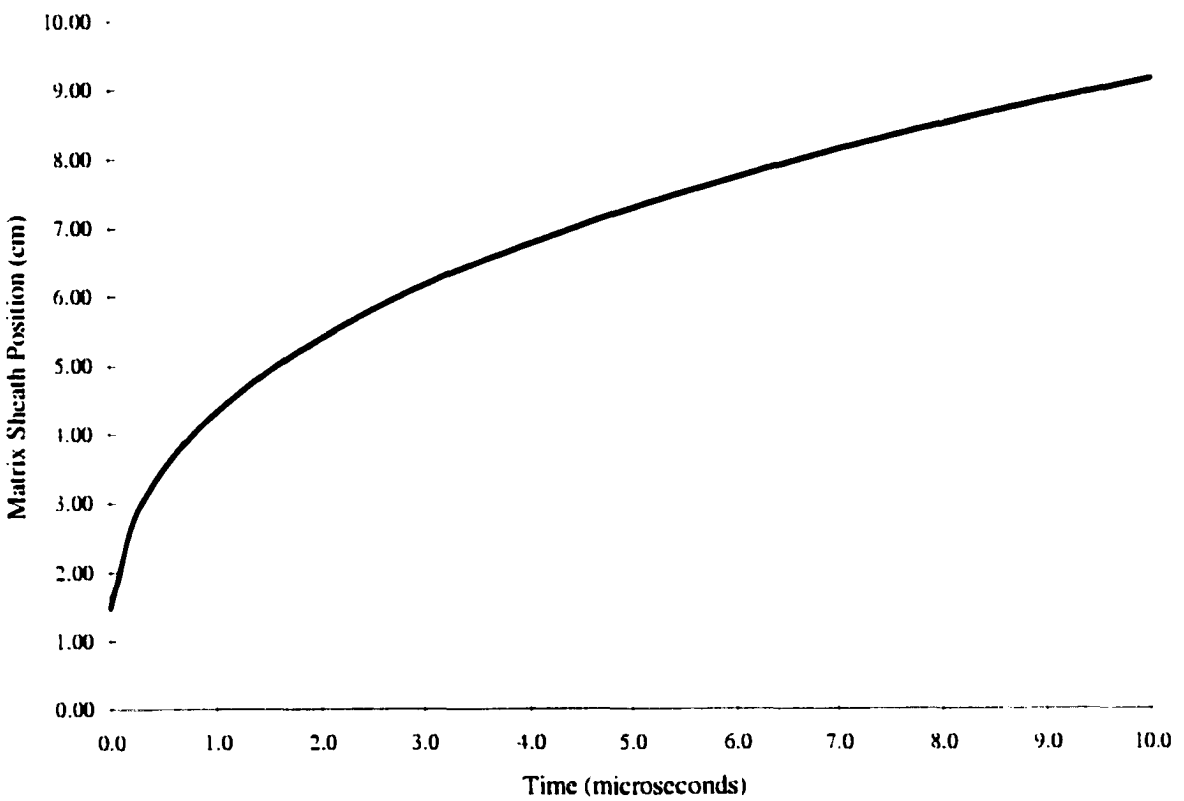

Figure 3.5: Sheath position as a function of time after instantaneous 30 kV voltage pulse. Plasma density is $10^10/cm^3$.

an energy distribution $E < qV_c$. Since ω_{pi} is proportional to $\sqrt{n_o}$, higher density plasmas will result in a low t. A larger percentage of the impacting ions will be those that crossed the matrix sheath and gained the full implant energy. The plasma density in the W&M PSII was measured to be about $10^9/cm^3$, so $\omega_{pi} \approx 1$ MHz. The matrix sheath ions, then, are implanted after about a microsecond. The remainder of the ions have gained the full energy, assuming a collisionless sheath. The W&M PSII pulse width is 10 μsec, so it is expected that a majority of the ions reach the surface with the full implant energy.

Scheuer et al [42] make the assumption that the ions outside the matrix sheath have zero velocity when the sheath edge reaches them ($u_B = 0$). Again, equating the Child-Langmuir law, eqn. 3.5, equal to the net charge arriving at the target, eqn. 3.6, with the assumption of zero initial velocity, one can solve for the sheath velocity:

$$\frac{ds}{dt} = \frac{4}{\epsilon_o} 9n \sqrt{\frac{2}{eM}} \frac{V^{3/2}}{s^2} \tag{3.17}$$

Integrating this equation, one obtains the solution for sheath position as a function of time:

$$s = s_o[(2/3)\omega_{pi}t + 1]^{1/3}. \tag{3.18}$$

This is the same solution found by Lieberman with the assumption of small sheath expansion, $s \ll s_{CL}$.

The temporal expansion of the ion matrix sheath edge has been calculated numerically [43], analytically [42], and measured experimentally with Langmuir probes [44]. Results from Malik *et al* [45] are shown in Fig. 3.6. The sheath edge as a function of time is shown for several target biases. Experimental measurements compare well with theory.

3.3 PSII Operation

3.3.1 Pulse Forming Network

The pulse forming network was constructed by North Star Corporation in Albuquerque, NM to the required specifications. It was integrated into the PSII system to be

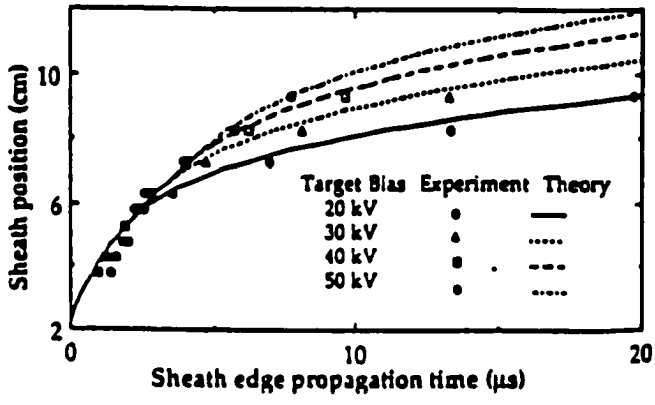

Figure 3.6: Comparison of experimental measurements of sheath position and the analytical solution for sheath propagation. From Malik [45].

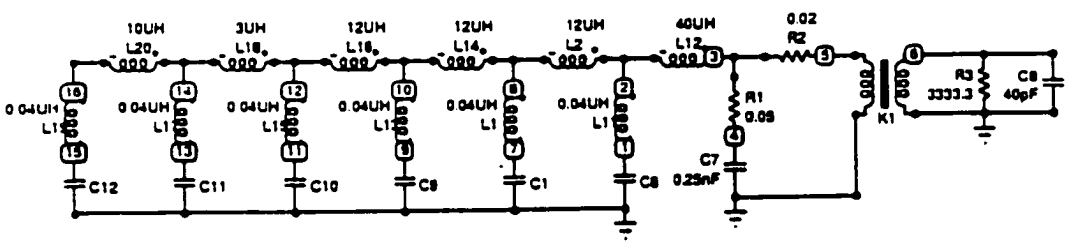

Figure 3.7: Schematic of W & M PSII Pulse Forming Network and step-up transformer

safe and easy to operate. The schematic of the PFN is shown in Fig. 3.7. The PFN forms a square pulse as follows: (1) the capacitor bank is charged by the high voltage power supply to the required voltage, (2) the trigger unit initiates breakdown in the thyratron, which is a gas-filled tube switch, (3) the circuit is complete, and current begins to flow. At $t = 0$, current flows from the first capacitor, C6. As the voltage across C6 drops, the inductor L2 resists the current flow from the next capacitor, C1. Thus, the charge from C1 is delayed slightly. The capacitors continue to sequentially discharge in this manner until all have delivered their charge through the thyratron. The natural ring in the circuit causes a reverse voltage to appear across the thyratron. This reverse voltage terminates the current and initiates the recovery stage of the tube. The capacitors are recharged for the next pulse.

During development at North Star, the W&M PFN was matched to a $3.3k\Omega$ resistor, and tuned to deliver a square-shaped pulse. However, the plasma presents a very non-linear impedance load to the PFN. The unit was designed to be easily tuned by changing the inductor values. In order to ensure that the PFN would deliver a square-shaped pulse, the effective resistance and capacitance of the plasma during the pulse (ion matrix expansion stage) needed to be understood. The following sections address the efforts to model the PFN and plasma during the pulse.

3.3.2 Pulse Shaping

Qin *et al* [46] developed a model of an equivalent circuit of a plasma load and its effective time-dependent impedance. An equivalent circuit is shown in Fig. 3.8. The factor G_2 is defined as a constant conductance presented to the PFN by the plasma. The functions $G_1(t)$ and $C(t)$ are the time varying conductance and capacitance of the system.

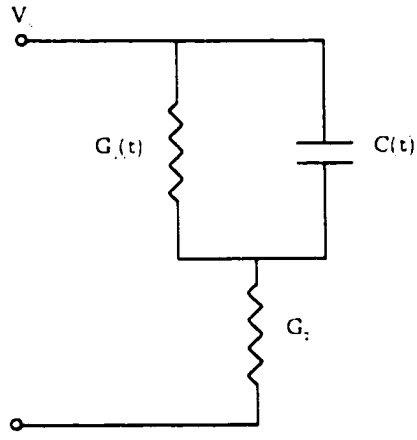

Figure 3.8: From Qin *et al* [46]. The equivalent circuit of a plasma during a high voltage pulse

.

respectively. The analytical functions derived by Qin for the impedance are

$$\begin{aligned} C(t) &= \frac{\epsilon_o}{s(t)} \\ G_1(t) &= \frac{4}{9}\frac{\epsilon_o}{s(t)}\left[\left(\frac{2}{3}\omega_{pi}t+1\right)^{-1/3}+\frac{3}{2}\left(\frac{2}{3}\omega_{pi}t+1\right)^{-1}\right] \\ G_2 &= \frac{2}{9}\frac{en_iu_o}{V}. \end{aligned} \tag{3.19}$$

The functions are given in units of $\Omega^{-1}m^{-2}$. The effective impedance should consider γ_i, the secondary electron emission coefficient, the target area, i.e. $G = G \cdot A(\gamma_i + 1)$ and $C = C \cdot A(\gamma_i + 1)$.

These functions were used as dynamic capacitance and resistance ($1/G$) values in a commercial circuit simulation software package, Micro-Cap V. The PFN could be modeled with the software, and the pulse shape altered by simply changing the inductor values in the program. Figure 3.9 shows the simulated waveform.

Figure 3.10 shows a representative pulse (this particular pulse is only 25 kV peak) from the tuned PFN with the plasma as load. The pulse trace shows only a small reflected pulse. Severe mismatch would result in reflected energy and a second pulse. Reflected pulses result in low energy ions with insufficient energy to implant past the first few monolayers, but sufficient energy to sputter target material ($E_i < 10keV$).

3.3.3 Profile and Dose Predictions

The net dose (cm^{-2}) of nitrogen can be determined by the following equation [47]:

$$d = \frac{twfnI}{qA(1+\gamma_i)} \tag{3.20}$$

where d is the expected dose, t is the total process time, w is the pulse width, f is the pulse frequency, n is the average number of atoms per ion, I is the average current per pulse, q is the fundamental charge, A is the target area (456 cm^2), and γ_i is the secondary electron emission coefficient. Of the nine parameters involved, the two that are the most uncertain

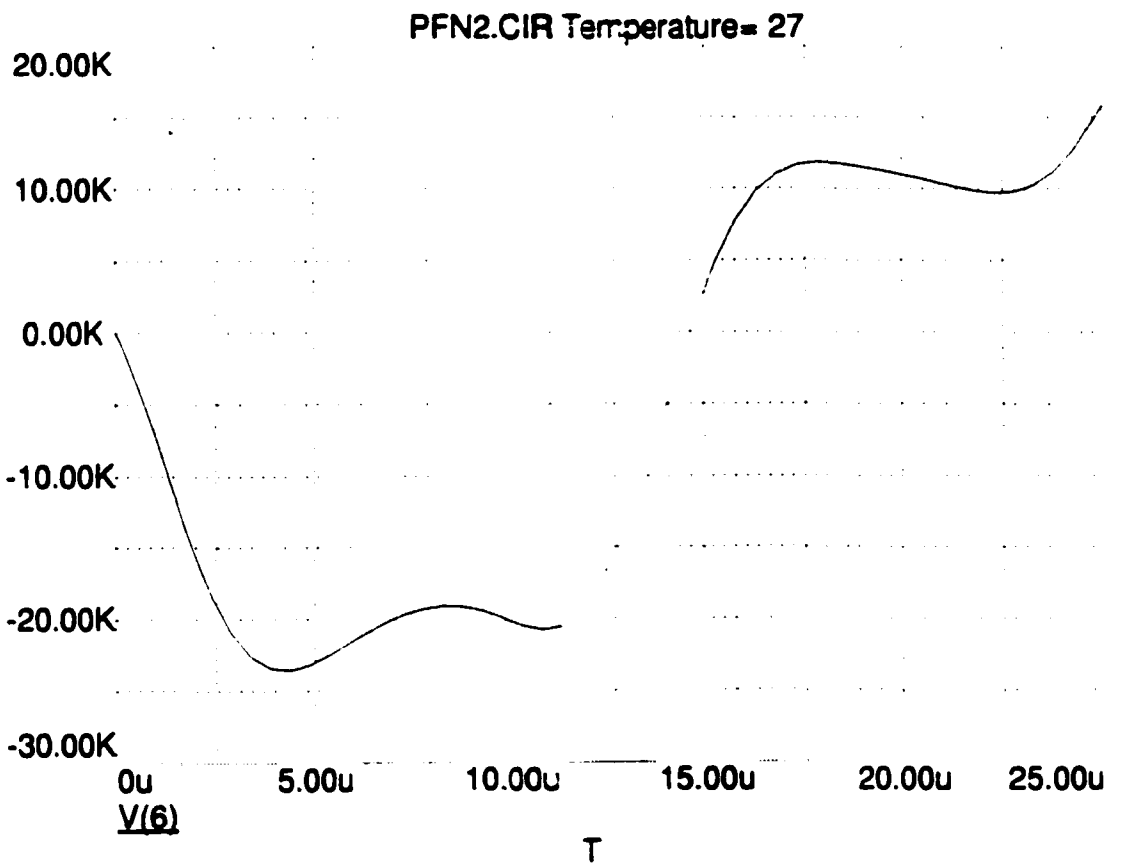

Figure 3.9: Waveform from the MicroCap V circuit simulation program. $n_i = 10^9/cm^3$.

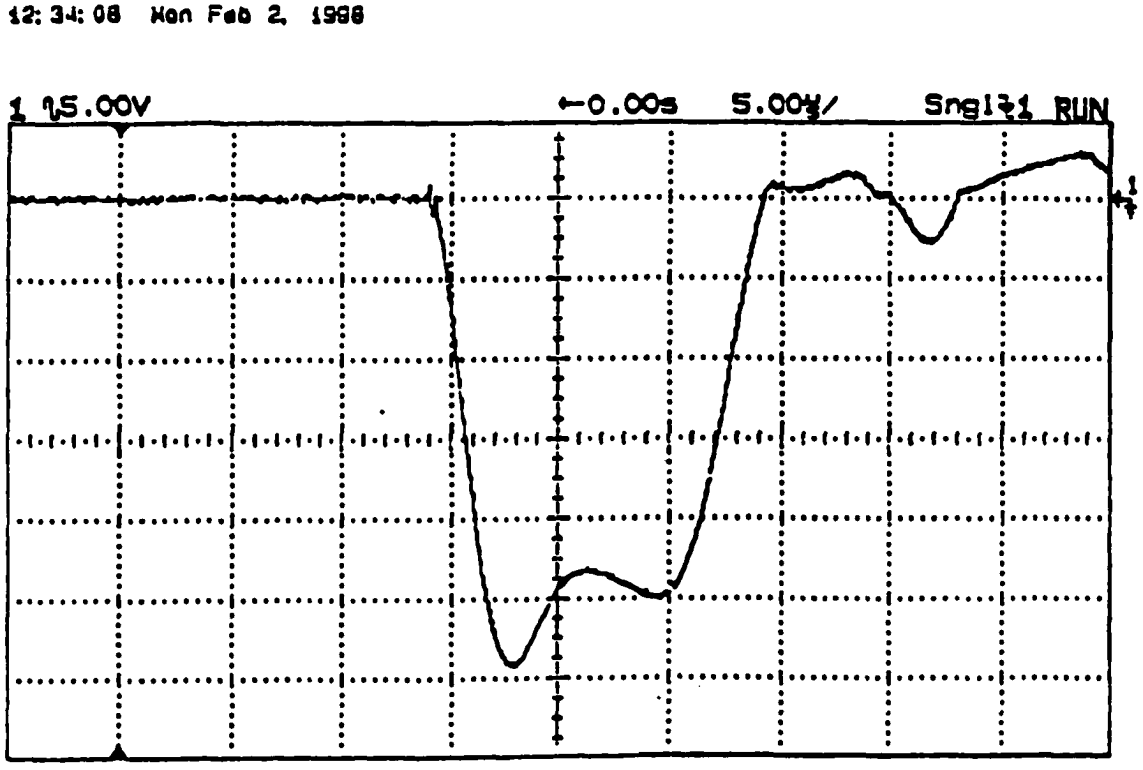

Figure 3.10: 30 kV pulse output from PFN with plasma as load.

are γ_i and n. γ_i for nitrogen into stainless steel has been measured and closely follows the form [48]:

$$\gamma_i = \gamma_{20}\sqrt{\frac{V_c}{20kV}} \tag{3.21}$$

where V_c is the charge voltage in kV, and $\gamma_{20} = 4.0$ is the experimentally measured SEEC for 20 keV N^+ ions into steel.

The dissociation fraction has been experimentally measured for filament driven nitrogen plasmas to be about 25% [49]. The factor n in eqn. 3.21 is computed to be $1(0.25) + 2(0.75) = 1.75$. The value of n has not been measured for the W & M PSII. Equation 3.20 gives approximate run times, but a direct measure of the retained dose is required through *Auger Depth Profiling.*

3.3.4 Initial Operation and Depth Profiling

Stainless steel samples were polished on a mechanical polisher to nine micron diamond paste. The samples were implanted with nitrogen at a pulse voltage of 30 kV and average current per pulse of 3.0 Amps. The process time was 2.5 hrs. at a repetition rate of 40 Hz.

The determination of acquired dose is performed with Auger sputter depth profiling. The ESCALab MKII is equipped with a sputter ion gun capable of providing a 0.5 microamps beam of 4 kV Argon ions. AES is performed in the "crater" of the ion beam at intervals to attain a percent composition. An approximate sputter yield for stainless steel was taken to be about 30 Angstroms/second. This value should only be taken as an estimate, as the sputter yield can change as a function of material composition and radiation damage. Fig. 3.11 shows the measured depth profile as a function of sputter depth for the 30 kV, 2 $\frac{1}{2}$ hr. process run. The shape of this pulse is discussed below, in terms of the ion energy distribution and the target temperature.

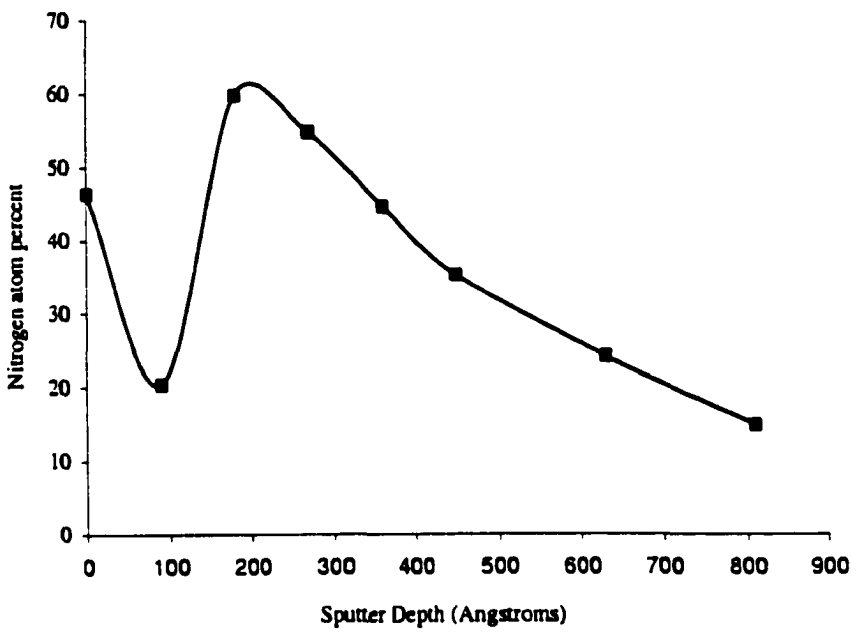

Figure 3.11: AES nitrogen percentage as a function of sputter depth.

Energy Distribution

The energy distribution of ions in a the PSII process can only be assumed. A few boundaries can be put on the distribution, however:

- The plasma is partially dissociated. The dissociation fraction (N^+/N_2^+) has been measured experimentally by Tang *et al* [49] to be about 25% for thermionic source plasmas. Some ions, therefore, will travel the extent of the sheath and gain the full impact energy of 30 kV.
- N_2^+ ions that travel the extent of the sheath will arrive with one half of the acceleration voltage, as the charge is shared between the two ions. Since two atoms come with each N_2^+ ion, and there are 3 N_2^2 ions for every N^+ ions, the energy distribution is dominated by the N_2^+ ion energy.
- Matrix sheath N^+ ions will impact with an energy distribution of range $0 < E < E_{max}$, where E_{max} is the energy an N^+ crossing the sheath boundary and gaining the full acceleration energy.
- Matrix sheath N_2^+ ions will impact with an energy distribution of range $0 < E < E_{max}/2$, where E_{max} is the energy an N^+ crossing the sheath boundary and gaining the full acceleration energy.
- Ions with energies less than a few kilovolts will not implant below the first few atomic layers, and will mainly cause sputter erosion of the surface. The surface will recede, changing the final ion distribution.

To know, exactly, the implant energy would require an energy spectrometer. Modifications could be made to the PSII to obtain a more mono-energetic distribution. The first is to *pre-dissociate* the nitrogen gas with an radio-frequency or microwave plasma generator prior to its entry into the main chamber. This would increase the N^+/N_2^+ ratio. Also, a higher plasma would result in a higher fraction of the total ion flux originating from the sheath boundary.

Diffusion

Another factor affecting the depth profile is the diffusion of the nitrogen due to the heating of the workpiece by the implant energy. The exact temperature of the workpiece during the process run is difficult to measure, as the workpiece is being pulsed to several tens of thousands of volts. This requires the use of an additional ceramic feedthrough to insulate the thermocouple leads from ground, which is very expensive. One can make an estimate on the temperature increase, however. The total energy input to the workpiece is 108 Watts. This can be found by multiplying the energy stored in the capacitors, $E = \frac{1}{2}CV^2$ times the repetition rate. The secondary electron emission coefficient for 15 kV nitrogen into steels is about 3. This would yield a net power input to the workpiece on the order of 30 Watts. The only heat sinks are the small quartz stand-offs and the high voltage feed (a 1/4" stainless steel rod) so heat loss by conduction is small. To calculate the approximate temperature of the sample during the process, the following heat equation is useful:

$$mc_p \frac{dT}{dt} = Q_{in} - Q_r \tag{3.22}$$

where m is the mass of the workpiece, c_p is the specific heat of the material, Q_{in} is the cycle averaged power input, and Q_r is the loss due to radiation. The radiative cooling Q_r is determined by

$$Q_r = \epsilon\sigma(T^4 - T_c^4) \tag{3.23}$$

where T_c is the chamber temperature, ϵ is the emissivity of the workpiece, and σ is Stephan-Boltzmann constant ($5.67 \times 10^{-8} W m^{-2} K^{-4}$). Combining these equations yields

$$mc_p \frac{dT}{dt} = Q_in - \epsilon\sigma(T^4 - T_c^4). \tag{3.24}$$

The difficulty in solving this equation is the uncertainty in the SEEC, the time-dependent temperature of the chamber during the implantation (this could be measured with a thermocouple), and the emissivity of the workpiece, which can change during the implant time. To simply estimate the temperature rise, the loss by radiation is ignored for a moment.

The value with $Q_r = 0$ is ΔT = 30 W × 9000 seconds / (20Kg × 0.44 kJ/kg/°K) = 30 °K. Thus, only a minimal increase in the time-averaged temperature can be expected from the actual implantation pulses. One may need to consider the rapid thermal spikes associated with each pulse. These have energy densities of $2.7J/10^{-5}sec/0.1m^2/3 = 0.9MW/m^2$. Other factors that will contribute to the heating of the workpiece are the plasma itself (by ion and electron bombardment between the pulses), and the 100 Watt tungsten filament used for plasma generation. The most reliable temperature determination could be made by simply calibrating an infra-red temperature probe against a thermocouple during measurements of heated stainless steel test pieces. This calibration could then be transferred to measurements of the workpiece during the implantation procedure.

3.3.5 TRIM Profiles

TRIM (TRansport of Ions in Matter) is a Monte Carlo code that predicts the distribution and energy loss of energetic ions impacting on surfaces [50]. TRIM also computes electronic excitation on the atoms, lattice damage, plasmons, and phonon production. TRIM follows a particle's "history" through the lattice. Each particle begins with a given energy, direction, and position. Binary collision processes are assumed (TRIM is reliable for $E_i > 100eV$), and the ion moves in a straight path between collisions. The energy is adjusted to account for nuclear and electronic energy losses, and the history is ended when the particle's energy drops below a specified value, or the particle exits the target material.

In Fig. 3.12, results are shown from a TRIM simulation for 30 kV N_2^+ ions (15 kV N^+) incident on a 304 stainless steel surface. Also shown is the data from a depth profile of a 30 kV implanted sample.

The low energy distribution of the matrix sheath ions is most likely the cause of the shallowness of the measured concentration. Sputtering of the top surface layer causes the profile to recede. The long tail of the measured depth profile may be due to diffusion of the nitrogen into the steel.

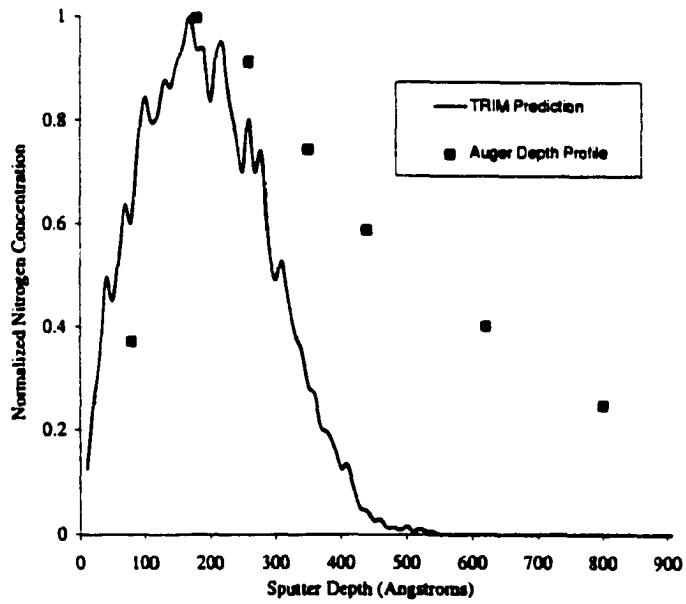

Figure 3.12: Final depth profile from a TRIM simulations for 30 kV N_2^+ ions incident on 304 stainless steel.

3.3.6 X-ray Photoelectron Spectroscopy

Implanted samples were analyzed with XPS. XPS will be described in detail in Chapter 5, but it is a method of determining the surface constituents on a sample. The sample was sputter cleaned for 30 seconds with 30 $\mu A/cm^2$ Argon ions at 5 kV to remove any contaminants on the top layer. Figure 3.13 shows the peaks associated with nitrogen. The peaks were deconvoluted to determine location. The peak at 397.2 eV is associated with interstitial N_2. The peak at 403.8 eV is due to precipitates of chromium nitride. The small peak at 399.4 eV may be associated with iron nitride.

3.4 Performance Evaluation

The W & M PSII implanted has shown promise as a surface modification instrument. The system met several of its goals:

1. The successful modification of the top surface layer of steel by nitrogen implantation. Surface spectroscopy shows the presence of interstitial nitrogen and nitride precipitates.
2. The PFN has delivered the required voltage pulse for the duration of the implant run.
3. The vacuum system meets the requirements of base pressure and operating pressure.
4. Contamination from the tungsten filament is minimal.

Several modifications are necessary to improve the PSII system for higher voltages and shorter implant times:

1. A new insulated sample stand has been constructed. The stand employs a large, alumina cylinder with triple-point protectors. A glass shield will protect the insulator from the plasma
2. A high power, electrode-less plasma generation system would be beneficial. A higher plasma density would result in a more uniform ion energy distribution.

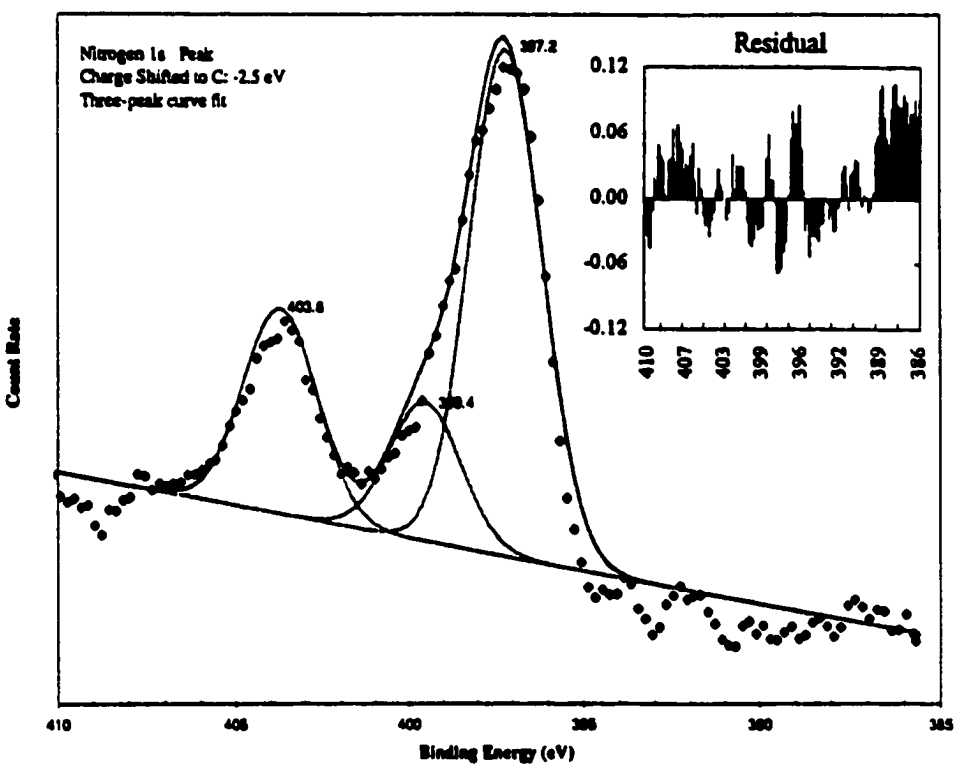

Figure 3.13: XPS of the nitrogen peaks on a 30 kV implanted sample. Dose was $\approx 10^{17}/cm^2$. Inset shows residual of normalized data.

3. The addition of transformer oil to the transformer container would suppress arcing from the high voltage terminals.

4. Higher repetition rates would be possible with a higher power capacitor charging power supply. The current supply is limited to 3 mA.

5. Protection of the charging power supply

The PFN, vacuum system, and plasma generation scheme proved capable of meeting the requirements of the initial PSII start-up.

3.5 Field Emission Suppression by PSII

The information from Chapter 2 on the nature of the anomalous emission site was conclusive; emitter structures on extended-area electrodes are non-metallic in nature. In the following sections, connections are made between the believed cause of the enhanced emission and the surface modifications of PSII.

The body of past experimental research clearly points to surface anomalies being the main factor in enhanced field emission from broad area electrodes. Also, several authors are revisiting the microprotrusion model [14, 15, 25], with any deviations from the Fowler-Nordheim law being ascribed to gas coverage or non-metallic layers. It is the goal of this thesis to propose PSII as an *ex situ* process for "pre-conditioning" electrodes.

3.5.1 Microprotrusion and Microparticle Detachment

With the application of the high voltage pulse, the electric field at the surface of the workpiece is on the order of $E = (M/e)\omega_{pi}^2 s_o$, where M is the mass of the ion, e is the fundamental charge, ω_{pi} is the ion plasma frequency, and s_o is the initial ion matrix sheath thickness. For nitrogen ions, a plasma density of 1×10^{10} cm^3, and a 30 kV pulse, the initial

ion matrix sheath thickness is

$$\begin{aligned} s_o &= \sqrt{\frac{2\epsilon_o V_o}{en_o}} \\ &= \sqrt{\frac{2\ 8.85\times10^{-12}\mathrm{F/m}\ 3\times10^{4}\mathrm{V}}{1.6\times10^{-19}\mathrm{C}\ 10^{16}\mathrm{m}^{-3}}} \\ s_o &\approx 2\mathrm{cm}. \end{aligned}$$

The electric field near the surface of the piece just after the formation of the ion matrix sheath is ($s|_{t=0} = s_o$)

$$\begin{aligned} E_{x=0,t=0} &= \frac{en_o}{\epsilon_o} s_o \\ &= \frac{1.6\times10^{-19}\mathrm{C}\ \times10^{1}6\mathrm{m}^{-3}}{8.85\times10^{-12}\mathrm{F/m}} \times 2\mathrm{cm} \\ &= 3\times10^{6}\ \mathrm{V/m} \end{aligned}$$

The effect of this field on surface microprotrusion will be considered. The treatment will follow the measurement of the charge and mass of particles emitted from a vacuum gap by Texier [7].

Consider a hypothetical microprotrusion, attached to the surface of an electrode. A half-spheroid shape will be assumed, with a and b the major and minor half-axis, respectively. This half-spheroid, subjected to a uniform field E parallel to its axis gets charged to:

$$Q_E = \pi\epsilon_o E b^2 \beta(\lambda) \tag{3.25}$$

where λ is the ratio of a/b. $\beta(\lambda)$ is given as

$$\beta(\lambda) = \frac{(\lambda^2-1)^{3/2}}{\lambda \log[\lambda + (\lambda^2-1)^{1/2}] - (\lambda^2-1)^{1/2}} \tag{3.26}$$

The force $F = Q_E E$ on the half spheroid with $a = 1\mu$m as a function the base radius b is shown in Fig. 3.14. Also shown is the ultimate strength of the spheroid as a function of the base radius. The tensile strength of stainless steel was taken to be 1000 MPa [51]. For one-micron high protrusions, only those with base diameter much less than 10 nm would become unstable under these field conditions.

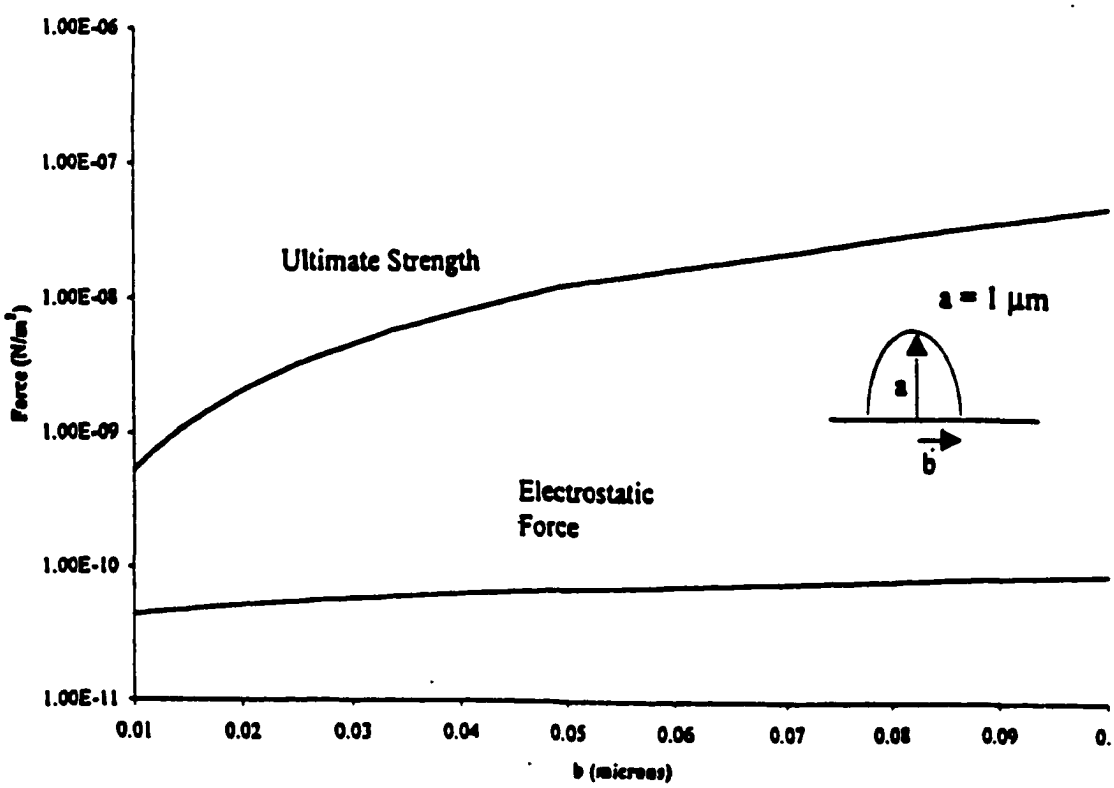

Figure 3.14: Electrostatic force on hypothetical microprotrusion. Top curve shows ultimate strength as a function of protrusion radius. Bottom curve shown force from electric field vs . protrusion radius.

The detachment of microprotrusions is an upper limiting case. In the case of microparticles resting on the surface, one must consider the van der Waal's force. This force arises between dipole-dipole interactions of molecules with a net positive or negative charge distribution. These are considerable in magnitude, approximately 10^{14} N/cm^2 [1]. It is difficult to determine the amount of contact area involved. Also, surface adsorbates lower adhesion forces, so the vacuum environment is an issue [1]. However, the work of Cranberg [6] and Texier [7] indicates that microparticles are ejected from electrode surfaces under field strengths of similar magnitude as those in the PSII environment.

3.5.2 Ion Bombardment

A unique aspect of PSII is that any site on the extended surface that enhances the field will draw more ions toward it. Kim et al [52] investigated the effects of low-energy (1-1.5 kV) nitrogen ion bombardment on sharp atom-probe field-ion microscopy (APFIM) tips. Sharp tips of Fe-3 at. % Mo tips were biased to several kilovolts in a nitrogen atmosphere at 10^{-5} to 10^{-3} Torr. Field emitted electrons ionized the background gas molecules, and the ions follow the field line back to the tip. It was found that the bombardment *sharpened* the tips. Kim and coworkers believed the ions were impacting on the sides of the tip at an angle. This causes sputtering of the tip material and the observed sharpening. In PSII, a situation may develop where a microprotrusion is sharpened from the sputtering, the field is enhanced around the sharpened tip, the ion bombardment is enhanced further, and the microprotrusion is destroyed. Sputter yields for metals is on the order one for ion energies in a PSII environment. Doses of 10^{17}/cm^2 will result in the removal of several hundred Angstroms of material from the surface. The high aspect ratio whisker structures, with bases of sub-micron dimensions that give rise to high field enhancement, may be thinned even further from the sputtering. The combined effect of the erosion of the sharp protrusions, and the electrostatic stress computed above, may lead to a situation of microparticle erosion and detachment.

The duty cycle of PSII is typically small. For a 40 Hz pulse train of 10 μsec pulses, the duty cycle is only 0.04%. The workpiece is simply submerged in a plasma for 99.96% of the total process run, which is typically on the order of a few hours. The energy of the ions from the plasma during the off-pulse is about 10 volts. This energy is too low to induce any particulate removal, and may serve only to remove adsorbed hydrocarbons from the surface.

3.5.3 Electronic Modification

High energy ions impacting on a solid surface cause a number of structural changes and electronic excitations. The energy loss of the impacting ion is divided into two categories, electronic and nuclear. As the ion enters the crystal lattice at high energy, electronic processes dominate. Secondary electron production, ionization, and electron-hole formation strip energy from the ion. As the ion slows, nuclear collision cascades are set into motion, and target atoms are displaced. These atoms can continue to displace more atoms. Finally, the ion either comes to rest, or exits the target material. The loss of energy as a function of distance into the solid can be written as

$$-\frac{dE}{dZ} = N[S_e(E) + S_n(E)] \tag{3.27}$$

Where N is the target atom density, and $S_e(E)$ and $S_n(E)$ are the electronic and nuclear stopping powers, respectively, in units of eV cm^2. Electronic energy loss is on the order of 5-10 eV/Angstrom, and nuclear energy loss is on the order of 10-100 eV/Angstrom. The Lindhard-Scharff-Schiott (LSS) theory quantified the two energy loss terms. $S_e(E)$ is proportional to $\sqrt{E}$. $S_n(E)$ can be written explicitly as

$$S_n(E) = \frac{1}{N}\frac{dE}{dz} = \frac{\pi}{2} a Z_1 Z_2 q^2 \frac{M_1}{M_1 + M_2} \tag{3.28}$$

here M_1, M_2, Z_1, Z_2 are the mass and atomic numbers of the incident ion and target atom, respectively, q is the electronic charge, and a is the screening radius for collision. This number lies between 0.1 and 0.2 Angstroms. This theory has been well supported by implantation experiments [50].

The enhanced emission model of Latham *et al* relies on electrons gaining energy by the applied field, accelerating through the conduction band of the charged insulating "site", and surmounting the surface barrier created by the surface states. As electrons are injected into the trap states near the metal-insulator interface (Schottky barrier), the conduction band of the insulator is raised toward the Fermi level in the metal. This leads to a buildup of charge in the insulator (amorphous, impure insulator with semiconductor-like properties) and an effective screening of the metal-insulator interface from the electric field. The field is decreased, and tunneling through the Schottky barrier is reduced. This electronic model was proposed by Bajic and Latham [53] when discussing the gas conditioning of electrodes. Gas conditioning involved admitting a known gas into the electrode environment during the conditioning process. For certain gas species, the current is quickly lowered. Alpert *et al* explained gas conditioning through selective ion bombardment of the emission site [54]. Electrons ionize the gas, and the ions accelerate back to the emission site and sputter foreign material from the surface. Bajic and Latham found that gas conditioning was only effective for select gas species (e.g. He, Ar), and a de-conditioning effect was seen with some gases (O_2, Ne). Some gases had no effect at all (H_2, N_2). These results do not favor a cleaning or sputtering effect of the emission sites, as H_2 is very effecting at removing surface contaminants. The conditioning effect could be reversed by a 250° C cycle of the cathode. The temperature cycle should have removed many surface contaminants through desorption. However, current after the temperature cycle was higher than the current just after the conditioning had leveled off. The de-conditioning after the cycle was attributed to the electrons being excited from their respective traps (Poole-Frenkel Emission) , and reducing the "screening" effect.

In the MIV Model developed by Latham, charge carriers are assumed to fill the trap states upon field application. When the surface traps are full, emission is prevented until the field is raised further. However, Latham assumes the trap density is low enough that the field can still penetrate the IV barrier. An increase in the trap states would tend to

shield the barrier from the applied field, and emission could be prevented. Ion implantation of the oxide layer of steel will increase the number of trap states through the formation of vacancies, interstitial, and dislocations, as in the gas conditioning model by Bajic and Latham. Gomer [10, pages 24] indicates screening can be sufficient to shield the metal-insulator interface from the external field; the semiconductor takes on a metallic behavior in this respect. The effects of PSII on high voltage electrode systems will be investigated in the following chapters of this thesis.

Chapter 4

Experimental Apparatuses

In order to fully characterize the effects of PSII and other surface modification techniqes on anomalous emission, two separate experimental apparatuses were constructed. The first apparatus was integrated into the sample preparation chamber of the VG ESCALab MKII at William and Mary. X-ray Photoelectron Spectroscopy, Scanning Electron Microscopy, and Auger Spectrocopy are available to fully characterize the surface of the electrodes before and after voltage applications of up to 50 kV. A larger, higher voltage test facility has been constructed at Jefferson Labs. This system will allow future investigations of six inch diameter electrodes at voltages in excess of 100 kV.

4.1 The William and Mary Test Apparatus

4.1.1 Design Considerations

Figure 4.1 shows the construction of the small scale test apparatus at William and Mary. Figure 4.2 shows the general layout of the ESCALab MKII. The test electrodes are small enough to be easily loaded into the ESCALab, yet large enough to provide a good measure of the effectness of a given surface treatment. The electrodes are loaded into the system via a small load-lock chamber. Sample manipulators are used to transfer up to eight electrodes through the preparation chamber, and onto a carousel in the analysis chamber. The anode is a highly polished sphere-shaped electrode, and is attached to the 60 kV ceramic

insulator. A linear motion feedthough was used to support the cathodes, and allowed the cathode-anode gap to be closed to the desired spacing. Resolution of the feedthrough was ±5 microns. The feedthrough was insulated from the chamber with a small ceramic break to allow emission measurements.

4.1.2 POISSON Calculations

A requirement of the test electrodes is that the electric field across the surface of the cathode be uniform to within a few percent of the maximum field strength (i.e., no field enhancements due to edge effects). Electrostatic field strengths for this geometry were modeled with the POISSON/SUPERFISH group of computer codes from Los Alamos National Lab. The POISSON subset handles electrostatic (or magnetic) computation, and SUPERFISH computes electrodynamic fields for accelerator cavity design. POISSON is a finite element package that allows the user to enter the geometric constraints of an electrode system, dielectric constants, and electrode voltages. Poisson's equation is then solved by finite difference iterations, and the potential gradients in free space and dielectric material are computed.

Several electrode geometries were modeled with POISSON, with the field-uniformity constraint in mind. The cathode design needed to be such that machining of the pieces was simple, as many were needed. A simple disk, with edges radiused, was chosen. The potential gradients were computed by POISSON, and the profile of the anode adjusted to meet the field-uniformity criterion. Figure 4.3 shows the electrostatic field strengths in the gap for the proposed electrode shapes. The geometry is cylindrically symmetric, so only half of the geometry is computed. In Fig. 4.4, the electric field is plotted for several points along the surface of the cathode, extending along a radial line from the center of the cathode outward. The field is uniform to within a few percent within the gap. It drops to 90% at ~0.22 inches from the center, and tapers off to the edge. Nowhere is the field higher than at the center. The field across the surface of the cathode is well within the field uniformity constraints.

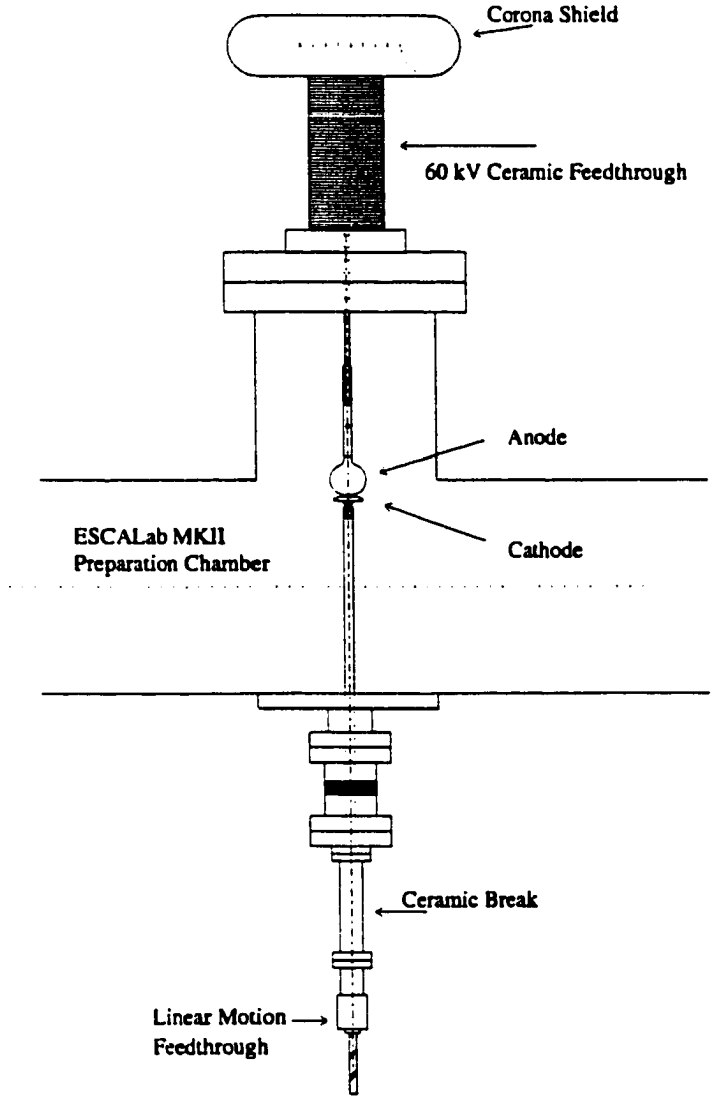

Figure 4.1: Field emission test apparatus schematic constructed on ESCALab MKII sample preperation chamber. Anode is mounted on 60 kV feedthrough. Cathode is mounted on linear motion feedthrough and low voltage ceramic break.

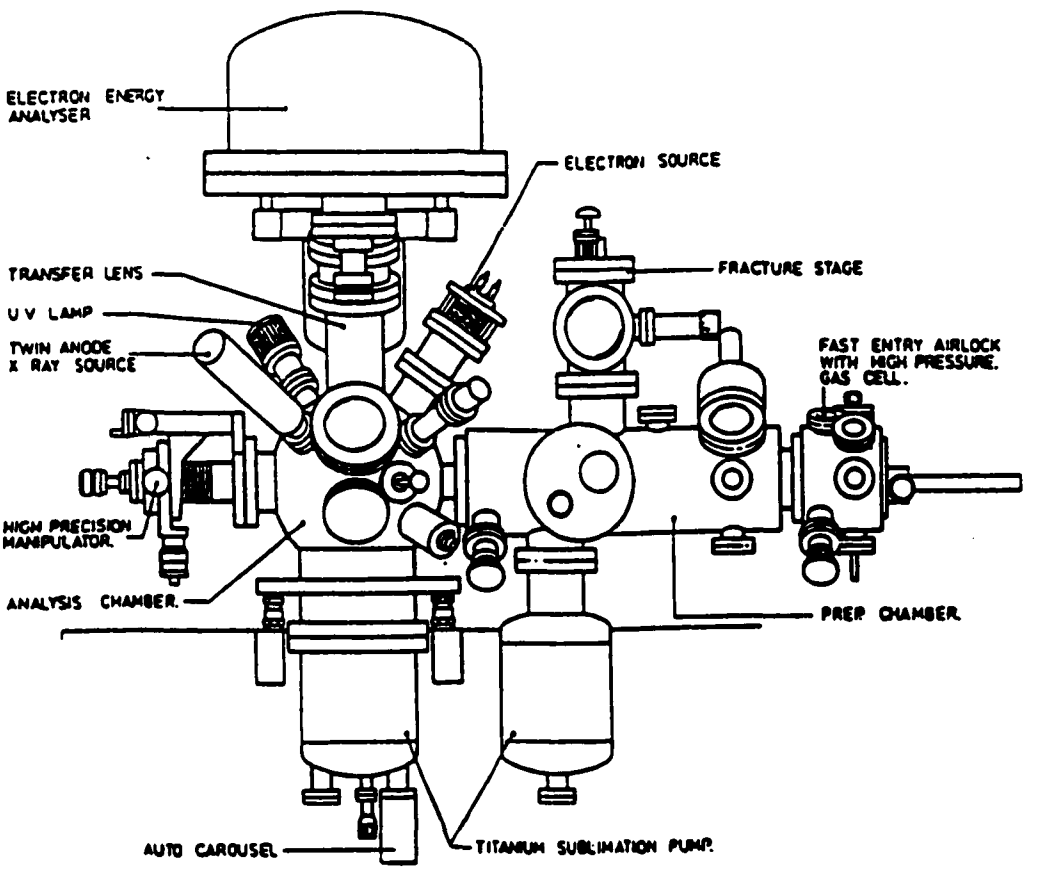

Figure 4.2: Diagram of the ESCALab MKII. The left side of the system is the analysis chamber. The right side in the preperation chamber and load-lock

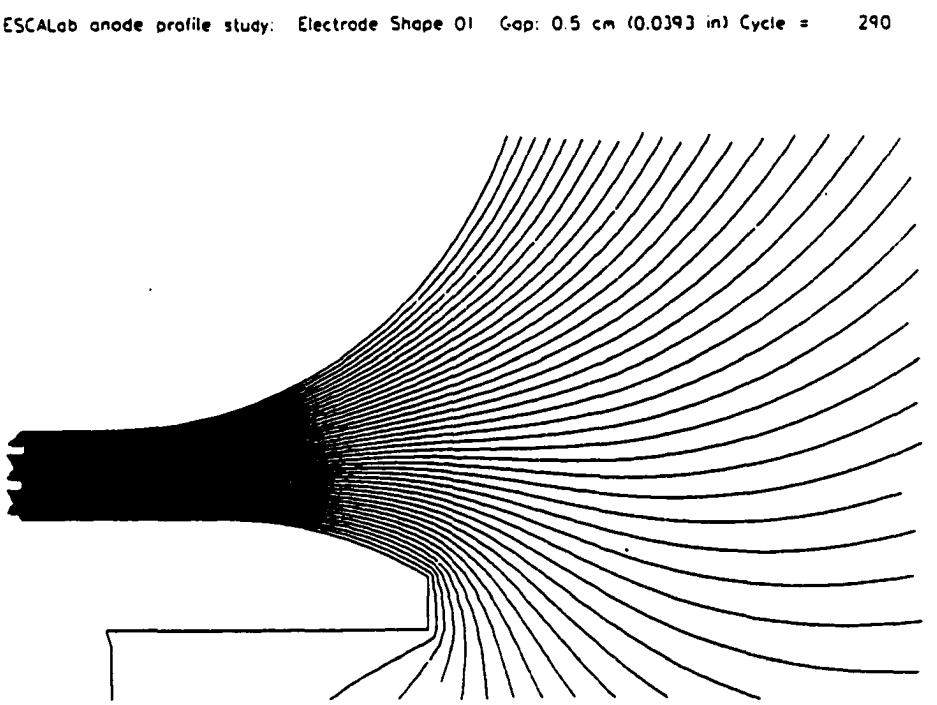

Figure 4.3: POISSON calculations for electrostatic field strengths. Maximum field is 20 MV/m at the face of the cathode. Field strength across cathode surface uniform to within a few percent.

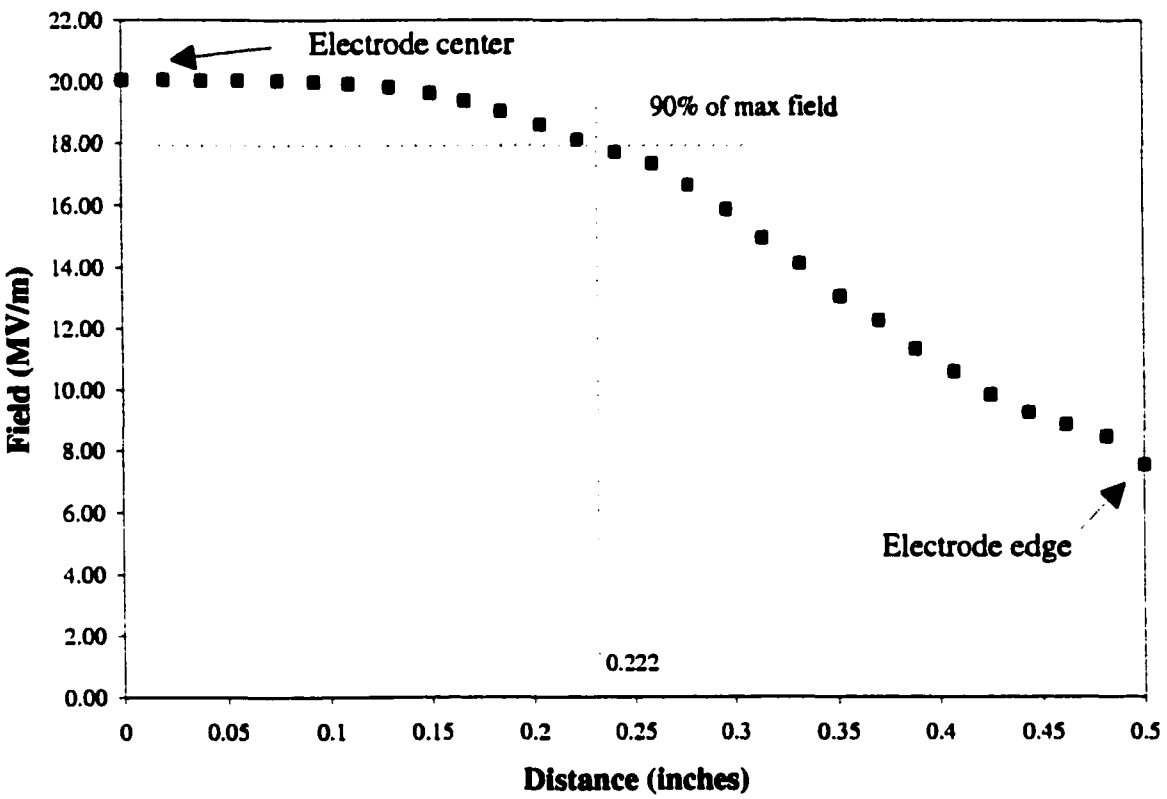

Figure 4.4: Field strengths computed for ESCALab test electrodes (see Fig. 4.3). Values taken near the surface of the cathode along a radial line beginning at the center of the electrode and extending outward toward the edge.

4.1.3 Current-Voltage System Design

The application of high voltages and the measurement of field emission currents was computer controlled with LabView software. A general schematic of the electronics and control hardware involved is shown in Fig. 4.5. The system allowed repeatable voltage ramps to be applied to the gap, and current to be measured and stored. The high voltage power supply (HVPS) was a Bertan model. An analog signal was used to program the positive output voltage to the anode. Current measurements were made with a Kiethley Model 485 picoammeter with GPIB interface. The 485 was protected from microdischarge and breakdown activity by the protection circuit shown in Fig. 4.5. The circuit employs a spark gap with a breakdown voltages of 2 kV. Two diodes are used to shunt high voltages that may appear on the cathode side to ground. In all tests, a 160 kV, 40 Watt, 15 MΩ resistor is placed on the anode side of the arrangement to limit the current available in the event of a complete voltage breakdown.

The voltage ramp was applied as follows: The voltage was slowly ramped to a low value, typically 10 kV. With the usual gap of 2.5 mm, this initial field strength was 4 MV/m. Current data was taken at a frequency of about 1 Hz as the voltage was held constant at this initial value. If the average current was below a set value (5 picoamps), after a set plateau time (60 - 120 sec), or if the current was above the set threshold, but the standard deviation was low (20%), the voltage would proceed to the next plateau. Voltage steps were in 1 kV increments. This procedure provided a standard methode of field application.

4.2 Jefferson Labs Test Apparatus

The electrodes used in the photo-electron guns at Jefferson Labs are several hundred square centimeters in area. In order to fully assess the effectiveness of a given surface treatment, a test apparatus is needed that would allow evaluation of similar size electodes. A system at Jefferson Labs was designed and constructed with the following criteria in mind:

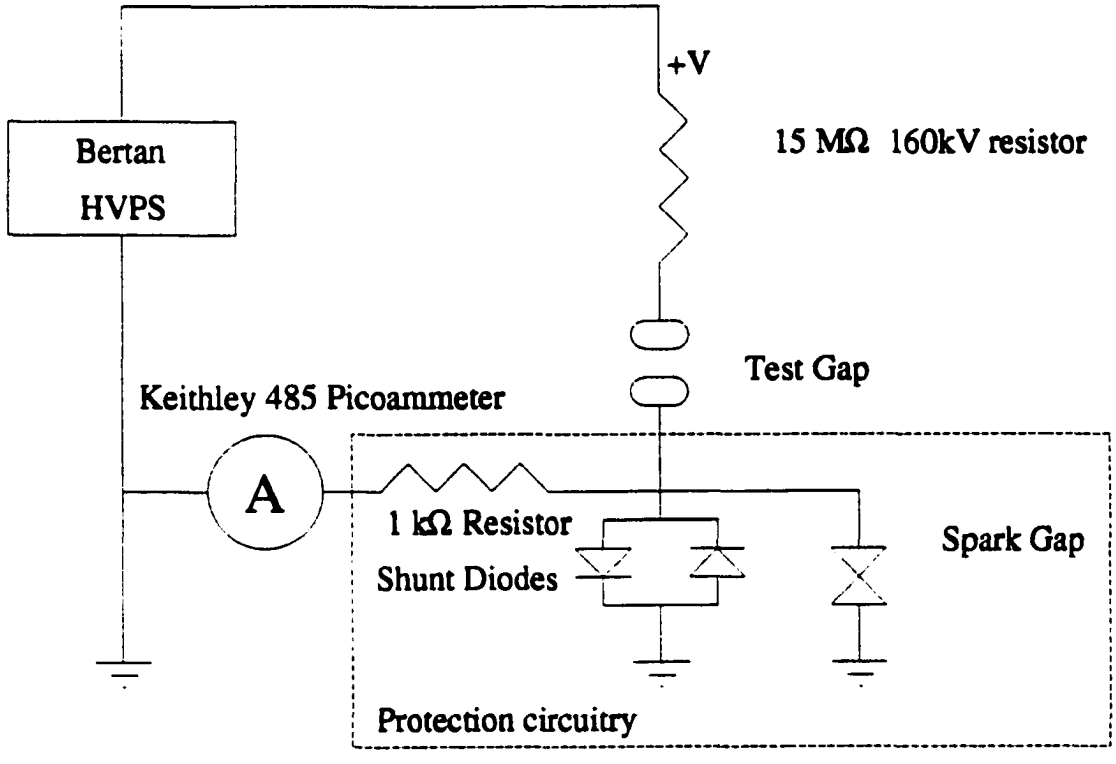

Figure 4.5: The schematic for the W & M FE test apparatus. A 15 MΩ resistor is used to limit the current. The protection ciruit employs a spark gap, shunt diodes, and 1 kΩ resistor.

1. Electrodes, both anode and cathode, must be designed to apply a uniform field in the gap region, with minimal field enhancements.

2. The electrodes must be constructed such that installation and removal is simple, and without any contact to the electrode surfaces that will be in the high field region.

3. The gap must be adjustable.

4. One electrode is to be mounted such that tilt adjustment is possible, and the electrodes must be made parallel to within a few micrometers across the gap.

5. The electrodes should be simple in design, so surface treatments are not made difficult due to any additional fixtures on the piece.

6. The entire UHV vacuum system must be bakeable to 250 °C. The system is to be designed such that clean, UHV conditions are easily and quickly attainable.

7. Partial and total pressure gauges are to be included.

8. Viewports are to be shielded from high voltage electrons by shutters.

A diagram of the Jefferson Labs high voltage test apparatus is shown in Fig. 4.6. The first criterion of field uniformity is met by the Rogowski profile. This profile was calculated by Rogowski by solving for the equipotential lines between two parallel plates. By solving Laplace's equation $\nabla^2 V = 0$ for the fringing fields at the ends of two charged parallel plates, one obtains the equipotential lines shown if Fig. 4.7. If a particular equipotential field line in Fig. 4.7 is replaces by a conducting surface, the remaining field lines will remain unchanged. Rogowski calculated the first field line where the maximum field strength is within the uniform-field central gap region and tapers off as one moves outside the gap is $v = \pi/2$. This field line is given by the equations:

$$x = \frac{a}{\pi}(u + 1 + e^u \cos v) \tag{4.1}$$

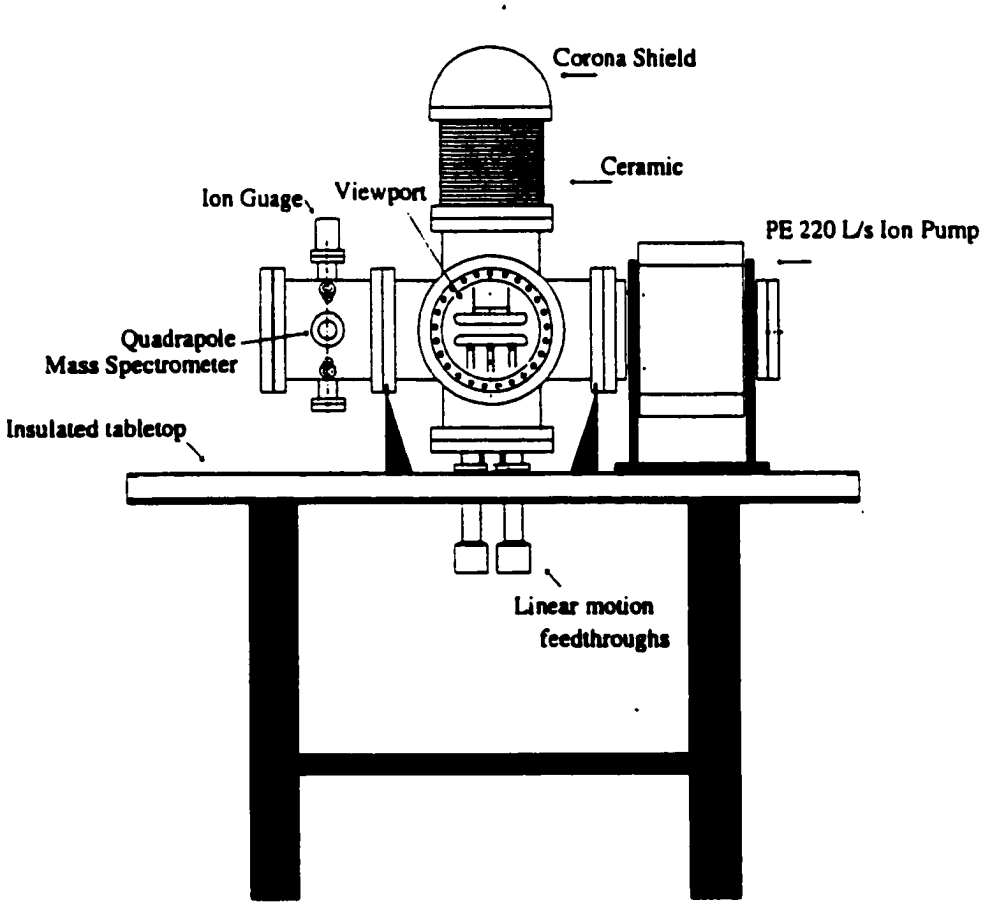

Figure 4.6: Diagram of the Jefferson Labs Field Emission Test Apparatus.

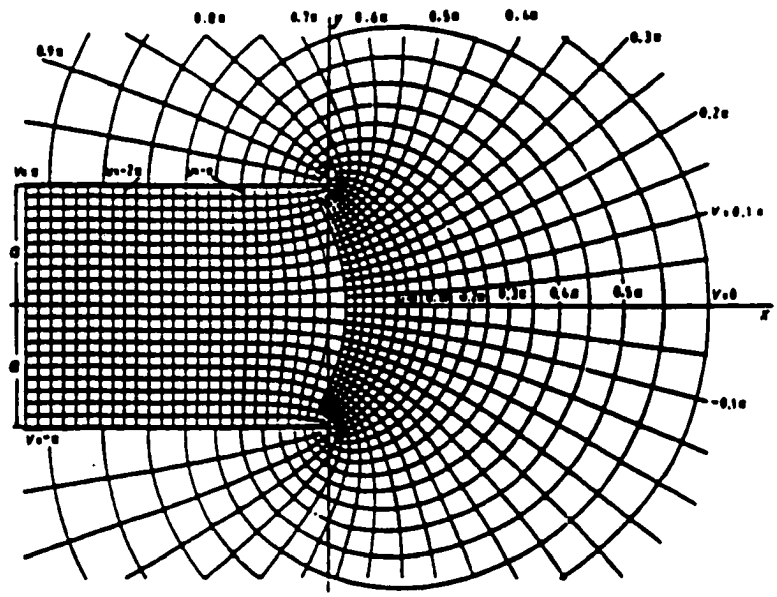

Figure 4.7: Equipotential lines for a pair of charged parallel plates.

$$y = \frac{a}{\pi}(v + e^u \sin v) \tag{4.2}$$

Setting $v = \pi/2$ and combining the above equations, one arrives at

$$y = \frac{a}{\pi}\left[\frac{\pi}{2} + e^{(\pi\frac{x}{a}-1)}\right] \tag{4.3}$$

The electrode edges were designed using this equation. This profile was used at the edge of the electode for a few centimeters. An equation for a circle was begun at the point where the Rogowski equation was terminated, to "finish off" the electrode edge. Both position and slope between the two equations were set equal to solve for position of the center of the circle, and to obtain a smooth transition at this point. Figure 4.8 shows the geometry used to determine electrode shape.

In order to confirm that this profile would meet the first criterion, POISSON was used to calculate the equipotential lines for two parallel electrodes of the profile in question. Figure 4.9 shows the field strengths in the gap. The field strength across the surface of the electrode from center to edge is shown in Fig. 4.10. The maximum field strength is at the center of the gap, and gradually tapers off, meeting the first criterion. Small variations in the field strength at the edge of the electrode are a result of the discrete nature of the electrode surface in the finite-element calculation.

The second criterion, that the electrodes could be easily installed and removed, was met. The top electrode (the cathode) was attatched to a specially designed mounting fixture. This fixture could be easily connected to the cathode support tube by a single worker. Appendix B shows the mechanical drawings for this fixture. The bottom electrode (the anode) rested on a three point support with ceramic spheres electrically isolating the cathode from the chamber. Because this electrode is mounted with high-field surface facing up, it could be held in one hand and simply placed on the supports.

The third and forth criteria, that the gap be adjustable, are met by use of heavy-duty linear motion feedthroughs acting as the anode supports. The feedthroughs are independently adjustable, and have a resolution of ±0.0002", allowing accurate determination of

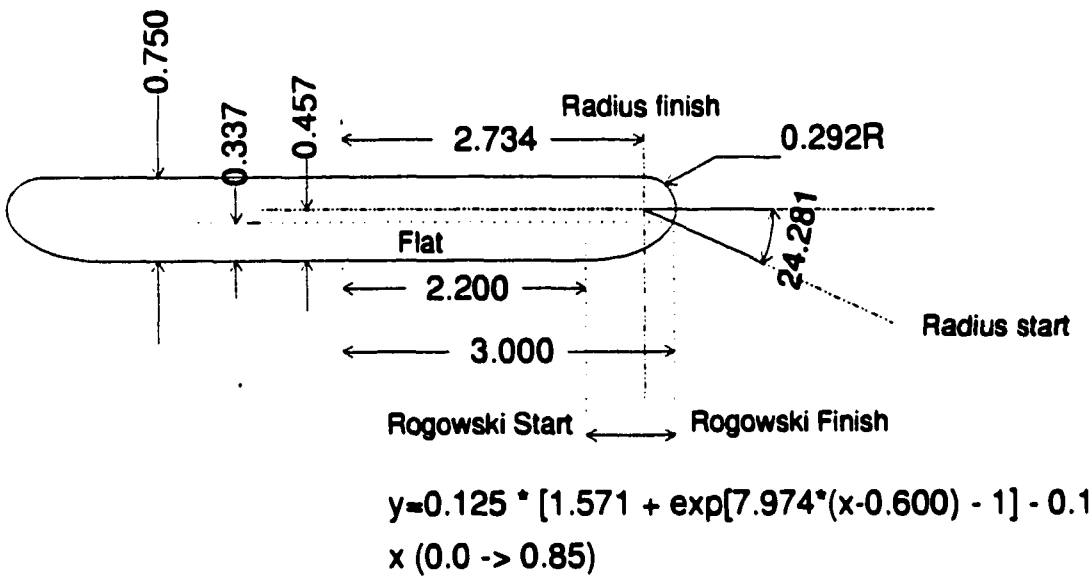

Figure 4.8: Diagram of Rowgowski profiled electrode edge. The Rowgowski profile was extended to $x = a$, and a radius r was used to complete the electrode profile.

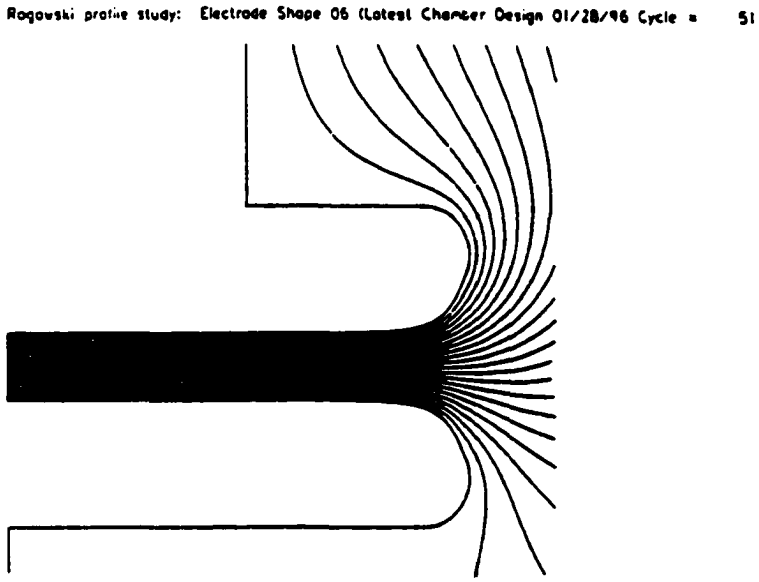

Figure 4.9: POISSON results from Rowgowski-profiled electrode edge. The maximum field strength is at the center, and tapers off as one moves outside the gap.

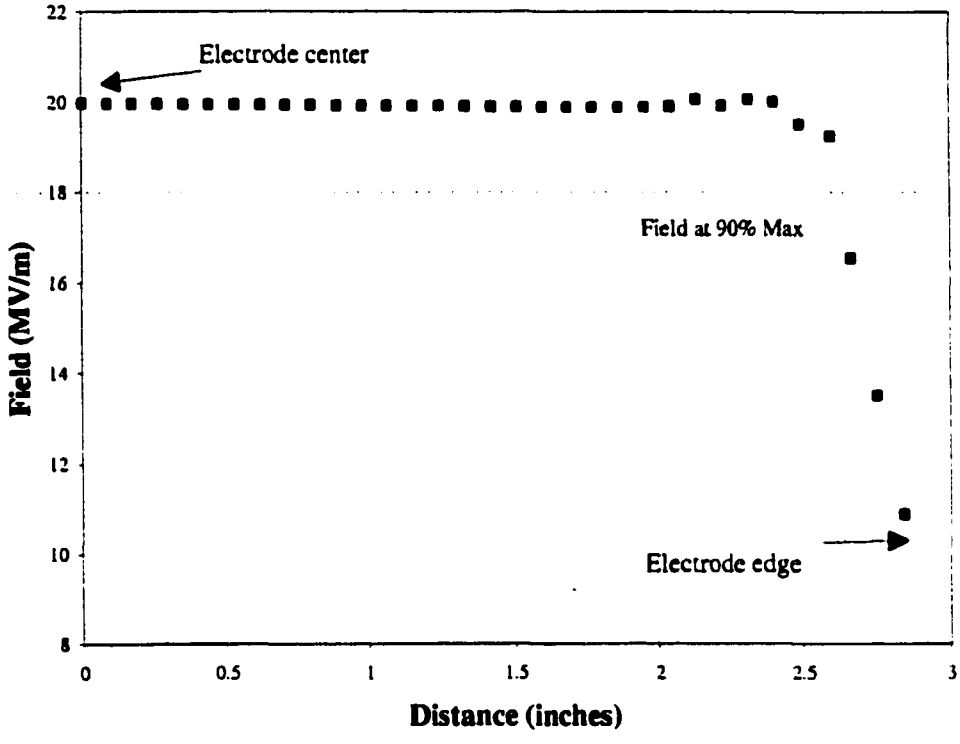

Figure 4.10: POISSON results from Rowgowski profiled cathode. See Fig. 4.9. Surface field is plotted along a radial line from the center of the electrode outward toward the edge.

gap width. The electrodes have accomodations for highly sensative tiltmeters. Biaxial models will be installed on the back of each electrode, and will be used to make the electrodes parallel to within a few microradians.

The electrodes were designed to be easily machined and handled. Their flat, disk shape with mounting holes on the back make them easily mountable in most process chambers. This meets the fifth criterion.

The last two criteria are met by proper UHV practice. All surfaces are cleaned ultrasonically in a mixture of Microclean and de-ionized water. This is followed by an ultrasonic treatment in ethanol, then isoproponal. A Granville-Phillips Stable-Ion ionization gauge measures total pressure, and a Stanford Research Systems Quadrapole Mass Spectrometer measures the partial pressure of the gas species remaining in the chamber.

Chapter 5

Results

5.1 Electrode Performance

The emitted current between the high voltage electrode system in the ESCALab was measured for several surface treatments of the cathode. The surface of the anode was not modified in this work. Cathodes were positioned 2.5 or 5.0 ±0.05 mm from the anode, depending upon the desired field. As described in Chapter 4, computer controlled voltages (up to 50 kV) were applied to the gap, and the emitted current from the cathode was measured. Studies were performed on thin film coated electrodes, electron beam treated electrodes, ion implanted electrons (beam and PSII), and control electrodes. The measurement of emission from clean, unprocessed, unpolished, electrodes serves as a benchmark for comparison of other process techniques. Results from polished electrodes serves as a process benchmark. Data from these experiments will be compared to the alternative process techniques explored in this study.

Several parameters are of interest during the investigations: (1) the "turn-on" field, that is, when the emission current reaches a value that is $> 0.1nA$[1], (2) the general behavior of the current at each voltage plateau, (3) the final current at the maximum field strength, and (4) the background pressure during the voltage ramp.

[1]This value was arbitrarily chosen as it was well above the noise level of the picoammeter. The source of the noise was determined to be the high voltage power supply.

5.2 Experimental Procedure

To maintain consistency during the experiments, a standard procedure was developed for preparing electrodes:

- For polished electrodes: The electrodes were polished according to a procedure used at Jefferson Labs. The procedure involved hand polishing with successive grades of SiC paper (240, 320, 400, 600), followed by polishing with successive diamond paste grits (9, 6, 3, and 1 μm).

- Each electrode was cleaned by a standard procedure: A 10 minute ultrasonic agitation in a mixture of DI water and Alconox detergent, followed by a 20 second DI water ultrasonic rinse (3 times), and a 5 minute ultrasonic agitation in isopropyl alcohol. The electrodes were allowed to dry in an air environment.

- Electrodes were loaded into the ESCALab, and the entire system baked at 150 °C for 24 hrs. This removes most of the adsorbed water and hydrocarbon contaminants. The base pressure of the ESCALab was $\leq 1 \times 10^{-9}$ Torr after the bakeout. A spectrum of the partial pressures after a typical bake is shown in figure 5.1

- After the bake and the system had cooled, XPS and Auger spectra were taken to determine the constituents on the surface of the cathodes.

- I-V curves for each electrode were taken following the procedure explained in Chapter 4.

- Total pressure curves for the voltage ramps were recorded. Partial pressures were monitored in some cases with the mass spectrometer.

- Surface spectroscopy of the electrodes was repeated periodically

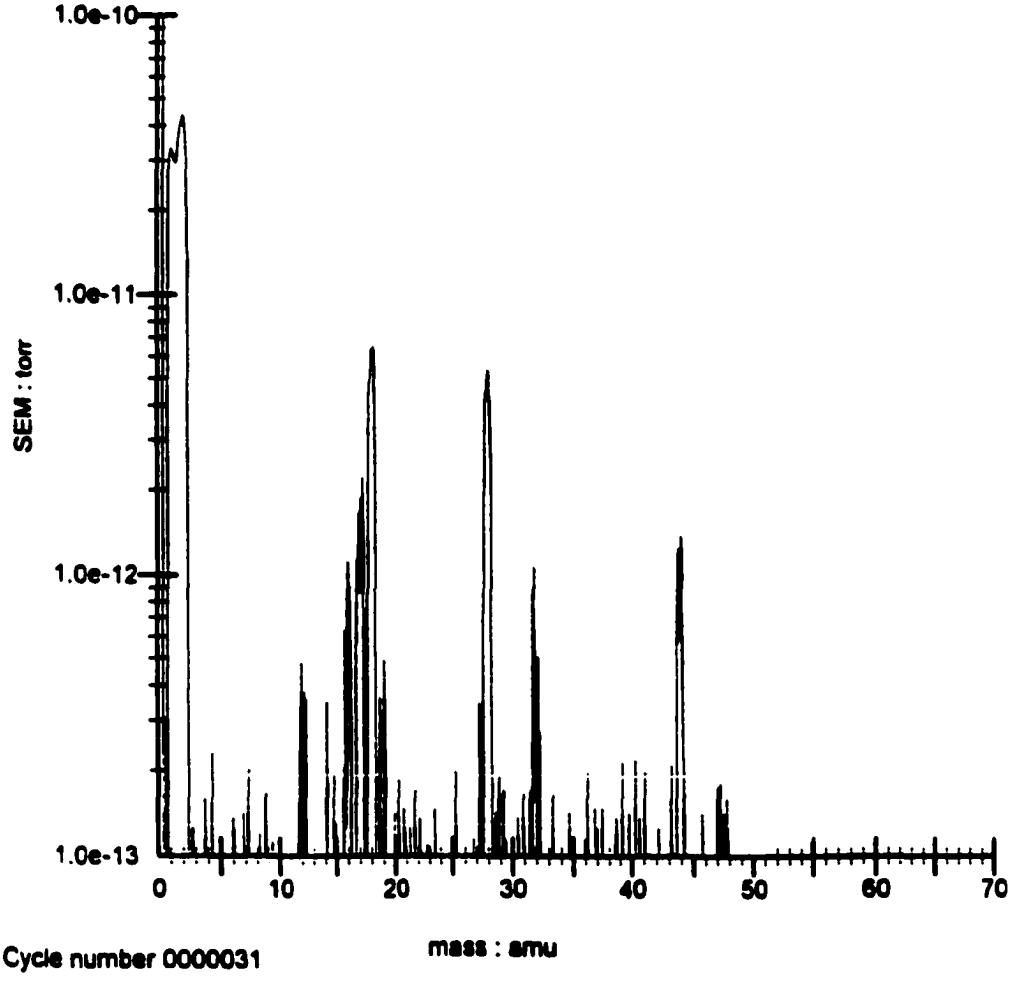

Figure 5.1: Background gas spectrum after the 24 hr. bake of the ESCALab system. Main constituents are H_2 (mass 2), H_2O (mass 18), CO (masses 28 and 12), and CO_2 (mass 44). Nitrogen would have appeared as masses 28 and 14.

5.3 Surface Spectroscopy Techniques

XPS, Auger, and SEM analyses were performed on the electrodes. Surface constituents were detected by XPS. Individual contaminants viewed on the surface with SEM were analyzed with Auger Spectroscopy.

X-ray Photoelectron Spectroscopy

XPS, or ESCA (Electron Spectroscopy for Chemical Analysis), is a method of resolving individual surface components by irradiation of the sample with X-rays. MgK_α (1253.6 eV) or AlK_α (1486.6 eV) X-rays are commonly used. The photons penetrate the solid a few micrometers and interact with the surface atoms. Electrons are emitted via the photoelectric effect. The emitted electrons have an energy of

$$KE = h\nu - BE - \phi_s \tag{5.1}$$

where $h\nu$ is the energy of the photon, BE is the binding energy of the orbital from which the detected electron originated, and ϕ_s is the spectrometer work function. A typical spectrum is shown in Fig. 5.5. Several peaks are associated with each element, depending upon the particular shell involved in the ionization. The binding energies of the core electrons are characteristic of each element, so the spectrum gives a "fingerprint" for each element. The broad background is associated with electrons originating from atoms deep (> 10 Angstroms) within the surface that have thermalized through collisions in the solid. Therefore, XPS is surface sensitive, in that only those electrons originating from the top few atomic layers contribute to the useful spectral peaks. The XPS process is shown in Fig. 5.2a. Also observed in XPS spectra are peaks associated with the Auger electron. The source of the Auger electron is described in the next section.

Auger Electron Spectroscopy

The Auger process is shown in Fig. 5.2b. Several steps are involved in the ejection of the Auger electron. First, a core electron is ejected by an incident photon or an incident

electron from an electron gun. An outer electron falls into the lower orbital, filling the vacancy. The excess energy remaining after this transition is carried off by either a photon or an electron. The electron ejected is the Auger electron, and its energy is characteristic of the element. Typically, electron beams are used in AES for chemical identification. If an X-ray photon initiated the Auger cascade, the process is termed X-AES (X-ray induced Auger Electron Spectroscopy).

Secondary Electron Microscopy

SEM involves rastering a high voltage electron beam (5 - 30 kV) across the surface of a sample. The incident beam ejects backscattered primary electrons and secondary electrons from the surface of the sample at the beam spot location. The electrons emitted from the sample impinge upon a scintillator screen. The light produced by the scintillator is then detected by a photo-electron detector. The intensity of the ejected electrons is sensitive to surface topography and chemical composition. The intensity of the detector signal is used to create a three dimensional image of the surface.

5.4 Surface Characterization

An SEM image of a dust particle found on a polished sample is shown in Fig. 5.3. The Auger spectrum in Fig. 5.4 revealed it to be primarily carbon. It is not possible to say if this particle was a source of anomalous emission. However, it is important to note that, although efforts were made to keep the electrode free of particulates, this type of contamination exists on the cathodes.

An X-ray photoelectron spectrum is shown in Fig. 5.5. The major peaks are labeled [55], with the designator (A) meaning the associated Auger peak (X-AES). A generalized approximation for the atom fraction of a surface constituent on a sample C_x, is

$$C_x = \frac{n_x}{\sum_{i=1} n_i} = \frac{I_x/S_x}{\sum I_i/S_i} \tag{5.2}$$

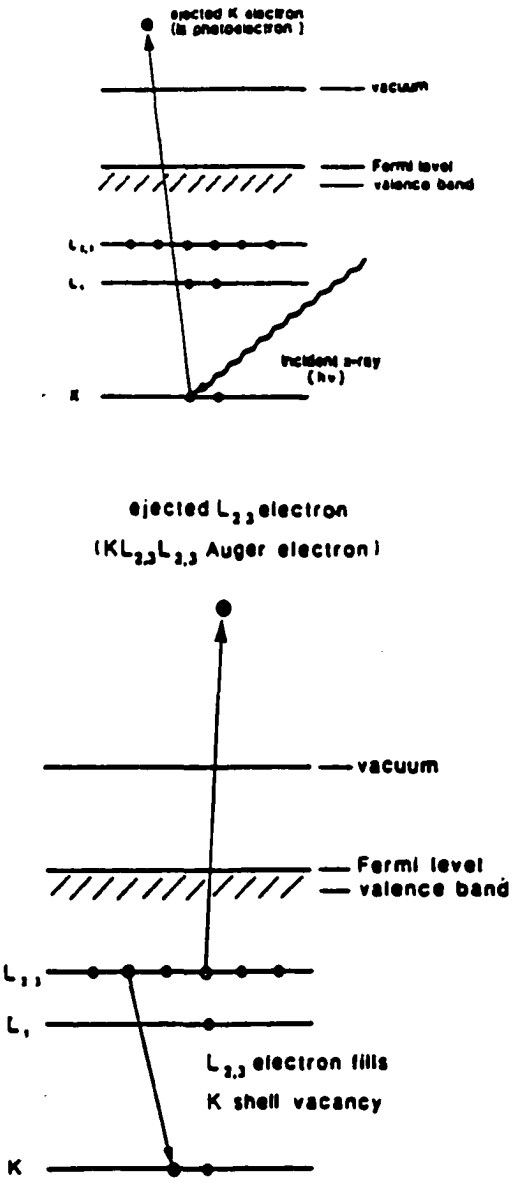

Figure 5.2: (a) A diagram of the photoelectric process. A core electron is ejected by the absorption of a photon. (b) A diagram of the Auger process. An electron from a higher shell drops to fill a vacancy created by an incident photon or electron. The Auger electron is ejected to carry off the excess energy [55].

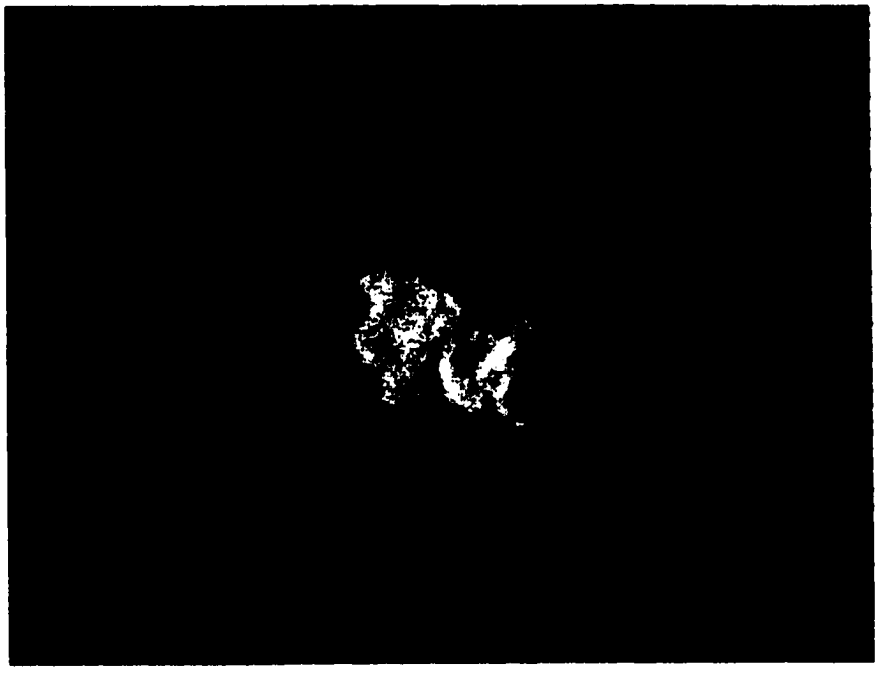

Figure 5.3: SEM image of particle on surface of polished electrode. Size is approximately 50 μm.

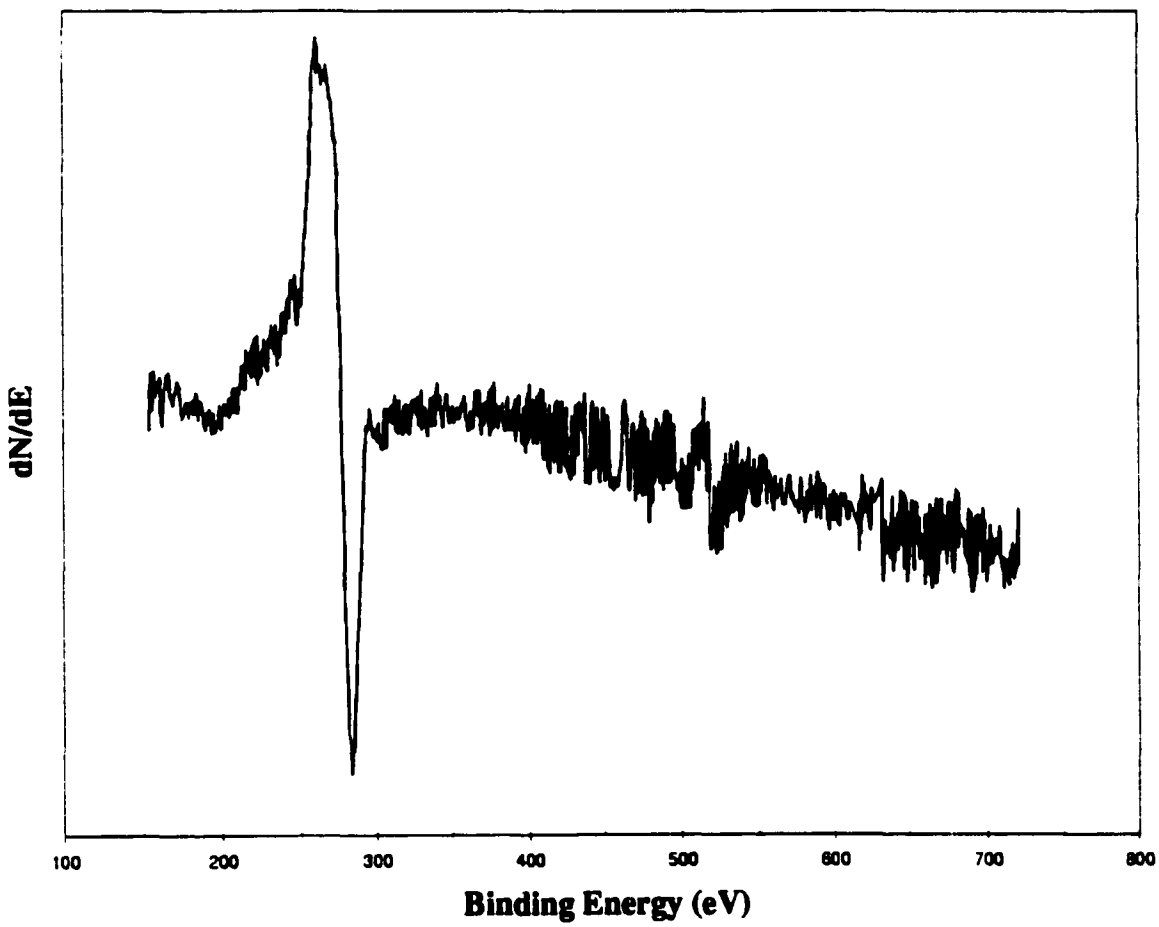

Figure 5.4: Auger analysis of particle shown in Fig. 5.3. The carbon peak is at 282 eV. Oxygen is at 503 eV. Peaks associated with the iron in the stainless steel would appear around 700 eV.

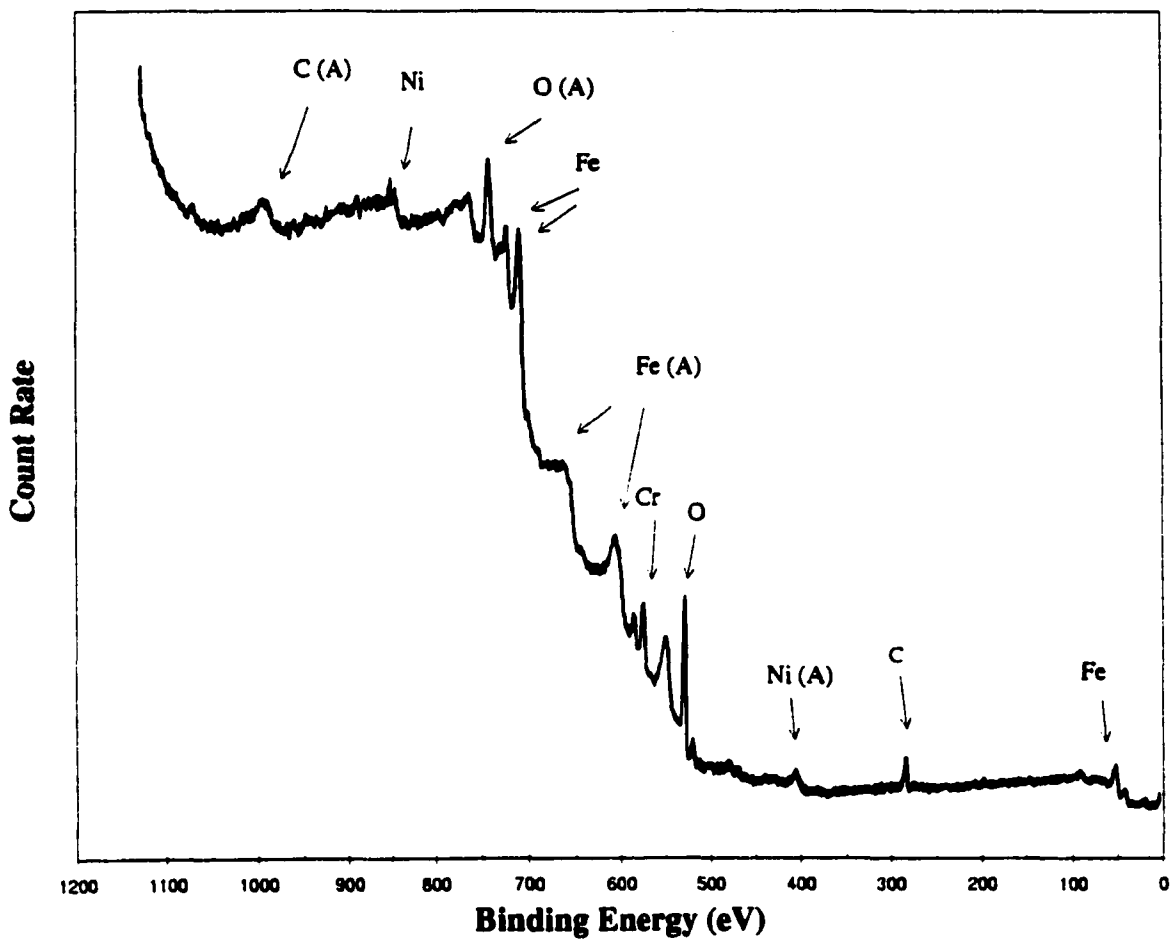

Figure 5.5: X-ray Photoelectron Spectrum of a 1μm polished sample. Sample was baked at 150 °C for 24 hrs. The major core-electron peaks are labeled, and Auger peaks are labeled with the designator (A).

where n_x is the surface concentration of the element in question, $\sum_{i=1} n_i$ is the sum of all the surface constituents. I_x is the area under the main spectral peak, and S_i is the atomic sensitivity factor (ASF) for the individual component [55]. The ASF is based upon calculated cross-sections for each element, and is a measure of how "sensitive" a particular element is to photo-emission. Note that the ASF for carbon is about one tenth that of iron, and carbon is present to less than one tenth of a percent in stainless steels. The carbon peak associated with the elemental composition of stainless steel, therefore, would only be one hundredth the size of the iron peak. It is concluded that this peak, therefore, is associated with a hydrocarbon layer.

5.5 General Emission Behavior

Figure 5.6 shows current and voltage data from one of the unpolished samples. The stair-step line represents the field ($E = V/d$) ramp. The field, in MV/m, is read on the right-hand axis. The current is read on the left hand axis in amperes. The turn-on field for this sample was about 6.5 MV/m. The current at the final field (10 MV/m) was 1.8 μA. The gap in the current data at t=2250 is the results of a microdischarge deactivating the picoammeter. A few seconds were needed to reset the meter. The spikes in the data at each voltage increment are the result of the capacitive charging ($I/C = dV/dT$) of the gap. Spikes are collected as data only if the time of the charge current (time of voltage increment) is coincidental with the data sample.

It is possible that many emission sites are active over the surface of the cathode, as discussed in Chapter 2. The current measured from the 1 inch diameter cathodes is the total integrated current from the cathode, so it is not possible to resolve individual emission sites. The total pressure during this ramp is shown in Fig. 5.7. Although the exact source of the gas increase is not known, it may be due to gas desorption from the cathode emission site, heating of an anode "hot spot" by electron impact, or both. The mass spectrometer showed an increase in the partial pressures of CO, H, and methane during the pressure

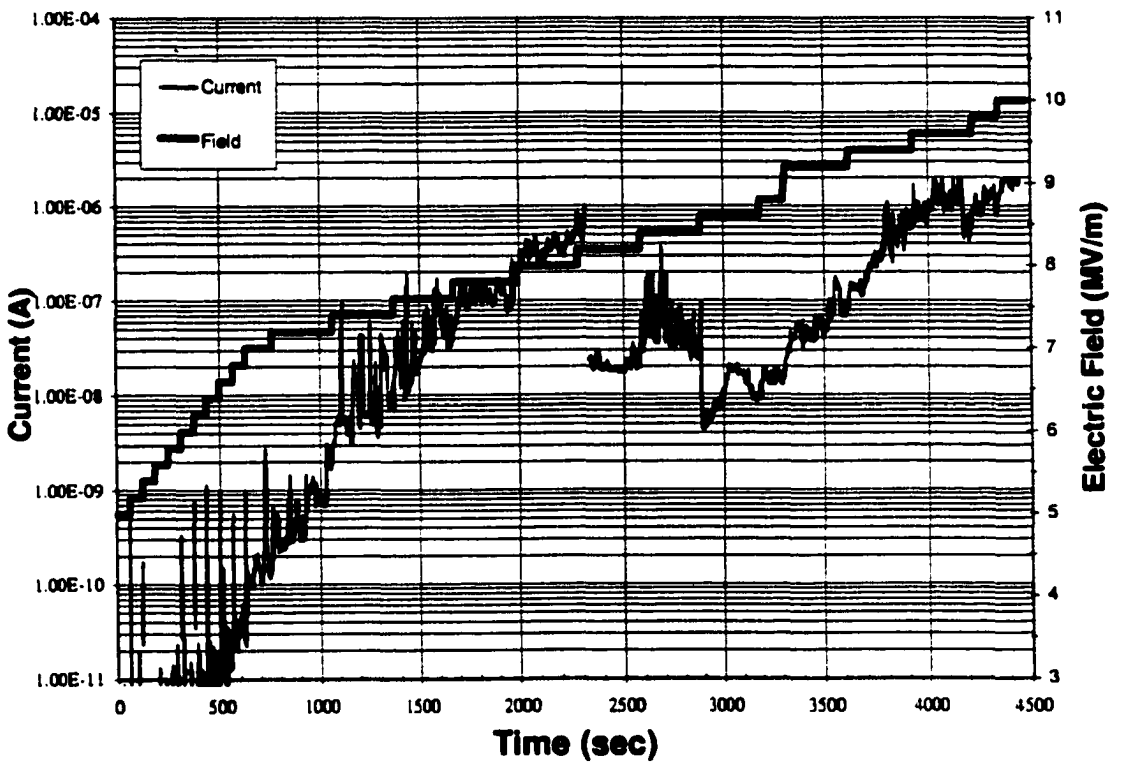

Figure 5.6: IV curve for unpolished sample. Stair-step curve is the applied field data. Lighter curve shows the measured current. Spikes at low field strengths are associated with capacitive charge of the gap with each voltage increase.

increase. The mass spectrometer was not operated for most of the voltage ramps, as it was discovered that electrons from the spectrometer ionizer induced almost 3 nA of current on the electrode system. Several "conditioning" events, or rapid decreases in current, were observed during the voltage ramp. Note the pressure bursts associated with the conditioning at t=2250 seconds and t=2750 seconds. Current during some higher field plateaus increased over the time of the constant field application. A gradual pressure rise was associated with this behavior, indicating a possible feed-back effect between current and pressure.

Figure 5.8 shows current and voltage data from a sample polished to one micron diamond paste (rms roughness 0.01μm). This particular sample gave a turn-on field of about 9 MV/m. As the voltage ramp continued, the emission became unstable at t=2150 seconds, after which the current dropped to a level below the noise of the picoammeter. This, again, is evidence of the conditioning effect. This emitter may have been a dust particle or loosely bound inclusion that was removed by the applied field, or the emitter was destroyed by a microdischarge. The exact mechanism can not be known, since the sampling rate of the picoammeter is too slow (1 Hz) to have recorded a transient pulse of current associated with a microdischarge. The current at the final field of 10 MV/m was below the noise level. Figure 5.9 shows the total pressure curve taken during the voltage application. The pressure data show a spike associated with the conditioning event.

A summary of the performance of several electrodes, polished and unpolished, is shown in Table 5.1. The applied fields for this initial investigation were between 3 and 10 MV/m. From the results, the polishing of the surfaces is clearly beneficial in reducing the turn-on voltage, and lowering the emitted current at the final applied field.

Some polished electrodes were tested under higher field conditions. The gap was duced to 2.5 mm for a maximum field strength of 20 MV/m. The results, with data from npolished electrode at lower field strength, are summarized in fig. 5.10. Note that this of current as a function of field, rather than a function of time. Current data from were averaged over the plateau time, and a standard deviation was computed

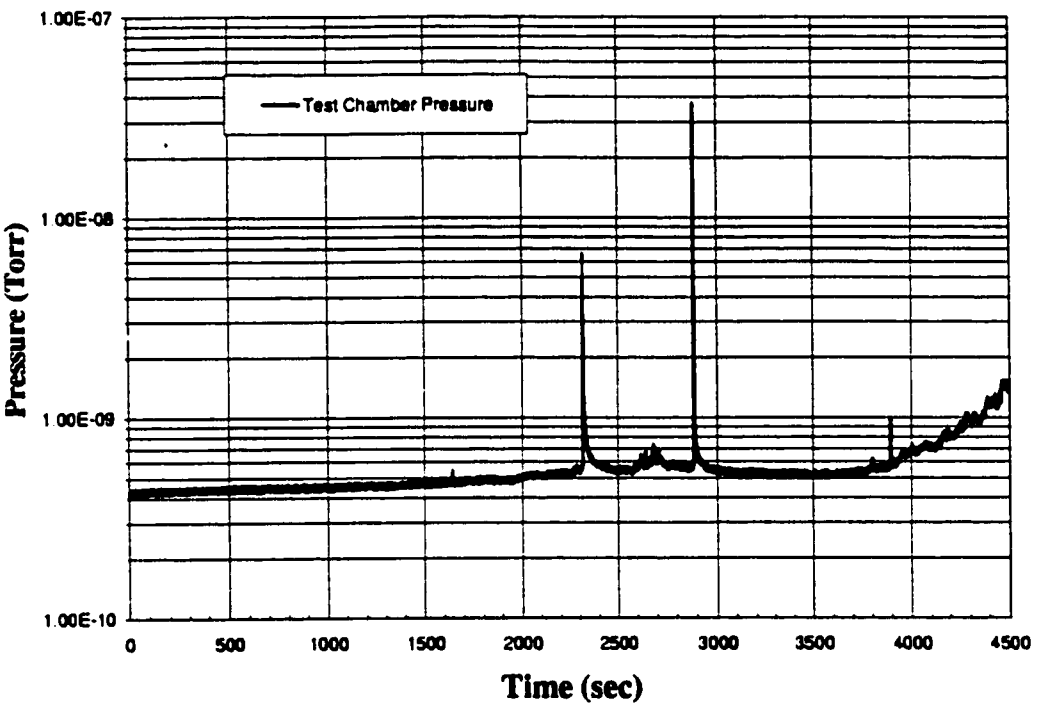

Figure 5.7: Pressure curve for unpolished sample 4. See figure 5.6 for IV data.

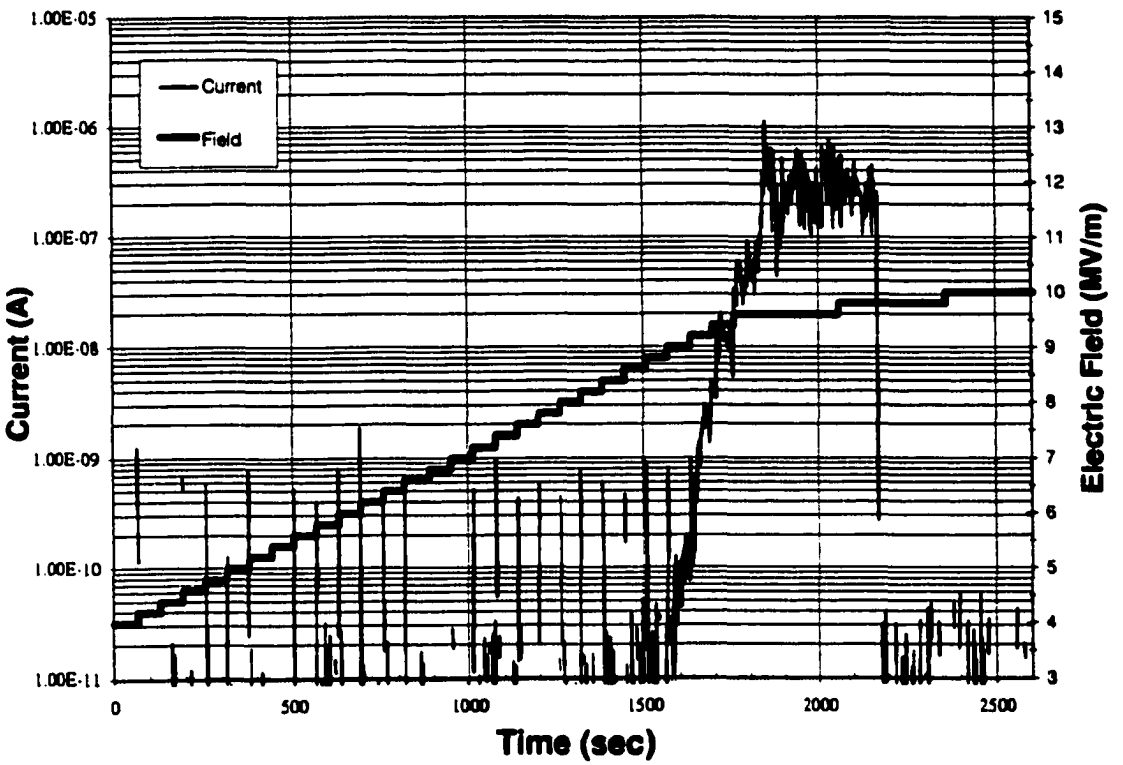

Figure 5.8: IV curve for highly polished sample. Stair-step curve is the applied field data. Lighter curve shows the measured current. Spikes at low field strengths are associated with capacitive charging of the gap with each voltage increase.

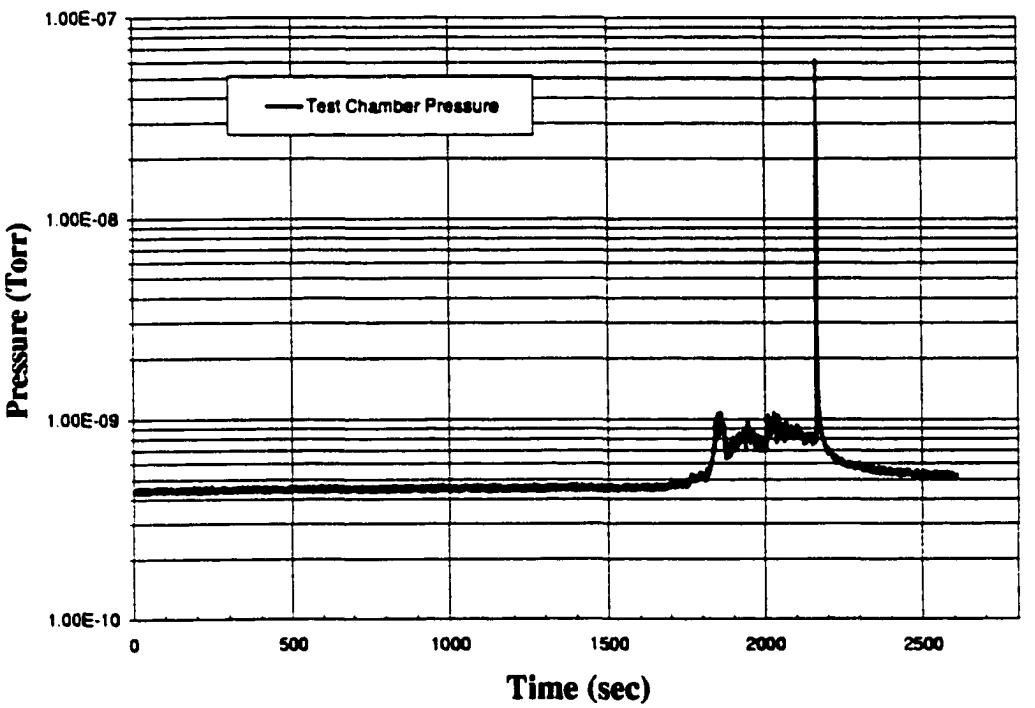

Figure 5.9: Pressure curve for a highly polished sample. See figure 5.8 for IV data.

Electrode	Finish	E_{on} (MV/m)	I_{max}	I(10 MV/m)
0101	As machined	< 5	10.0 μA	2.29 μA
0104	As machined	7	1.58μ A	1.58μ A
0102	Polished	†	<0.1 nA	<0.1 nA
0105	Polished	9.2	0.5μ A	<0.1 nA
0106	Polished	†	<0.1 nA	<0.1 nA

Table 5.1: Summary of results from untreated stainless steel electrodes to field strengths of 10 MV/m. †Indicates no "turn-on" field associated with this experiment.

for each data set. The standard deviation of the current during the plateau is represented by the error bars at each point. It is interesting to note the differences in the dynamic emission behavior, not only between electrodes of dissimilar surface finish, but also between electrodes of similar surface finish. These results indicate the possibility of more than one type of emission mechanism occuring on the samples. For example, the polished sample 0206 was already active at the start of the 10 to 20 MV/m run, and the emission current was extremely stable. Sample 0202, also polished, gave a higher turn-on field, and showed very erratic emission behavior.

5.6 Nitrogen Implanted Electrodes

Electrodes were implanted with the W & M PSII system at 30 kV to a dose of $10^{17}/cm^2$. One sample was polished to 1 micron diamond paste, (0.01 μm rms roughness) and the second sample polished to only 9 micron (0.07 μm rms roughness). Two more samples polished similarly were implanted by beam implantation to the same dose at energies of 50 kV by an outside vendor (Implant Sciences). An XPS spectrum of one of the samples after the system bake is shown in Fig. 5.11.

The spectrum from the implanted electrodes differs from that of the non-implanted electrodes for the following reasons. The Auger peaks associated with the nickel in the stainless steel are around 410 eV and 393 eV. The main spectral peak of nitrogen is near 400 eV. Peak discrimination becomes somewhat difficult because the nickel Auger (X-AES)

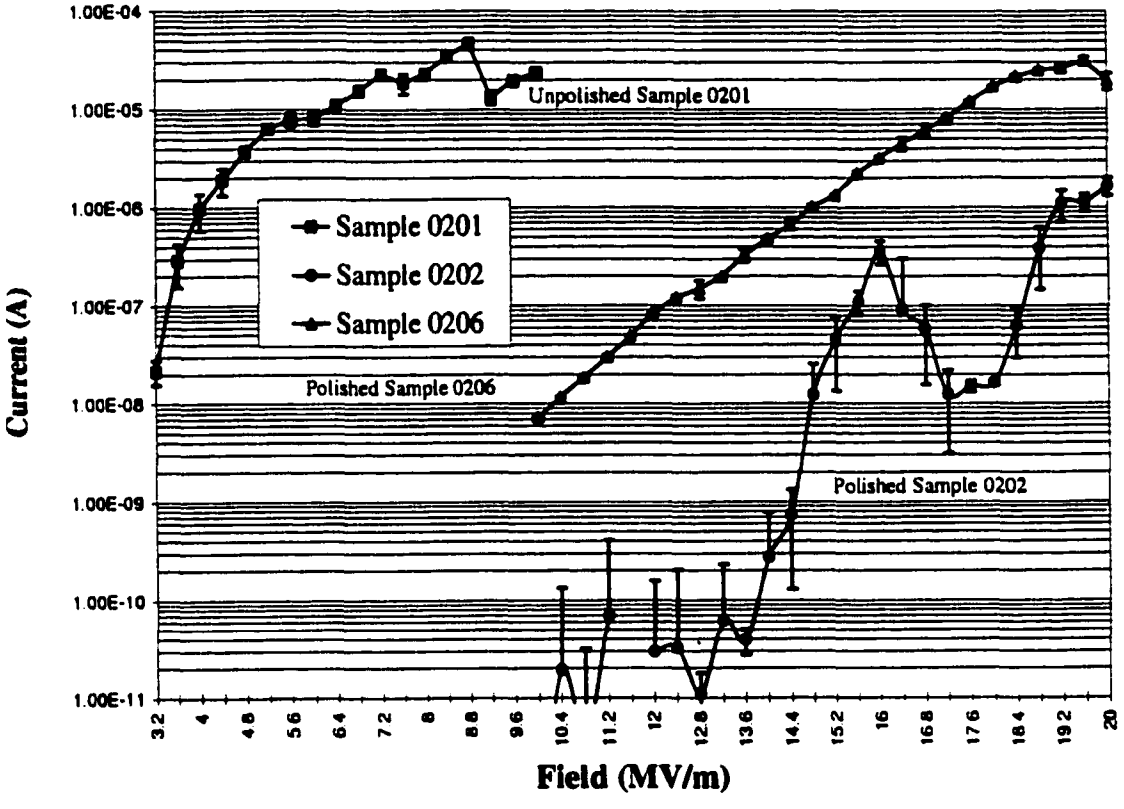

Figure 5.10: Summary of data taken for 2 polished electrodes and 1 unpolished electrode at high fields. Data points represent the average current for each plateau, and the error bars represent the standard deviation from each average.

peaks overlap the nitrogen peak. This problem can be alleviated by selecting the aluminum X-ray source (Al K_α = 1486.6 eV). The binding energy is calculated by the spectrometer as $KE = h\nu - BE - \phi_s$, where $h\nu$ is the energy of the photon, BE is the binding energy of the orbital from which the detected electron originated, and ϕ_s is the spectrometer work function. As the energy of an Auger electron is insensitive to the incident photon energy (assuming, of course, the energy of the incident photon was sufficient to cause the Auger transition), the Auger peaks are shifted by an amount 1486.6eV - 1253.6 = 233.0 eV with the selection of the aluminum source. The nickel Auger line is shifted, then, far from the main nitrogen peak.

The samples show a high level of oxygen and carbon concentration. This may be due to a temporary loss of power to one of the vacuum pumps during the bake. This would account for the large carbon and oxygen peaks, as the pump speed during the bake was compromised, and gases were not adequately pumped from the system. The final pressure in the system was 1×10^{-9} Torr. Partial pressures in the system are shown in Fig. 5.12.

Other contaminants present on the two PSII samples are Zn and Cu. The copper was most likely a result of the copper feedthroughs supporting the filament in the PSII chamber. Ion bombardment of these feedthroughs may have sputtered copper into the plasma. The source of the zinc is not known at this time. Neither component is present in manufactured stainless steel.

IV curves for the four nitrogen implanted samples are shown in Figs. 5.13, 5.14, 5.15, and 5.16. Fields as high as 20 MV/m were applied to all four samples, with minimal emission current. No pressure rise was associated with any of these tests.

The contamination layer may have played a part in suppressing the emission from the electrodes. In order to evaluate the effects of the hydrocarbon layer, the 9 micron polished sample treated in the PSII was sputter cleaned for 10 minutes with a 5 kV argon ion beam at 2 $\mu A/cm^2$. The sputter rate for iron (stainless steel is about 74% iron) is about 100 Angstroms per minute for a 1 mA/cm^2 5 kV beam. A 2 $\mu A/cm^2$ ion current

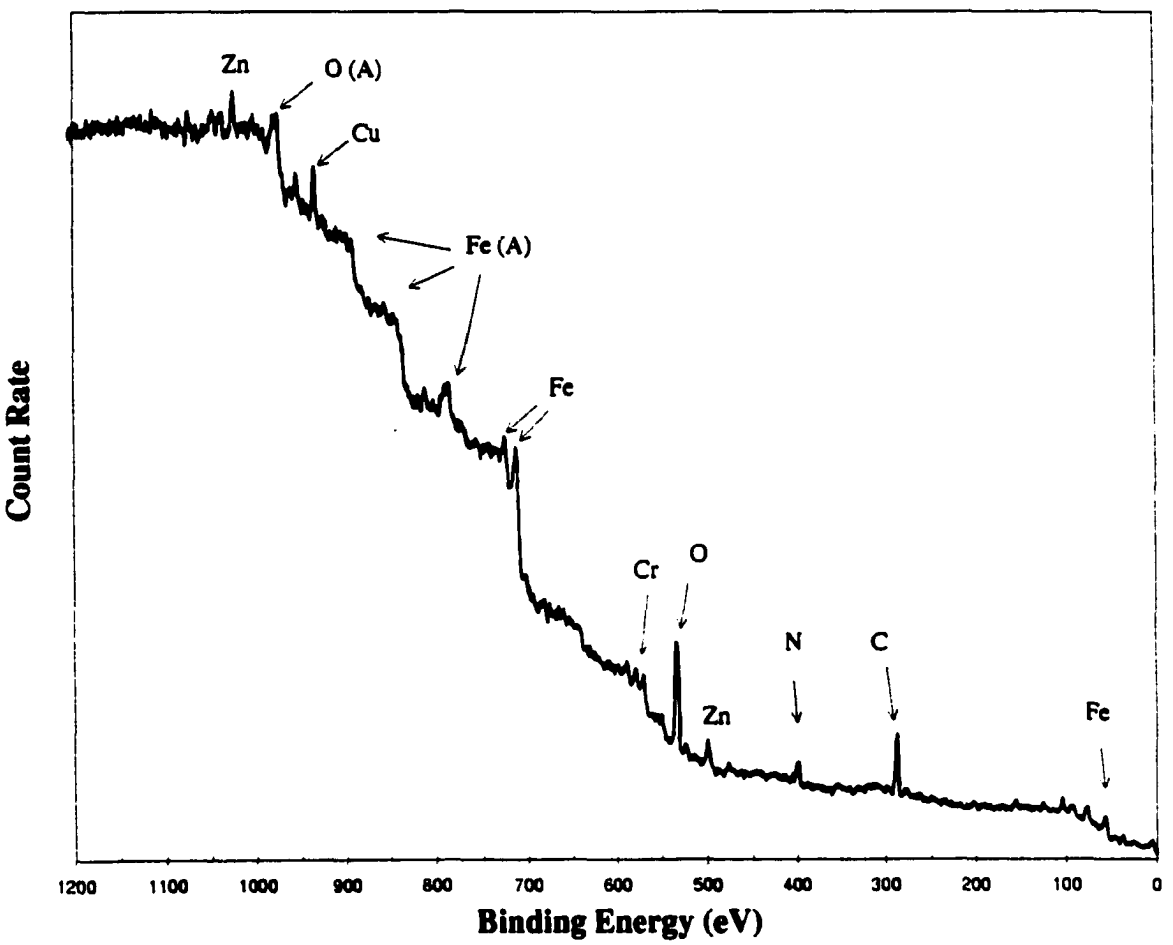

Figure 5.11: XPS of implanted electrode after 24 hour, 150 °C bake of the system. High level of oxygen and carbon are the result of partial loss of pumping speed during the bake process.

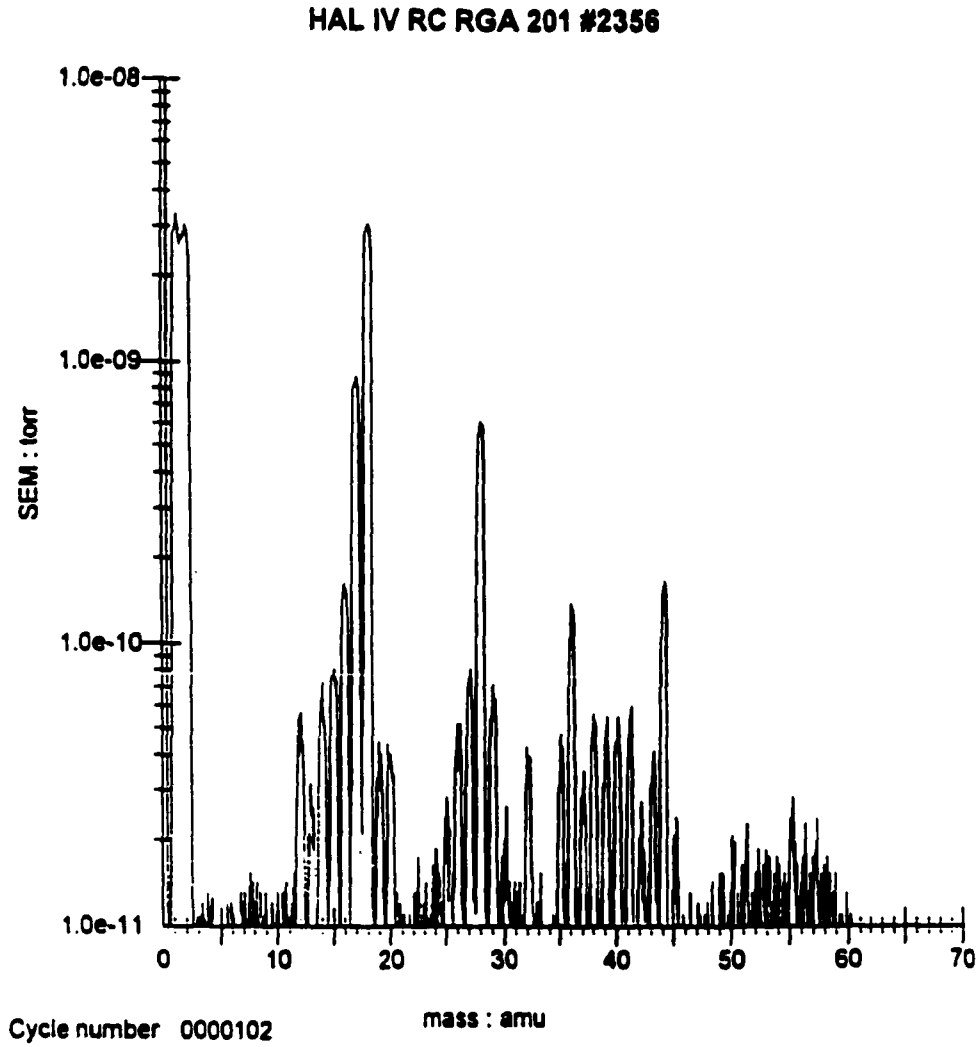

Figure 5.12: Background gas spectrum during IV curves for nitrogen implanted electrodes. Main constituents are H_2 (mass 2), H_2O, (mass 18), CO (mass 28), and CO_2 (mass 44).

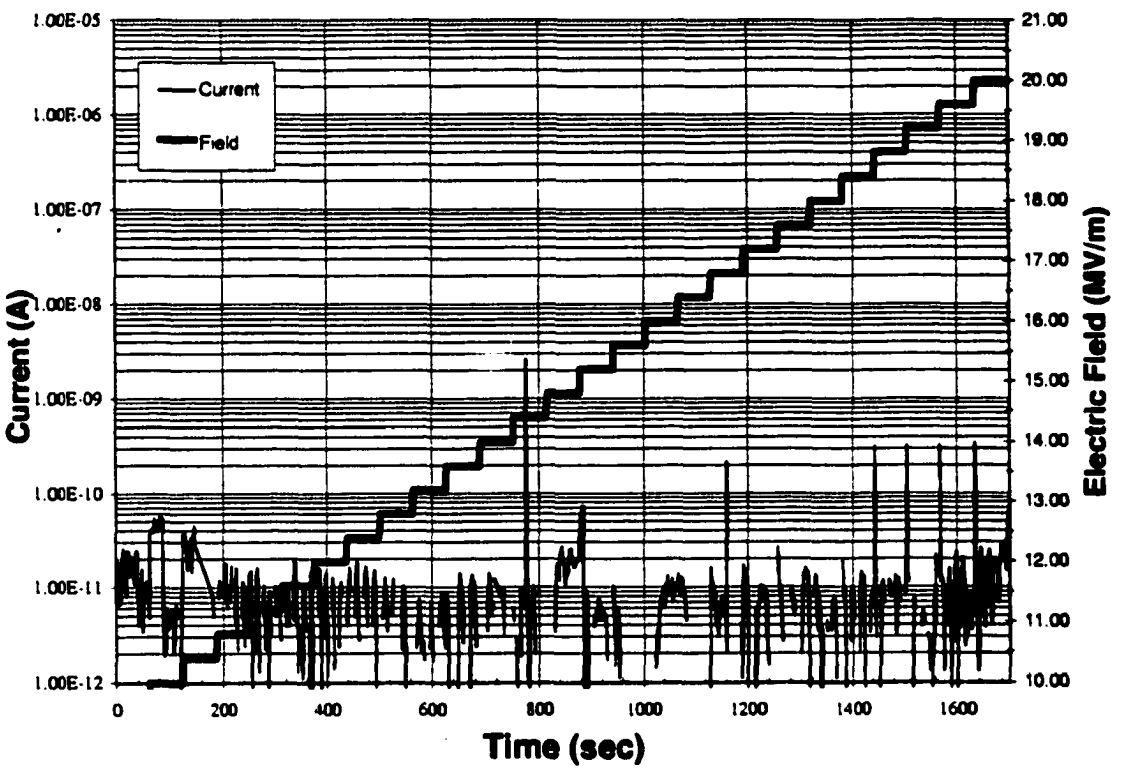

Figure 5.13: IV curve for 1 μm polished sample implanted to dose of $10^{17}/cm^2$ at 30 kV pulse voltage.

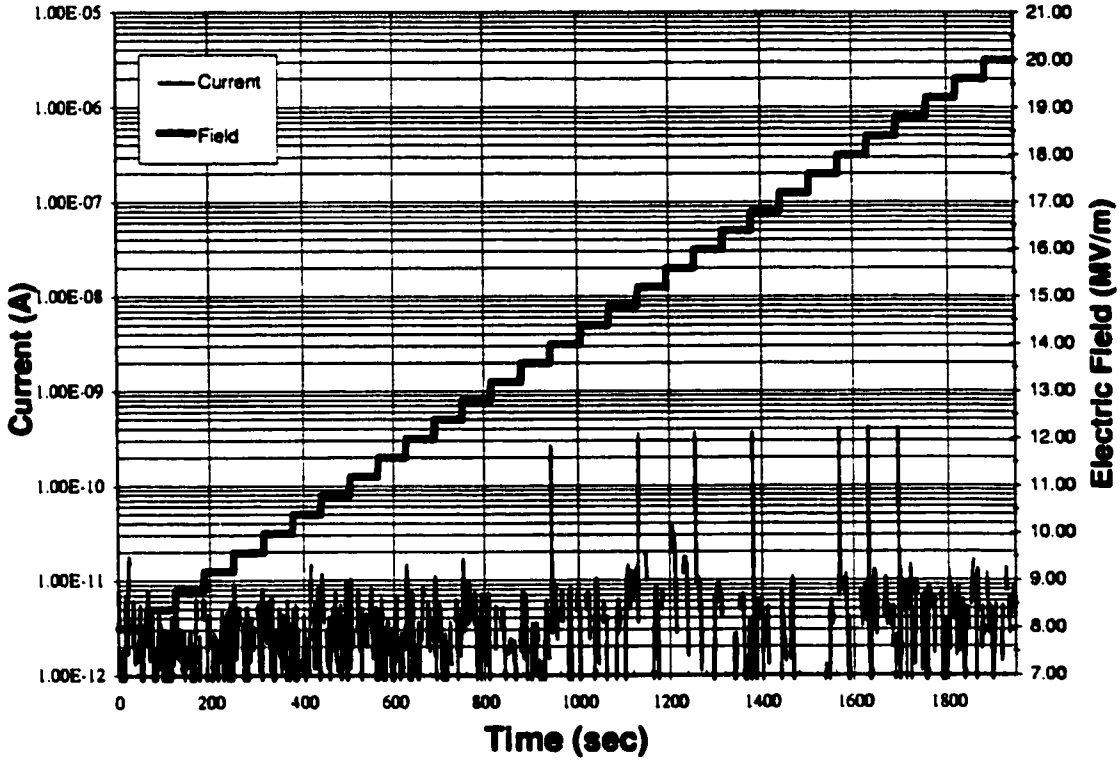

Figure 5.14: IV curve for a 9 μm polished sample implanted to dose of $10^{17}/cm^2$ at 30 kV pulse voltage.

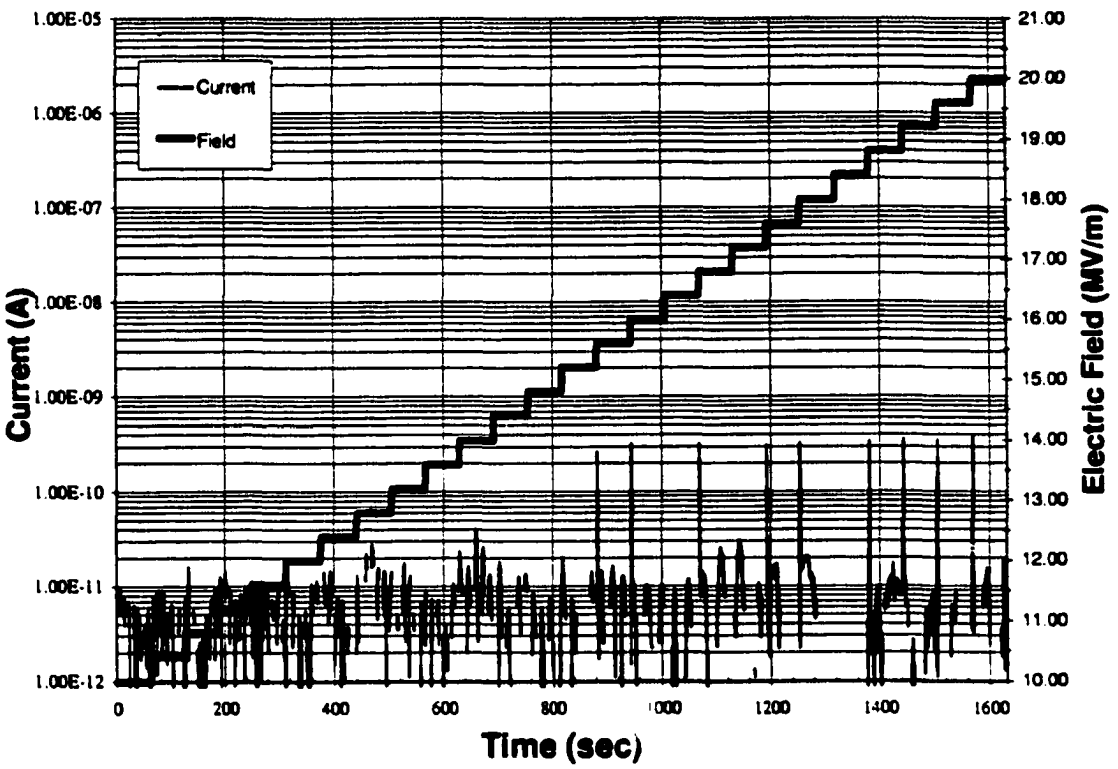

Figure 5.15: IV curve for 1μm polished sample. Sample was beam implanted with nitrogen to dose of $10^{17}/cm^2$ at 50 kV acceleration voltage.

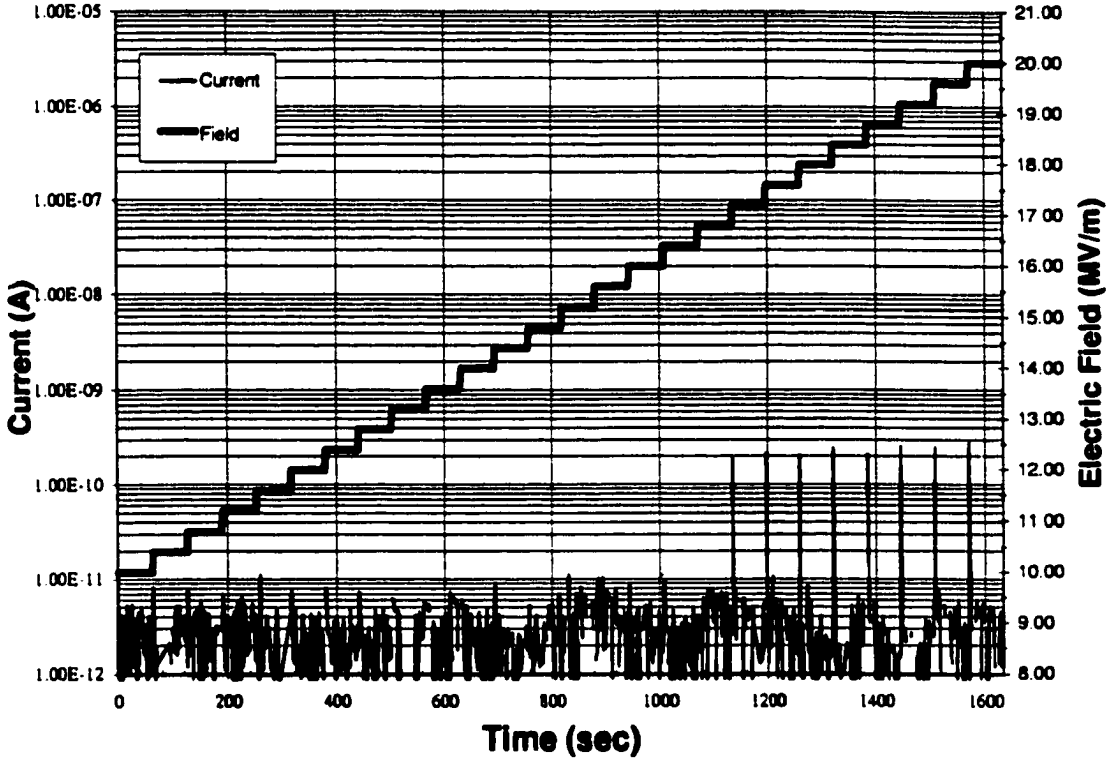

Figure 5.16: IV curve for 9 μm polished sample. Electrode was beam implanted to a dose was $10^{17}/cm^2$ at 50 kV acceleration voltage.

for 10 minutes would result in about 20 Angstroms of material removed. Figure 5.17 shows XPS analysis of the cleaned sample. Note the reduction of the carbon peak and the Zn peaks, although copper is still present. If copper was present in the PSII plasma, it would have been implanted also. The zinc was removed by the argon sputter clean, so it may have originated from the cleaning steps. Note also the nitrogen peak at 400 eV binding energy. Figure 5.18 shows the characteristic IV curve for the clean sample. This result was consistent with those from the contaminated samples.

5.7 Alternative Surface Treatments

Two additional surface treatments were evaluated for their pre-breakdown electron emission behavior. These processes were characterized by the same parameters as the other electrodes in the experiments.

5.7.1 Electron Beam Treatment

Results from Batrakov *et al* [23] indicated that treating the surface of the electrodes with a high-current, low energy electron beam reduced the emission current at a given field. With this motivation, an electrode was treated similarly at Jefferson Labs. The IV curve and pressure trend for this electrode is shown in Figs. 5.19 and 5.20.

Emission current from the e-beam treated electrode resulted in a high background pressure increase. How this gas desorption compares with the desorption of some polished electrodes at a few select currents is shown in Table 5.2.

Sample	Treatment	Current μA	Pressure Increase	Field (MV/m)
0213	E-beam	3.35	728%	20
0205	Polish	3.54	<1%	20
0202	Polish	19.5	<1%	20

Table 5.2: Total background pressure increase for an electron beam treated electrode and two highly polished electrodes.

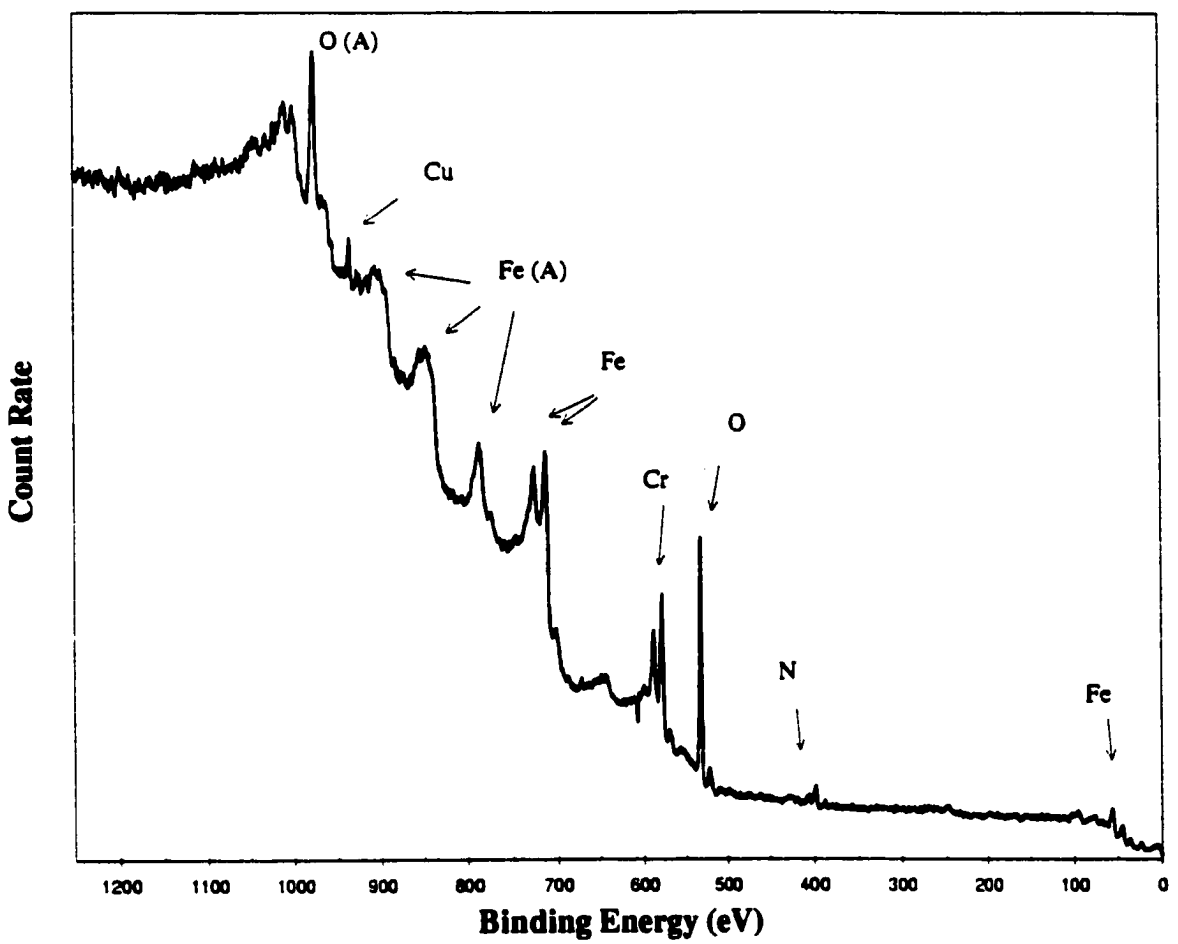

Figure 5.17: XPS data of "clean" electrode. The sample was sputter cleaned for 10 minutes with a 5 kV Argon ion beam at 2 $\mu A/cm^2$.

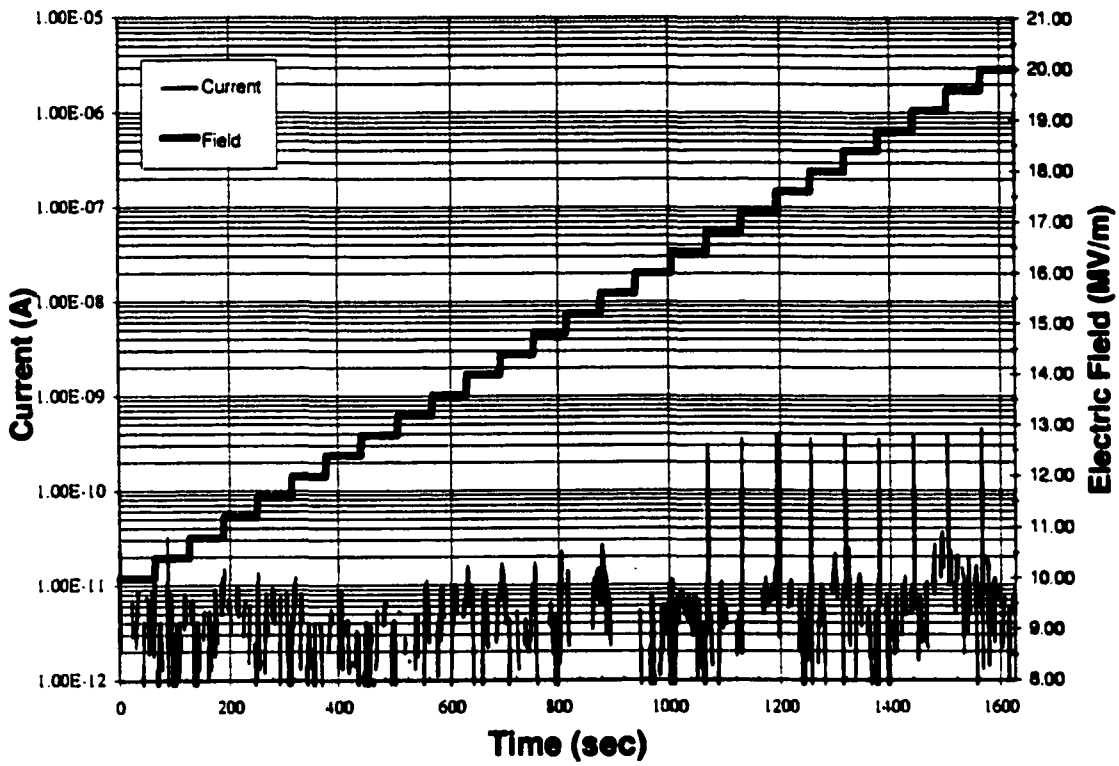

Figure 5.18: IV curve for 9 μm polished sample implanted to dose of $10^{17}/cm^2$ at 30 kV pulse voltage. Sample was sputter cleaned prior to voltage application. See XPS in Fig. 5.17.

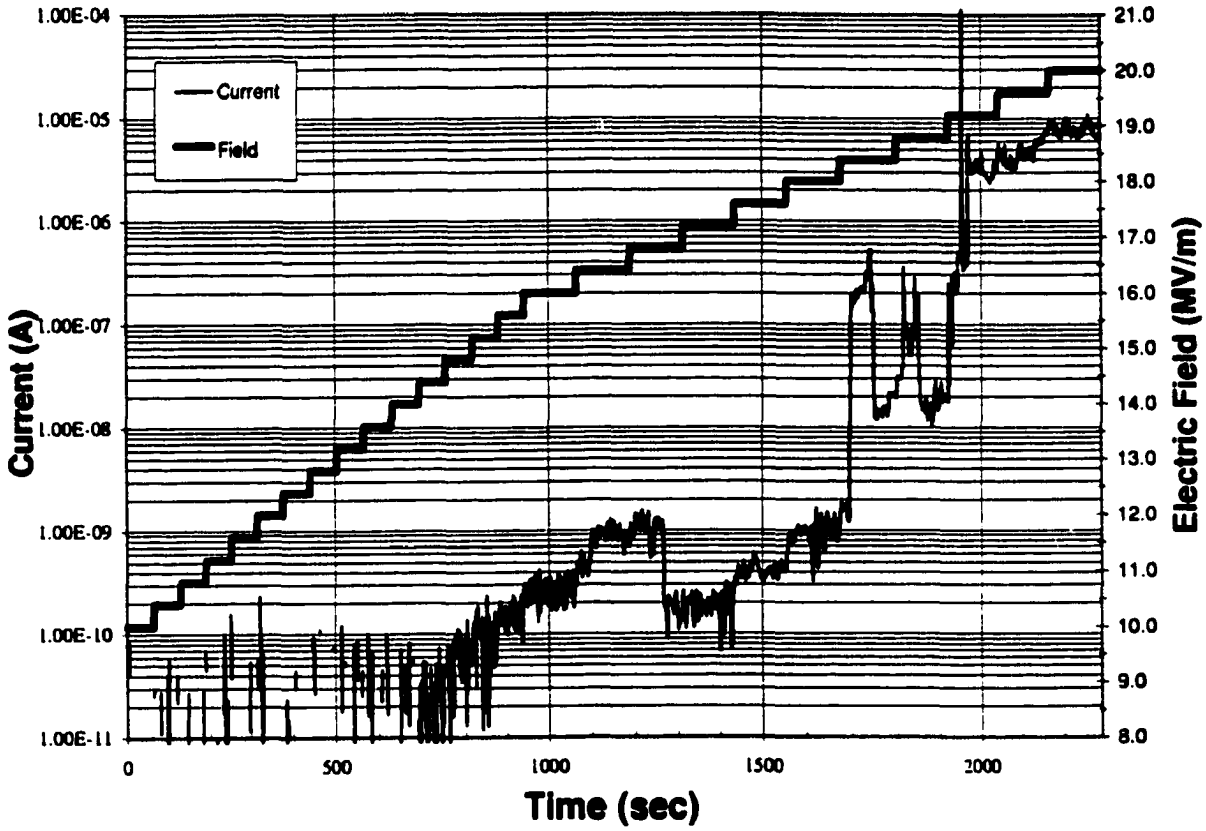

Figure 5.19: IV curve for e-beam treated sample.

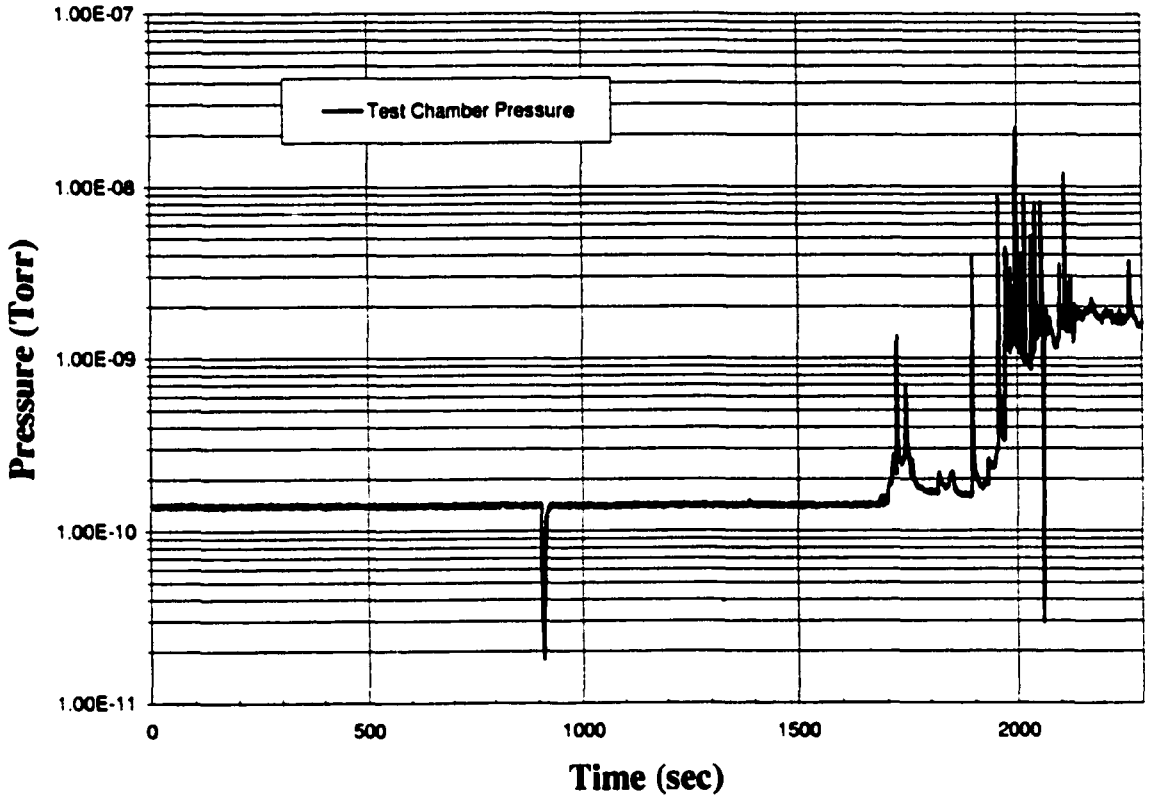

Figure 5.20: Pressure trend for e-beam treated sample during field application.

The source of the gas may be electron stimulated desorption from the anode, or thermally desorbed species from the emitter site. It is difficult to draw a conclusion concerning the source of the desorbed gases from these data. The number of emission sites may differ between the samples shown in Table 5.2, therefore the power density may differ. There may be one intense "beam" of electron emission, or several smaller ones. However, the electron beam welder used to process the electrodes is not a high vacuum instrument ($\sim 10^{-4}$ to 10^{-5} Torr). The melted top surface layer ($\sim 25\ \mu$m) may have trapped gases. Desorption may have occurred near a heated emitter site. However, further experiments are needed to confirm this.

5.7.2 Thin Film Coatings

A commercial thin film[2] was evaluated for electron emission suppression in the ESCALab test platform. Samples polished to one micron diamond, and with no polishing, were coated and tested. Figure 5.21 shows results from a polished, coated electrode. This sample showed some turn-on events, with a current at 20 MV/m of about 0.3 nA. Results from an unpolished, coated electrode is shown in Figure 5.22. The ability of the coating to suppress emission by six orders of magnitude as compared to an unpolished, uncoated electrode is remarkable. Indeed, this unpolished, coated sample, out-performed its polished counterpart.

5.8 Conclusion of Results

Characteristic IV curves have been obtained for stainless steel electrodes processed by several methods. The results of all experiments are summarized in Table 5.3.

- Polishing, a standard practice in the high voltage field, gave consistent results up to field of about 10 MV/m. With the application of higher fields, up to 20 MV/m, currents on the order of several microamps were observed.

[2] *Highvolt A*, FM Technologies, Alexandria, VA

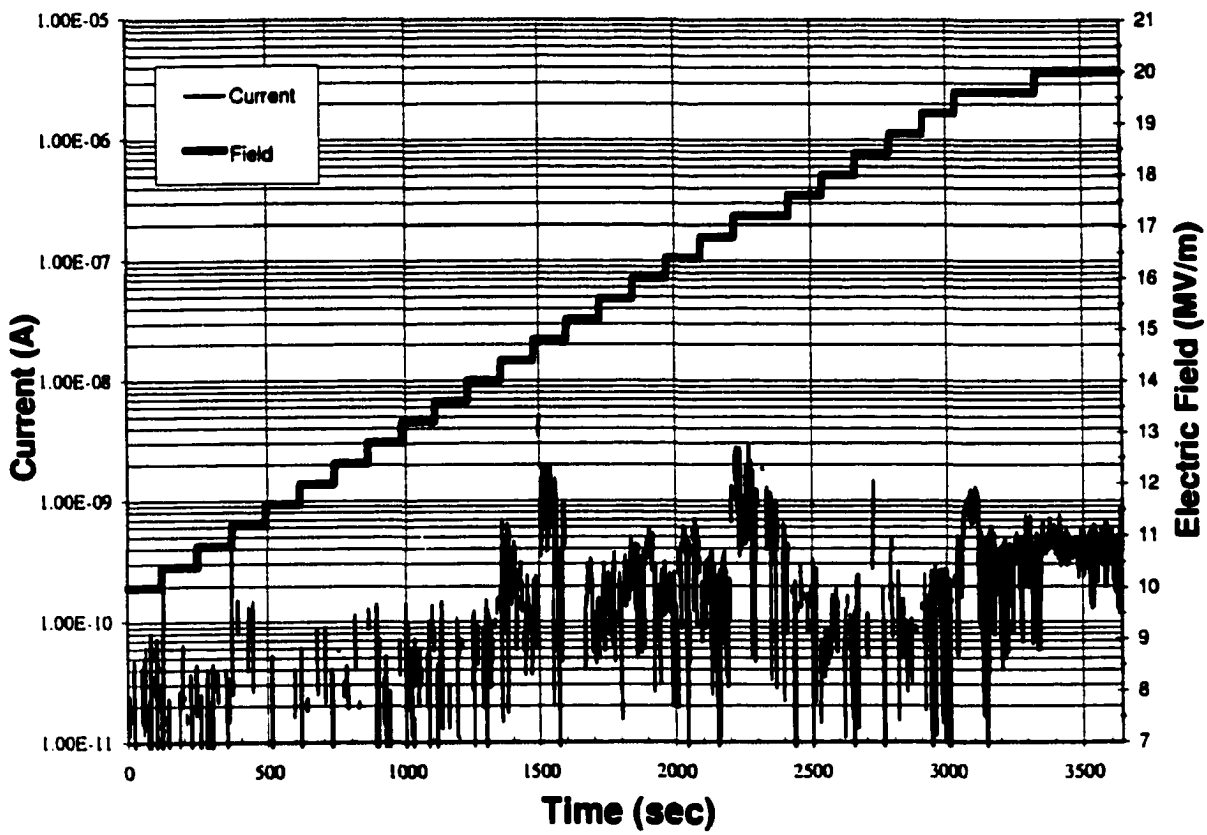

Figure 5.21: IV curve for coated, polished electrode.

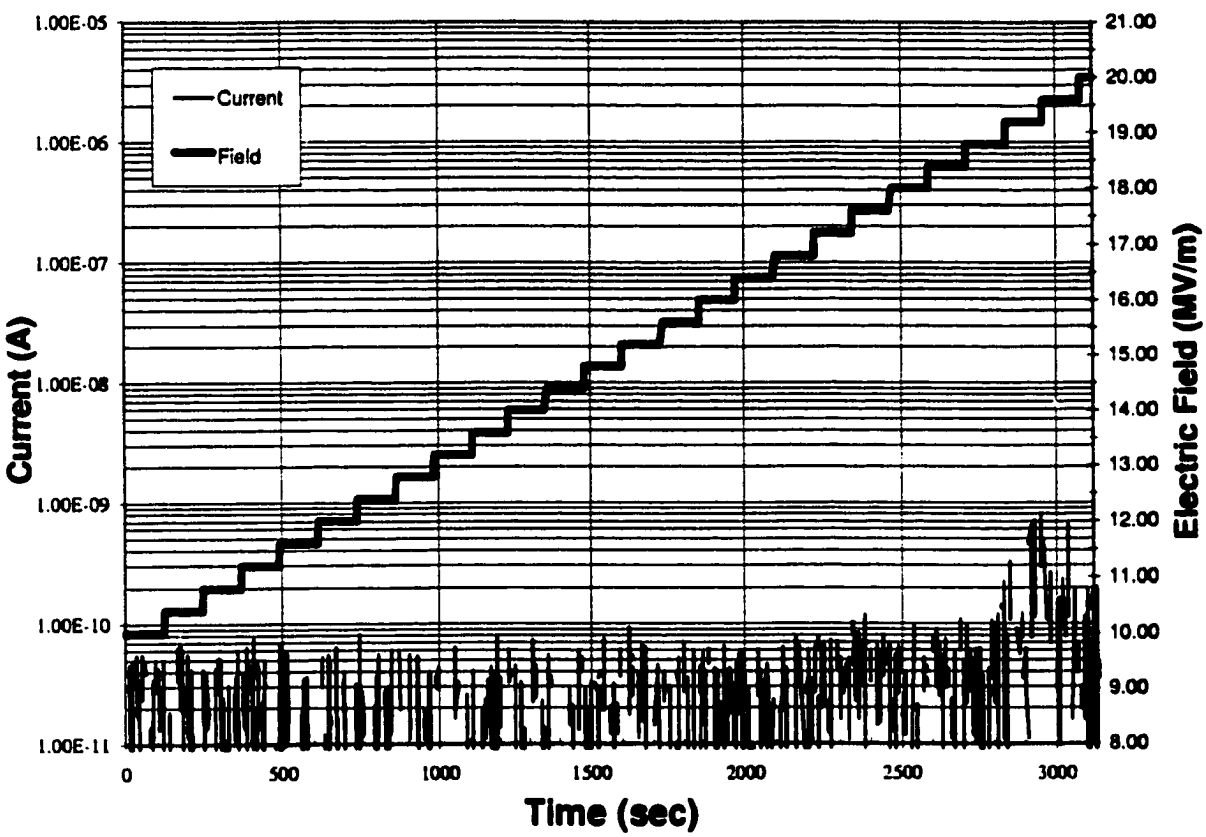

Figure 5.22: IV curve for a coated, unpolished electrode.

Electrode	Finish	E^1_{max}	E^1_{on}	I_{max}	I at E_{max}
0101	Unpolished	10	< 5	10.0 μA	2.29 μA
0104	Unpolished	10	7	1.58μA	1.58 μA
0201	Unpolished	10	<3.2	4.50 μA	2.25 μA
0102	Polished	10	†	‡	‡
0105	Polished	10	9.2	0.51μA	‡
0106	Polished	10	†	‡	‡
0202	Polished	20	14	1.52 μA	1.52 μA
0206	Polished	20	8	20.0 μA	20.0 μA
0204	Polished, Coated	20	20	<1 nA	<0.3 nA
0205	Polished, Coated	20	†	‡	‡
0207	Polished, Coated	20	†	‡	‡
0209	Unpolished, Coated	20	†	‡	‡
0213	E-beam	20	15	7.02μA	7.02μA
0302	Polished, PSII	20	†	‡	‡
0311	Polished (9μm) PSII	20	†	‡	‡
0306	Polished, Ion Beam	20	†	‡	‡
0312	Polished (9μm) Ion Beam	20	†	‡	‡

Table 5.3: Summary of results from treated and untreated stainless steel electrodes in this report. [1]Fields given in MV/m. †Indicates current did not rise above 0.1 nA during the entire field application (i.e. no "turn-on" of the current). ‡Indicates current less than 0.1 nA.

- An electron beam treated electrode showed little emission current until the field reached 13 MV/m. An order of magnitude pressure increase was observed during emission from this electrode.
- Electrodes coated with a commercial thin film from FM Technologies, Inc. was showed low levels of emitted current at fields as high as 20 MV/m. One polished, coated electrode showed very low current during the voltage run.
- Nitrogen implanted electrodes processed with PSII and beam implantation resulted in low levels of field emission at fields as high as 20 MV/m.

Further studies are required to quantify the effects of the implantation. Variations of dose, energy, and species would help elucidate the mechanisms. Also, testing of larger-area electrodes at higher voltages is crucial to the transfer of any emission suppression techniques to systems such as the electrons guns at Jefferson Labs. These results, and suggestions for further research, will be discussed in Chapter 6.

Chapter 6

Discussion and Future Work

This chapter draws conclusions about the W & M PSII, and about the benefits of PSII as a surface process technique for treating high voltage electrodes. First, improvements to the W & M PSII system are suggested. Then, suggestions are made to further the understanding of the electronic and physical structure of an implanted surface in terms of anomalous emission.

6.1 PSII

The William and Mary PSII showed promise as an ion implanter. Several modifacations are suggested to increase its operational reliability. These are outlined in the following sections.

6.1.1 W & M PSII Upgrades

High Voltage Power Supply

Implant voltages were limited to 30 kV due to a problem with the capacitor charging power supply. Charge voltages above 3kV (the 10:1 step up transformer gave the 30 kV pulse voltage) would occasionally cause the power supply to shut down during an implantation experiment due to an overvoltage fault protection. The cause of this fault is not certain, but it was determined that the fault occured just after the firing of the thyratron. A solution

was offered by the makers of the power supply (Kaiser). The interface to the power supply includes an "enable" pin. Once grounded, the output of the power supply is enabled, and the power supply will charge the capacitors. If the pin is not grounded, the power supply is disabled. With this interface, the supply can be deactivated just prior to the pulse, and reactivated just after the pulse for charging of the capacitors. This will protect the power supply from any transient pulses or ground loops that may be causing the problem. The control of the enable pin is accomplished by the addition of a field effect transistor. The source of the transistor is attatched to the inhibit pin, the gate attached to a DC source, and the drain attached to ground. For charging the capacitors, 5 volts DC is applied to the transistor. The source of the transistor will be pulled to ground, and the supply enabled. Just before the thyratron is triggered, the transistor gate is dropped to 0 volts, and the source will no longer be grounded. The power supply will be inhibited and protected during the pulse. After the pulse, the enable pin is grounded for the next charge.

Plasma Production

Although the PFN was matched well enough with the plasma to produce a square shaped pulse with minimal reflected energy, the the plasma density was too low to match efficiently with the PFN. The average current per 30 kV pulse was only 2 amperes. The PFN was designed to deliver 3 amperes for a 30 kV pulse; this increases the process time. A higher plasma density is required to increase the average current per pulse. Because the charge per unit time crossing the sheath boundary is proportional to the density, an increase in density of a factor of 2 should be sufficient. The filament driven plasma was limited by the danger of tungsten contamination if the filament is operated at too high a temperature. This limits the amount of power that can be used for plasma production. The total power input to the plasma from the filament supply was about 100 Watts. An rf or microwave driven plasma would be appropriate for the implanter, as these methods are electrode-less and have been proven in other systems [32, 48]. Microwave and rf coupling to the plasma

can provide greater power input without the worry of contamination. The chamber's large top plate would accomodate an rf flat coil design, or an electron-cyclotron-resonance (ECR) microwave source.

Insulation

Minimizing arcing activity at pulse voltages above 30 kV in the PSII chamber was a challenge. A great deal of arc formation occured at the triple-point (the junction where the quartz stand-offs, metal, and vacuum contact). When an arc forms, the voltage pulse drops to just a few volts, and the current rises to many tens of amps. The maximum average current rating for the thryatron can be surpassed, should the arcing continue. This will result in permanent damage to the thyratron. To reduce the arc formation at the triple point, a new alumina stand-off with stainless steel triple point protectors was designed (the design was not put into service, however). Also, the arc formation is exacerbated by the presence of the plasma. A quartz tube fitted over the alumina standoff will help keep the plasma away from the insulator.

6.1.2 Conclusion - PSII

Based on this work, some modifications will improve the capabilities of the William and Mary PSII system. However, initial operations were successful. Future implant work is possible with the suggested modifications. The PFN is nominally a 100 kV, 30 pulse unit. The system has been operated at voltages as high as 50 kV (prior to observing the problem with the power supply). With the new alumina high voltage stand-off and modifications to the power supply, higher voltage will be possible.

6.2 Field Emission Experiments

The following sections discuss the field emission results, and offers suggestions for future research. Suggestions are based on results from the current research and on past

results from the other works in literature discussed in chapter 2.

6.2.1 Disussion

Data from the emission experiments indicate that anomalous field emission from extended area electrodes is unpredictable in nature. Turn-on voltages varied by factors of 2 or more between similarly prepared electrodes. Distinct "modes" of current emission were also observed. This indicates the need for a larger set of experiments to confirm the effectiveness of implantation. The test chamber at Jefferson Laboratory, discussed in Chapter 4, will allow evaluation of the PSII process on higher voltage electrode systems.

These preliminary experiments indicated coatings and ion implantation were effective in reducing the emission current from stainless steel electrodes by several order of magnitude. However, the database is small, and more experiments are needed. Also, the data collected in this experiment provide a start in working towards a fundamental understanding of the mechanisms involved. Experiments can be proposed that would help to develop quantitative models. These are outlined in the next section.

6.2.2 Future Work

Past research investigations of anomalous field emission were reviewed in Chapter 2. It was shown that inclusions and foreign contaminants play a large role. Improving the ultimate breakdown voltage of a large-area electrode system would begin with the removal of foreign microparticles. This is not an impossible task, as the semiconductor industry routinely performs multi-step processing of 300 mm wafers with no introduction of particulates. Tenacious hydrocarbon layers, however, were shown in this work to remain after the 150 °C bake of the vacuum system. The effects of the layer, however, were not investigated thoroughly. Inclusions in the material are not so easily controlled as particulate contamination. The effects of PSII on these inclusions could be investigated by processing selectively contaminated surfaces that contained a high density of inclusions. To study the effects of

the ion impact on the crystalline structure, cross sectional transmission electron microscopy (TEM) would show the formation of amorphous layers and the amount of crystalline damage. An appropriate surface analytical method for the study of a modified oxide layer is Ultra-Violet Photoelectron Spectroscopy (UPS). UPS works on irradiating a surface with U-V light from a gas discharge lamp. Typically, low energy resonance lines from helium are used (He^{I}, 21.2 eV and He^{II}, 40.8 eV) with an energy width of a few millielectron volts. The energy from these lines is sufficient to emit electrons from the valence band only. UPS is used for the study of the electron band structure of metals, semiconductors, and alloys. If the effect of ion implantation is simply one of surface cleaning, experiments involving intentionally contaminated electrodes could be performed. If the geometric smoothing of emitter structures is involved, an experiment involving the implantation of field emitter arrays is suggested. Field emitter arrays are arrays of microscopic sharp tips used specifically for flat panel display technology. The tips have a very small radius of curvature, and, hence, a high field enhancement factor. These tips would provide for an excellent study of the effects of PSII on such structures. Also, a comparison could be made between the effects of plasma source and beam implantation using these emitter arrays.

Electrode material selection is reviewed by Latham [1, pages 48, 49]. Physically hard materials have been empirically accepted as "good" electrode materials. However, this rule can not be extended to all materials, as metals such as tungsten and beryllium, which are very hard, have not been shown to provide high voltage hold-off capabilities. Stainless steel and titanium are two materials that have been "accepted" in the field. A common attribute is the protective oxide layer on these materials. This layer increases the corrosion resistance of the material. Indeed, several similaries are observed between "pitting corrosion" and field emission sites. Pitting corrosion is a highly localised form of corrosion usually associated with a discontinuity in the material's passive oxide layer. The source of the corrosion pits can be an impurity inclusion within the structure which may cause a break in the oxide coating [56]. The anology between the cause of pitting corrosion and anomalous field

emission between extended area electrodes is clear. Perhaps a "good" electrode, or one that shows low levels of initial field emission, would also show no pitting corrosion. Similarly, perhaps a conditioned electrode would be resistant to pitting corrosion. If a relationship did exist, the large body of experimental evidance on pitting corrosion would aid in the physical understanding of the implantation effects of the electrodes. At was noted in Chapter 2, ion implantation is an effective technique for increasing the corrosion resistance of alloy systems.

Work Function Measurements

It is clear that the work function of the material, the amount of work needed to remove an electron from the bulk of the material to the vacuum with a zero final energy, is an important parameter in field emission investigations. There are several methods that measure the work function of a material. The simplest is with a vibrating Kelvin Probe [57]. The schematic for this type of work function probe is shown in Fig. 6.1.

A sample of known work function is placed near the surface of the sample to be investigated. The two electrodes are electrically connected, and charge will flow until the chemical potential of the electrons is uniform throughout the system. The amount of current that flows is $Q = C\Delta V$ where $\Delta V = \phi_R - \phi_S$. C is the capacitance of the electrodes, and ϕ_R and ϕ_S refer to the work function of the reference and sample electrodes, respectively. The reference electrode is vibrated at a frequency ω, changing the capacitance of the system. Current is induced in the circuit by the relation $I/C = dV/dt$. If the reference electrode is biased to V_{ext}, the voltage difference due to the different work functions can be nulled. The difference in work functions will then be equal to the external voltage, i.e. $\Delta V = -V_{\text{ext}}$.

6.2.3 Conclusion - Field Emission

Although a small database was collected on field emission experiments, the results of ion implanted electrodes are, at least, encouraging. However, it is important that the experiments be extended to the large area, high voltage test chamber at Jefferson Labs.

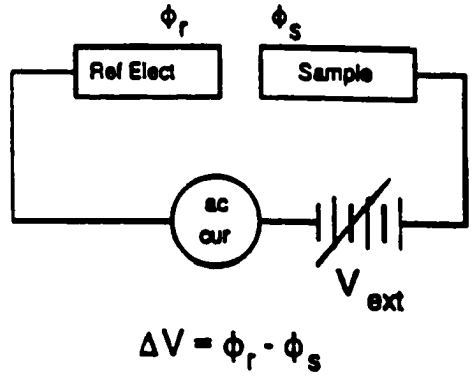

Figure 6.1: The Kelvin probe method for measureing the relative work function of materials. From John [56].

The non-linear relationship between breakdown field and gap voltage (the Total Voltage Effect discussed in Chapter 2) requires such extreme testing. Experiments in this chamber would provide confidence in the PSII process on a scale similar to that of the photoelectron guns.

To gain a physical understanding of the effects of ion implantation, a more accurate electronic model of the surface is needed. This is not a simple task on an oxide covered, polycrystalline, alloy such as stainless steel. UPS may provide some experimental guidance. Also, implantation of electrode materials with no natural oxide layer, or a conducting oxide layer, and their field emission behavior would lend to the understanding of the exact mechanisms involved.

The causes of anomalous emission from extended area electrodes are becoming clearer. A number of experiments that would aid in the understanding of the effects of ion implantation on these causes have been suggested.

6.3 Summary

The ability of the electron guns at Jefferson Labs to run reliably and consistently is crucial to the scientific programs in the main accelerator ring and the Free-Electron Laser project. The specified operational voltages are a reflection of what *can* be accomplished with current electrode materials and processing techniques. A reduction in the anomalous field emission activity between the electrodes in these systems, through the proper selection of novel materials and surface process techniques, will raise the operational voltages and fields in these electron guns, and provide stable, reliable operation. Plasma Source Ion Implantation has been shown in this work to reduce anamolous field emitted electrons in small area electrode systems, and physical mechanisms to explain the effects have been proposed. An experimental program based on the ground work in this thesis will further the understanding of field emission suppression and high voltage electrode performance from these modified surfaces.

Appendix A

The WKB Approximation

As field emission is a quantum mechanical phenomenon, it is appropriate to consider the probability of finding an electron on the vacuum side of a potential barrier. For a particle of mass m in a potential $V(x)$, the time-independent Schrödinger equation in one dimension is

$$-\frac{\hbar^2}{2m}\frac{d^2\Psi(x)}{dx^2} + V(x)\Psi(x) = E\Psi(x) \tag{A.1}$$

where $\hbar$ is Planck's constant divided by 2π, $\Psi(x)$ is the particle's wave function, and E is the total energy of the particle (kinetic plus potential). For a simple step potential barrier with a constant potential $V(x) = V_o$, the solution to Schrödinger's equation is:

$$\Psi = A\exp\frac{\pm ip_o x}{\hbar} \quad p_o = \sqrt{2m(E - V_o)} \tag{A.2}$$

where A is a constant. For potential functions that vary slowly with position, the Wentzel-Kramers-Brillouin, or WKB, method can be implemented. The derivation of the WKB approximation presented here follows B. H. Bransden and C. J. Joachain [58]. 'Slowly varying' means $V(x)$ changes slightly over the de Broglie wavelength

$$\lambda(x) = \frac{h}{p(x)} \tag{A.3}$$

where $p(x) = \sqrt{2m[E - V(x)]}$ is the classical momentum at the point x. In the classical limit, $\lambda(x)$ tends to zero. Therefore, the condition that the potential varies slightly with position implies the WKB approximation applies to a semi-classical approximation.

For a slowly varying potential function $V(x)$, one may assume a solution to eqn. A.1 of the form

$$\Psi = A\exp\frac{iS(x)}{\hbar} \tag{A.4}$$

Where $S(x)$ is a function to be determined. Inserting eqn. A.4 into eqn. A.1, one obtains

$$-\frac{i\hbar^2}{2m}\frac{d^2S(x)}{dx^2} + \frac{1}{2m}\left[\frac{dS(x)}{dx}\right]^2 + V(x) - E = 0 \tag{A.5}$$

Equation A.5 is a non-linear equation even more difficult to solve than equation A.1, and must be solved approximately. For a general potential function $V(x)$, $S(x)$ may be approximated as a series of powers of $\hbar$:

$$S = S_o(x) + \hbar S_1(x) + \frac{\hbar^2}{2}S_2(x) + \cdots \tag{A.6}$$

Eqn. A.6 can be inserted into eqn. A.1. To solve the resulting differential equation, the coefficient of each power of $\hbar$ in the equation is separately set equal to zero. A series of equations is then obtained (up to second order $\hbar$).

$$\frac{1}{2m}\left(\frac{dS_o(x)}{dx}\right)^2 + V - E = 0 \tag{A.7}$$

$$\frac{dS_o(x)}{dx}\frac{dS_1(x)}{dx} - \frac{i}{2}\frac{d^2S_o}{dx^2} = 0 \tag{A.8}$$

$$\frac{dS_o(x)}{dx}\frac{dS_2(x)}{dx} + \left[\frac{dS_1(x)}{dx}\right]^2 - i\frac{d^2S_o(x)}{dx^2} = 0 \tag{A.9}$$

We will begin in the classically allowed region where $E > V(x)$, and the momentum $p(x) = [2m(E - V(x))]^{1/2}$ is real. Equation A.7 can now be solved:

$$\frac{dS_o(x)}{dx} = \pm\sqrt{2m(E - V(x))} \tag{A.10}$$

to obtain

$$S_o(x) = \pm\int^x p(x')dx' \tag{A.11}$$

The arbitrary constant of integration has been omitted. $S_1(x)$ can be found by inserting the above equation into A.8 to obtain:

$$\frac{dS_1(x)}{dx} = \frac{i}{2}\frac{1}{dS_o(x)/dx} = \frac{i}{2}\frac{d}{dx}\ln\frac{dS_o(x)}{dx} \tag{A.12}$$

to arrive at

$$S_1(x) = \frac{i}{2}\ln p(x) \tag{A.13}$$

For clarity, the arbitrary constant of integration has been omitted. Using the above two equations in eqn. A.9, one has

$$S_2(x) = \frac{1}{2}m[p(x)]^{-3}\frac{dV(x)}{dx} - \frac{1}{4}m^2\int^x [p(x')]^{-5}\left[\frac{dV(x')}{dx'}\right]^2 dx' \tag{A.14}$$

It is clear that the above equation for $S_2(x)$ will be small when $dV(x)/dx$ is small, provided $E - V$ is not too close to zero. If all higher derivatives of $V(x)$ are small, then S_3, S_4, $\cdots$, are also small. Using only the first two terms $S_o(x)$ and $S_1(x)$, one obtains the *WKB approximation* in the classically allowed region:

$$\Psi(x) = A[p(x)]^{-1/2}\exp\left[\pm\int^x p(x')dx'\right], \quad E > V \tag{A.15}$$

A more general WKB solution is a linear combination of such approximations:

$$\Psi(x) = [p(x)]^{-1/2}\left\{A\exp\left[\frac{1}{\hbar}\int^x p(x')dx'\right] + B\exp\left[-\frac{1}{\hbar}\int^x p(x')dx'\right]\right\} \tag{A.16}$$

where A and B are arbitrary constants. The first half of the above expression represents a plane wave moving in the positive direction, and the second corresponds to a wave moving in the opposite direction.

So far, only the classically allowed case $E > V$ has been considered. For the classically forbidden region where $E < V$, the WKB approximation can still be obtained. In this region, the momentum $p(x) = \sqrt{2m[E-V]}$ becomes imaginary. Solving equations A.7 and A.8 for this case, one obtains the following equation for the WKB approximation:

$$\Psi(x) = A|p(x)|^{-1/2}\exp\left[\pm\frac{1}{\hbar}\int^x |p(x')|\,dx'\right] \quad E < V \tag{A.17}$$

where A is a constant. A general WKB solution is a linear combination of such approximations:

$$\Psi(x) = |[p(x)]|^{-1/2} \left\{ C \exp\left[-\frac{1}{\hbar} \int^{x} |p(x')|\, dx' \right] + D \exp\left[\frac{1}{\hbar} \int^{x} |p(x')|\, dx' \right] \right\} \quad E < V \tag{A.18}$$

where C and D are arbitrary constants.

The validity of the WKB approximation may be obtained by requiring that the third term in the expansion of $S(x)$ (A.6) be negligible, or that

$$\left| \frac{\hbar}{2} S_2(x) \right| << 1. \tag{A.19}$$

Using the expression for $S_2(x)$ (Eq. A.14) and the above equation, one may obtain

$$\left| \frac{\hbar m}{[2m(E - V(x))]^{3/2}} \frac{dV(x)}{dx} \right| << 1. \tag{A.20}$$

It is clear from the above equation that the WKB approximation breaks down where $E = V$, the so-called *classical turning point*. The WKB approximations for the two regions $E > V$ and $E < V$ are asymptotically valid, that is, they are only valid when used sufficiently far away from the turning point. Connection formulae have been obtained that join the two types of WKB approximations across the turning point. The derivations of these connection formulae are shown in greater detail in the Bransden and Joachain [58], and are only presented here. Two types of barriers, as shown in Fig. A.1, are considered. Fig. A.1a is a left hand barrier, where $V(x_1) = E$, $V(x) > E$ for $x < x_1$, and $V(x) < E$ or $x > x_1$. The classical turning point is at $x = x_1$. $p(x)$ is real in the region $x > x_1$, and the general WKB solution is given by eqn. A.16 with x_1 as the lower limit of integration. In the region $x < x_1$, $p(x)$ is imaginary, and the WKB solution is given by eqn. A.18, again with x_1 as the lower limit of integration. As shown in reference [58], when the approximate solution to A.18 is is a decaying exponential as $x \to -\infty$, the constant C is zero. It can then be shown that $iA = B = D(i\pi/4)$. The connection formula is then expressed as

$$|p(x)|^{1/2} \exp\left[\frac{1}{\hbar} \int_{x_1}^{x} |p(x')|\, dx' \right] \to 2[p(x)]^{-1/2} \cos\left[\frac{1}{\hbar} \int_{x_1}^{x} p(x')dx' - \frac{\pi}{4} \right] \tag{A.21}$$

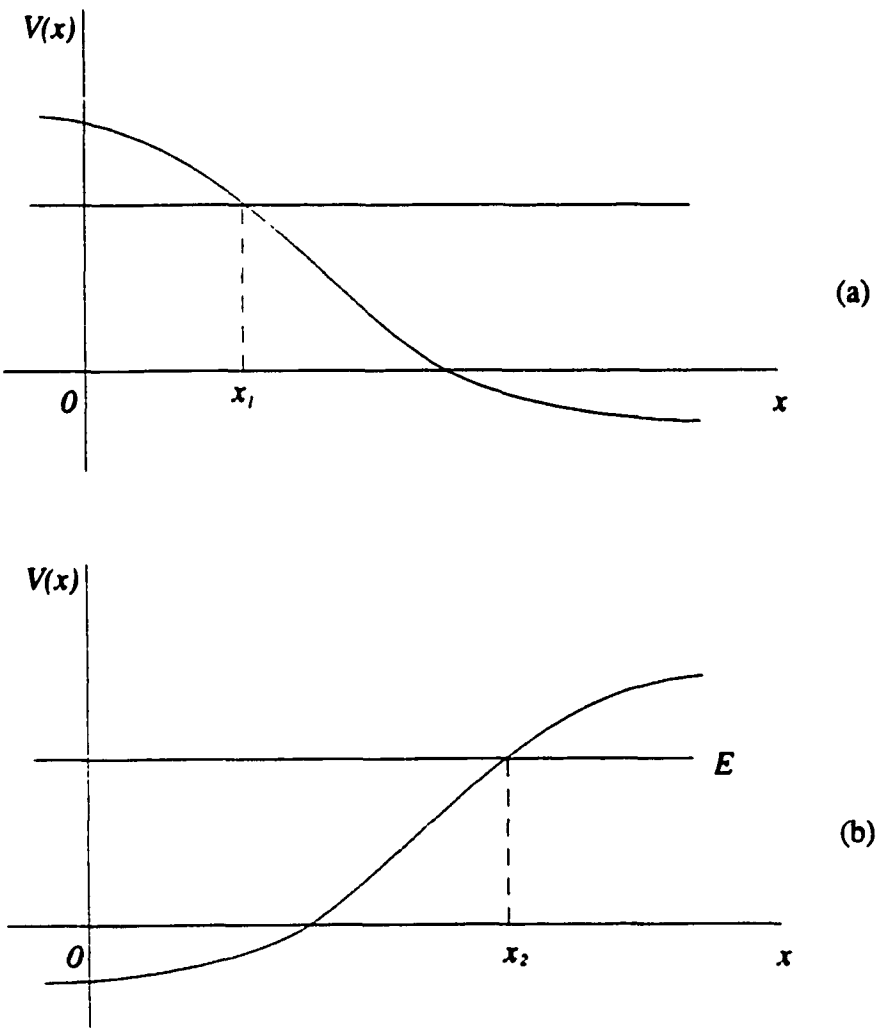

Figure A.1: (a) A left-hand barrier. The point x_1 is the classical turning point. (b) A right-hand barrier. The classical turning point is at x_2.

where the left-hand side is valid for $x < x_1$ and the right-hand side is valid for $x > x_1$. The arrow indicates the direction in which the connection formula can be applied. For the case where the wave function increases exponentially as x recedes to the left of x_1, the appropriate connection formula is

$$|p(x)|^{-1/2} \exp\left[-\frac{1}{\hbar}\int_{x_1}^{x} |p(x')|\,dx'\right] \leftarrow [p(x)]^{-1/2} \sin\left[\frac{1}{\hbar}\int_{x_1}^{x} p(x')dx' - \frac{\pi}{4}\right] \qquad (A.22)$$

where the left-hand side is valid on the left side of the turning point, and the right-hand side is valid on the right side of the turning point. Again, the arrow indicates the direction in which the connection formula can be applied. In the case of a right-hand barrier (see Fig. A.1b), the classical turning point is $x = x_2$. The appropriate connection formulae are given by

$$2[p(x)]^{-1/2} \cos\left[-\frac{1}{\hbar}\int_{x_2}^{x} p(x')dx' - \frac{\pi}{4}\right] \leftarrow |p(x)|^{-1/2} \exp\left[-\frac{1}{\hbar}\int_{x_2}^{x} |p(x')|\,dx'\right] \qquad (A.23)$$

and

$$[p(x)]^{-1/2} \sin\left[-\frac{1}{\hbar}\int_{x_2}^{x} p(x')dx' - \frac{\pi}{4} + \sigma\right] \rightarrow -|p(x)|^{-1/2} \cos\sigma \exp\left[\frac{1}{\hbar}\int_{x_2}^{x} |p(x')|\,dx'\right] \qquad (A.24)$$

where

$$\sigma = (2n+1)\frac{\pi}{2} \quad n = 0, 1, 2, \cdots \qquad (A.25)$$

The WKB approximation for $x < x_2$ is placed on the left side of the equations, and that for $x > x_2$ is on the right side.

Penetration of a potential barrier

To demonstrate the application of the WKB approximation and the connection formulae, consider the one-dimensional step barrier shown in Fig. A.2. Let the function $V(x)$ describe the potential barrier shown, with a maximum potential energy of V_o. An incident beam of particles is incident from the left, with kinetic energy $E < V_o$. x_1 and x_2 are the

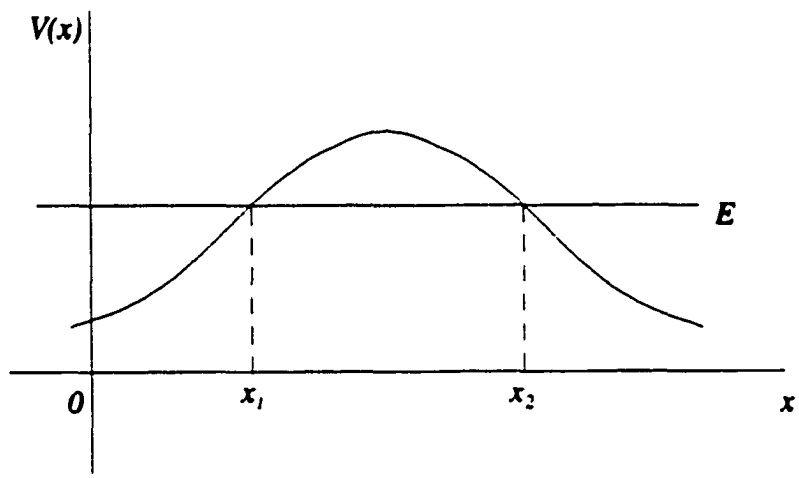

Figure A.2: A one-dimensional potential barrier. The energy E of the incident particle is assumed to be less than V_o, the top of the barrier. x_1 and x_2 are the classical turning points.

two classical turning points where the connection formulae will be applied. Some particles incident to the barrier will be reflected back into region 1, and some will be transmitted in to region 3. The wave function of those that are transmitted will is given by the WKB approximation:

$$\Psi_3(x) = A[p(x)]^{-1/2} \exp\left[\frac{i}{\hbar}\int_{x_1}^{x} p(x')dx' - i\frac{\pi}{4}\right] \quad x > x_1. \tag{A.26}$$

Although the factor $\exp(-i\pi/4)$ could have been included in A, it has been written in this form to facilitate the application of the connection formulae. Writing the imaginary part of the equation in terms of sine and cosine yields

$$\Psi_3(x) = A[p(x)]^{-1/2}\left\{\cos\left[\frac{1}{\hbar}\int_{x_1}^{x} p(x')dx' - \frac{\pi}{4}\right] + i\sin\left[\frac{1}{\hbar}\int_{x_1}^{x} p(x')dx' - i\frac{\pi}{4}\right]\right\}, \quad x > x_1 \tag{A.27}$$

Using the fact that as x recedes to the left of x_1 the wave function will increase exponentially, we use the connection formula for a left-hand barrier to obtain the wave function for region 2:

$$\Psi_2(x) = -iA\,|p(x)|^{-1/2} \exp\left[\frac{1}{\hbar}\int_{x}^{x_1} p(x')dx'\right], \quad x_2 < x < x_1 \tag{A.28}$$

This equation can be written in the from of a decreasing exponential for $x > x_2$:

$$\Psi_2(x) = -iA\,|p(x)|^{-1/2}\, e^{\Lambda} \exp\left[-\frac{1}{\hbar}\int_{x_2}^{x} |p(x')|\,dx'\right], \quad x_2 < x < x_1 \tag{A.29}$$

where

$$\Lambda = \frac{1}{\hbar}\int_{x_2}^{x_1} |p(x)|\,dx = \frac{1}{\hbar}\int_{x_2}^{x_1} 2m[V(x) - E]^{1/2}dx \tag{A.30}$$

The connection formulae can now be applied to eqn. A.29 to find the wave function in region 1 for the case of a right-hand barrier. Eqn. A.23 yields the wave function

$$\Psi_1(x) = 2iA[p(x)]^{-1/2} e^{\Lambda} \cos\left[-\frac{1}{\hbar}\int_{x_2}^{x} p(x')dx' - \frac{\pi}{4}\right]$$

Writing the above equation in exponential terms yields

$$\begin{aligned}\Psi_1(x) \;=\; & -iA[p(x)]^{-1/2} e^{\Lambda}\left\{\exp\left[i\left(\frac{1}{\hbar}\int_{x_2}^{x} p(x')dx' + \frac{\pi}{4}\right)\right]\right. \\ & \left. + \exp\left[-i\left(\frac{1}{\hbar}\int_{x_2}^{x} p(x')dx' + \frac{\pi}{4}\right)\right]\right\}, \quad x < x_2. \end{aligned} \tag{A.31}$$

The first term in curly brackets represents a wave moving to the right (the incident wave), and the second term represents a wave moving to the left (the reflected wave).

The *transmission coefficient* is the ratio of the intensities of the transmitted and reflected probability current densities. Probability density is the product of the intensity of the wave times the velocity. The ratio of the velocities is equal to the ratio of the corresponding momenta. Therefore, the transmission coefficient can be found from eqn. A.27 and eqn. A.31:

$$\begin{aligned} T &= e^{-2\Lambda} \\ &= \exp\left[-\frac{2}{\hbar}\int_{x_2}^{x_1}\{2m[V(x)-E]\}^{1/2}dx\right]. \end{aligned} \tag{A.32}$$

Field emission of electrons from a metal

The WKB approximation will now be applied to field emission of electrons from a metal under the application of an electric field ε. The deformed potential barrier is shown in Fig. A.3. E_f is the Fermi energy, ϕ is the work function. The first classical turning point at x_1 is found by solving the equation

$$V_o - e\varepsilon x_1 = V_o - \phi \tag{A.33}$$

which yields $x_1 = \phi/e\varepsilon$. The second classical turning point x_2 is at the surface of the metal, so that $x_2 = 0$. At this point, the potential function varies sharply, and the validity of the WKB approximation is in question. However, the fraction of the transmission coefficient coming from this region is quite small, and should not introduce serious error. Eqn. A.32 with $x_1 = \phi/e\varepsilon$, $x_2 = 0$, and $V(x) - E = V_o - e\varepsilon x - E = \phi - e\varepsilon x$, the the transmission coefficient T is given by

$$\begin{aligned} T &= exp\left[-\frac{2}{\hbar}\int_0^{\phi/e\varepsilon} 2m(\phi - e\varepsilon x)^{1/2}dx\right] \\ &= exp\left[-\frac{4}{3}\frac{\sqrt{2m}\phi^{3/2}}{\hbar e\varepsilon}\right]. \end{aligned} \tag{A.34}$$

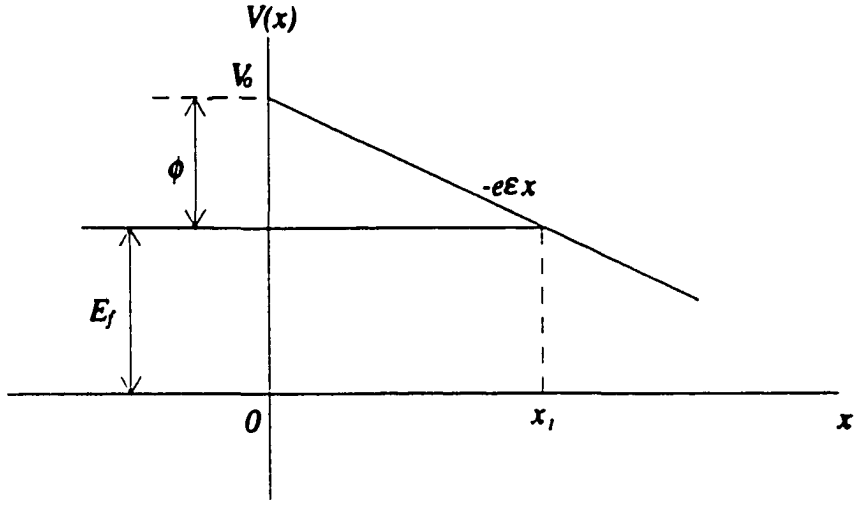

Figure A.3: Schematic representation of the potential function at the surface of a metal with applied electric field ε. x_1, the classical turning point, is such that $x_1 = \phi/e\varepsilon$.

The tunneling current per area is found by multiplying the transmission coefficient with the energy distribution of electrons $N(E)$ incident on the barrier. This product is then integrated over the energy range 0 to E_f, the Fermi level. According to Fowler and Nordheim [11], the result of these calculations is

$$j = C_0 \frac{E_f^{1/2}}{(\phi + E_f)\phi^{1/2}} E^2 e^{-C_2\phi^{3/2}/E} \tag{A.35}$$

where C_0 and C_2 are constants. The Fowler-Nordheim equation is often approximated by

$$j = C_1 \frac{\beta^2 E^2}{\phi} exp\left(-C_2 \frac{\phi^{3/2}}{\beta E}\right) \tag{A.36}$$

where C_1 is a constant, and β is the geometric electric field enhancement factor.

Bibliography

[1] R. Latham. *High Voltage Vacuum Insulation.* Academic Press-Limited, London, England, 1995.

[2] D. K. Davies. The initiation of electrical breakdown in vacuum - a review. *J. Vac. Sci. Tech.*, 10:115–121, 1973.

[3] D. W. Williams and W. T. Williams. Effect of electrode surface finish on electrical breakdown in vacuum. *J. Phys. D: Appl. Phys.*, 5:1845–1854, 1972.

[4] R. A. Millikan and C. F. Eyring. *Phys. Rev*, 27:51–67, 1926.

[5] V. A. Nevrovskiy, V. I. Rakhovskiy, V. G. Zhurbenko, and V. A. Zernaev. Gas desorption from electrodes and electrical breakdown in vacuum. *J. Phys. D: Appl. Phys.*, 14:215–220, 1981.

[6] L. Cranberg. *J. Appl Phys.*, 23:518–522, 1952.

[7] C. Texier. Breakdown initiation in vacuum: Electrical charge of microparticles emitted in a vacuum gap. *J. Phys. D: Appl. Phys.*, 10:1693–1702, 1977.

[8] Burkhard Juttner. Vacuum breakdown. *Nucl. Instr. And Methods in Physics Research*, A268:390–396, 1988.

[9] N. S. Xu and R. V. Latham. The application of an energy-selective imaging technique to a study of field-induced hot electrons from broad-area high voltage electrodes. *Surface Science*, 274:147–160, 1992.

[10] R. Gomer. Field emission, field ionization, and field desorption. *Surface Science*, 299/300:129–152, 1994.

[11] R. H. Fowler and L. Nordheim. Electrons in intense electric fields. *Proc. R. Soc.*, A 119:173–181, 1928.

[12] W. P. Dyke and W. W. Dolan. *Advances in Electronics and Electron Physics.* Academic Press, New York, 8 edition, 1956.

[13] N. K. Allen, B. M. Cox, and R. V. Latham. The source of high-β electron emission sites on broad-area high-voltage alloy electrodes. *J. Phys. D: Appl. Phys.*, 12:969–977, 1979.

[14] B. Bonin. Field emission and surface conditioning. *Vacuum*, 46(8-10):907–912, 1995.

[15] M. Jimenez, R. J. Noer, G. Jouve, C. Antoine, J. Jodet, and B. Bonin. Electron field emission from selectively contaminated cathodes. *J. Phys. D: Appl. Phys.*, 26:1503–1509, 1993.

[16] R. E. Hurley and P. J. Dooley. Electroluminescence produced by high electric fields at the surface of copper cathodes. *J. Phys. D: Appl. Phys.*, 10:L195–L201, 1977.

[17] N. Pupeter, T. Habermann, A. Kirschner, E. Mahner, G. Muller, and H. Piel. Comparative studies on enhanced field emission from mechanically and chmically polished broad-area nb, cu, and al cathodes. *Draft Copy.*

[18] T. Kelsey. Measurements of prebreakdown current and x-ray emission in vacuum. *J. Phys. D: Appl. Phys.*, 5:569–574, 1972.

[19] B. M. Cox and W. T. Williams. Field-emission sites on unpolished stainless steel. *J. Phys. D: Appl. Phys.*, 10:L5–L9, 1977.

[20] Shinichi Kobayashi. Recent experiments on vacuum breakdown of oxygen-free copper electrodes. *XVIIth International Symposium on Discharges and Electrical Insulation in Vacuum - Berkeley*, pages 9–16, 1996.

[21] Ping He and M. K. Sinha. Prebreakdown characteristics of thin film-coated molybdenum electrodes. *J. Appl. Phys.*, 12:6184–6186, 1989.

[22] Jr. J. N. Smith. Suppression of prebreakdown current by a cathode coating of silicon. *J. Appl. Phys.*, 60:1490–1492, 1986.

[23] A. V. Batrakov, D. S. Nazarov, G. E. Ozur, S. A. Popov, D. I. Proskurovsky, and V. P. Rotshtein. Increasing the electric strength of vacuum insulation by treating the electrodes with a low-energy high current electron beam. In *XVIIth International Symposium on Dishcarges and Electrical Insulation in Vacuum*, pages 487–491, Berkeley, CA, 1996.

[24] H. L. Skriver and N. M. Rosengaard. Surface energy and work function of elemental metals. *Phys. Rev. B*, 46(11):7157–7168, 1992.

[25] A. Zeitoun-Fakiris and B. Juttner. On the dose of bombarding residual gas ions for influencing pre-breakdown field emission in a vacuum. *J. Phys. D: Appl. Phys.*, 24:750–756, 1991.

[26] Little and Whitney. *J. Appl. Phys.*, 34:2430, 1968.

[27] J. R. Conrad, J. L. Radke, R. A. Dodd, F. J. Worzala, and N. C. Tran. *J. Appl. Phys.*, 62:4591, 1987.

[28] Y. Chen, Y. Shi, H. Xie, Z. Wu, X. Jiang, T. Bell, and H. Dong. Surface engineering of steels by plasma immersion ion implantation and related innovative techniques. *Surface Engineering*, 12(2):137–141, 1996.

[29] Lothar Koch, Axel Lesche, and Wolfram Maring. Fighting arcing and field emission in medical x-ray tubes. *XVIIth International Symposium on Discharges and Electrical Insulation in Vacuum*, pages 1077–1081, 1996.

[30] W. Ensinger. Plasma immersion ion implantation for metallurgical and semiconductor research and development. *Nucl. Instr. and Meth. in Phys. Res.*, B 120:270–281, 1996.

[31] J. M. Williams, G. M Beardsley, R. A. Buchanan, and R. K. Bacon. In *Proceedings of Materials Research Society Symposium on Ion Implantation and Ion Beam Processing of Materials*, page 735, 1983.

[32] C. B. Franklyn and G. Nothnagel. Nitrogen profiles of high dose, high temperature plasma source ion implantation treated austenitic stainless steel. *J. Vac. Sci. Technol. B*, 12(2):923–926, 1994.

[33] R. E. Hurley. Electrical phenomena occurring at the surface of electrically stressed metal cathodes - electroluminescences and breakdown phenomena with medium gap spacings (2-8 mm). *J. Phys. D: Appl. Phys.*, 12:2229–2245, 1979.

[34] Ph. Niedermann, N. Sankarraman, R. J. Noer, and O. Fischer. Field emission from broad-area niobium cathodes: Effects of high-temperature treatment. *J. Appl Phys.*, 59(3):892–901, 1986.

[35] M. Jimenez, R. J. Noer, G Jouve, J. Jodet, and B. Bonin. Electron field emission from large-area cathodes: evidence for the projection model. *J. Phys. D: Appl. Phys.*, 27:1038–1045, 1994.

[36] P. Spolaore, G. Bisoffi, F. Cervellera, R. Pengo, F. Scarpa, G. Binelle, and A. Zanon. The large gap case for high voltage insulation in vacuum. *XVIIth International Symposium on Discharge and Electrical Insulation in Vacuum, Berkeley*, 1996.

[37] M. Ohring. *The Materials Science of Thin Films*. Academic Press, Inc., San Diego, CA, 1 edition, 1992.

[38] D. D. Pollock. *Physical Properties of Materials for Engineers*. CRC Press, New York, 2 edition, 1993.

[39] K. H. Bayliss and R. V. Latham. *Vacuum*, A 403:285–311, 1986.

[40] F. F. Chen. *Introduction to Plasma Physics*. Plenum Publishing Corporation, New York, NY, first edition, 1974.

[41] M. A. Lieberman. *Principles of plasma discharges and materials processing.* John Wiley & Sons, Inc., New York, 1 edition, 1994.

[42] J. T. Scheuer, M. Shamim, and J. R. Conrad. Model of plasma source ion implantation in planar, cylindrical, and spherical geometries. *J. Appl. Phys.*, 67(3):1241–1245, 1990.

[43] G. A. Emmert and M. A. Henry. Numerical simulation of plasma sheath expansion, with applications to plasma-source ion implantation. *J. Appl. Phys.*, 71(1):113–117, 1992.

[44] M. H. Cho, N. Hershkowitz, and T. Intrator. Temporal evolution of collisionless sheaths. *J. Vac. Sci. Technol. A*, 5(6):2978–2986, 1988.

[45] S. M Malik, K. Sridharan, R. P. Fetherston, A. Chen, and J. R. Conrad. Overview of plasma source ion implantation research at University of Wisconsin-Madison. *J. Vac. Sci. Technol.*, B 12(2):843–849, 1994.

[46] S. Qin, Z. Jin, and C. Chan. An equivalent circuit and its effective impedance of a plasma load during a high voltage pulse. *Nucl. Inst. and Meth. in Phys. Res.*, B 114:288–292, 1996.

[47] A. Chen, J. Firmiss, and J. R. Conrad. Dose analysis of nitrogen plasma source ion implantation treatment of titanium alloys. *J. Vac. Sci. Technol. B*, 12(2):918–922, 1994.

[48] M. M. Shamim, J. T. Scheuer, R. P. Fetherston, and J. R. Conrad. Measurement of electron emission due to energetic ion bombardment in plasma source ion implantation. *J. Appl. Phys.*, 70(9):4756–4759, 1991.

[49] B. Y. Tang, R. P. Fetherston, M. Shamim, R. A. Breun A. Chen, and J. R. Conrad. Measurement of ion species ratio in the plasma source ion implantation process. *J. Appl. Phys.*, 73(9):4176–4180, 1993.

[50] J.P. Biersack and L.G. Haggmark. A monte carlo computer program for the transport

of energetic ions in amorphous targets. *Nuclear Instruments and Methods*, 174:257–269, 1980.

[51] L. H. Van Vlack. *Elements of Materials Science and Engineering.* Addison-Wesley Publishing Company, Reading, Massachusettes, sixth edition, 1989.

[52] Y. C. Kim, C. J. Yu, and D. N. Seidman. Effects of low-energy (1-1.5 kv) nitrogen-ion bombardment on sharply pointed tips: Sputtering, implantation and metal-nitride formation. *J. Appl. Phys.*, 81(2):944–950, 1997.

[53] S. Bajic and R. V. Latham. A new perspective on the gas conditioning of high-voltage vacuum-insulated electrodes. *J. Phys. D: Appl. Phys.*, 21:943–950, 1988.

[54] D. Alpert, D. A. Lyman, and H. E. Tomaschke. *J. Appl. Phys.*, 38:880–881, 1967.

[55] C. D. Wagner, W. M. Riggs, L. E. Davis, J. F. Moulder, and G. E. Muilenberg. *Handbook of X-Ray Photoelectron Spectroscopy.* Perkin-Elmer Corporation, Eden Prairie, MN, 1 edition, 1979.

[56] V. John. *Introduction to Engineering Materials.* Industrial Press, Inc., New York, 3 edition, 1992.

[57] J. B. Hudson. *Surface Science - An Introduction.* Butterworth-Heinemann, Stoneham, MA, 1 edition, 1991.

[58] B. H. Bransden and C. J. Joachain. *Introduction to Quantum Mechanics.* Addison Wesley Longman Limited, Essex, England, 1 edition, 1989.

Vita

Thomas Joseph Venhaus

Tom was born in Grand Island, NE on June 15, 1968. He attended High School at Central Catholic High School in Grand Island, NE and graduated in June, 1986. He married Dawn Mani Guilmet on October 12, 1996 in Williamsburg, VA. Tom received his Bachelor of Science degree in Physics from Hastings College, Hastings, Nebraska in May, 1991. Following undergraduate studies, Tom entered the Applied Science department of The College of William & Mary in Virginia where he received his Master of Science in Applied Science in December, 1993. Tom will begin a post-doctoral position with Sandia National Labs in Livermore, California. The work will be performed at Los Alamos National Laboratory in Los Alamos, New Mexico. Tom and his wife are expecting their first son in April, 1998.